

---

**Development of Computational Analysis Criteria Based on  
Laser Sensor Device to Identify the Surface Status of  
Micro-structured Coatings for Aerospace Industry**

**Dissertation**  
approved  
for the degree of  
Doctor in Engineering  
-Dr-Ing-

Faculty of Production Engineering  
Department of Production Engineering  
University of Bremen

by

**Mauricio Zadra Pacheco**

**Bremen, May 2017**

---

**Entwicklung von Rechnerische Analysekriterien auf Basis  
der Lasersensor-Vorrichtung zur Identifizierung des  
Oberflächenstatus von mikrostrukturierten  
Beschichtungen für die Luft-und Raumfahrtindustrie**

Dem Fachbereich Produktionstechnik

Der

Universität Bremen

Zur Erlangung des Grades  
Doktor-Ingenieur  
Genehmigte

**Dissertation**

von

**Mauricio Zadra Pacheco**

**Bremen, Mai 2017**

1. Referee: Prof. Dr. rer nat Bernd Mayer

2. Referee: Prof. Dr. Max Mauro Dias Santos - Universidade Tecnológica Federal do Paraná - Ponta  
Grossa (UTFPR-PG) - Brazil

Dissertation Defense Date: 03.08.2017

# Abstract

In 2009, the European Union decided that CO<sub>2</sub> emissions on ship and aerospace industries must be reduced by 10% and 20% respectively. To fulfill these requirements, aerospace industries looking for new approaches to overcome this challenge and take technological gains. The use of bio-inspired micro-structured coatings, e.g.riblet structured based on shark skin; this is one of new technologies applied. In this context, quality control in manufacturing and maintenance of structured coatings is of extreme relevance specifically for aerospace industries to ensure the optimal surface structuring, to assist maintenance, to predict life time, and consequently to decide when to perform surface renewal. The mentioned requirements are met with an experimental fast sampling sensor setup using noncontacting laser probing. The theory behind the laser sensor device is based on Huygens-Fresnel diffraction theory combined with ray-tracing calculation methods. A computational tool was developed to perform analysis and treatment of output data provided by the laser sensor. This dissertation aims to present a methodology to evaluate the calculations implemented in this computational tool. It is used to interpret the obtained diffraction patterns, and as a tool to simulate the structured surface status from a given pattern. Thus, the software is developed to generate consistent information for analysis and decision-making regarding the surface structure and its maintenance. The software development is performed by using Object Oriented programming (OOP) and it is also integrated with database management systems (DBMS).Optics theory is discussed and applied to specific target, graphical renderization of pre-determined geometric micro-structured coatings are implemented and the fundamental outputs to evaluate the real status of the surface are described and treated to be a reliable knowledge database.

Overcomming the experimental requirements to build a reliable theoretical base to implement consistent outputs to the proposed technique, this dissertation brings the analysis criteria identified to be applied in further studies, the investigation and application of well-known theoretical founding to be a starting to new techonlgies contributing to open new perspectives on this field, joining the necessary interdisciplinarity on computer science, physics and engineering to improve the knowledge on the field of quality assurance, applied, in this particular case, on aerospace industry.

# Zusammenfassung

Im Jahr 2009 hat die Europäische Union entschieden, dass die CO<sub>2</sub> Emissionen von Schiffen und Flugzeugen um 10 bzw. 20% reduziert werden müssen. Um diese Anforderung zu erfüllen sucht die Luftfahrtindustrie nach neuen Ansätzen, mit denen gleichzeitig technische Vorteile erzielt werden können. Der Einsatz biomimetisch inspirierter mikro-strukturierter Oberflächenbeschichtungen wie z.B. der Haifischhaut nachempfunderer Riblets ist eine dieser neuen Technologien. In diesem Zusammenhang ist die Qualitätsüberwachung strukturierter Oberflächen in Fertigung und Einsatz besonders im Luftfahrtbereich von äußerster Relevanz, um so eine optimale Oberflächenstruktur sicherzustellen, Wartung zu unterstützen, Lebensdauern vorherzusagen und damit über den Zeitpunkt zur Erneuerung von Oberflächen zu entscheiden. Die genannten Anforderungen werden mit einem experimentellen Sensoraufbau hoher Messgeschwindigkeit und nichttaktiler Messung mittels Laser erfüllt. Die zugrundeliegende Theorie hinter dieser Lasermessung basiert auf der Lichtbeugungstheorie nach Huygens-Fresnel in Kombination mit einer dem Strahlungsverlauf folgenden Berechnungsmethode. Diese Dissertation zielt darauf ab, die im verwendeten oftwaretool eingesetzten Berechnungen zu evaluieren. Sie werden zur Interpretation der ermittelten Beugungsmuster und als tool zur Simulation des Zustands der strukturierten Oberfläche im Vergleich zu einem vorgegebenen Muster eingesetzt. Die Software wurde daher entwickelt, um eine konsistente Information zur Analyse und zur Entscheidung über notwendige Wartungsmaßnahmen der Oberfläche zu erhalten. Die Entwicklung erfolgt auf Basis des Object Oriented programming (OOP) und ist auch mit dem database management systems (DBMS) integriert. Die Theorie der Optik wird diskutiert und auf das spezielle Ziel angewendet. Eine graphische Visualisierung der Beschichtung mit vorbestimmten Mikrostrukturen ist implementiert. Fundamentaler Output zur Evaluierung des tatsächlichen Zustandes der Oberfläche wird beschrieben und als verlässliche Wissensdatenbank behandelt.

Experimentelle Herausforderungen wurden überwunden, um eine verlässliche theoretische Grundlage für die vorgeschlagene Technik zu entwickeln. Diese Dissertation identifiziert die analytischen Kriterien für weitergehende Studien. Die Untersuchung und Anwendung bekannter theoretischer Grundlagen ermöglicht neue Technologien, die zur Öffnung neuer Perspektiven in diesem Feld beitragen und so die notwendige Interdisziplinarität von Computer Science, Physik und Ingenieurwissenschaften aufzeigen, die erforderlich ist, um das Wissen zur Qualitätskontrolle –in diesem besonderen Fall in der Luftfahrtindustrie- zu steigern.

### Eidesstattliche Versicherung

Hiermit versichere, ich Mauricio Zadra Pacheco, dass ich diese Arbeit ohne unerlaubte fremde Hilfe angefertigt habe, keine anderen als die von mir angegebenen Quellen und Hilfsmittel benutzt habe und die den benutzten Werken wörtlich oder inhaltlich entnommenen Stellen als solche kenntlich gemacht habe.

---

Ort, Datum

---

Unterschrift

**I would like to dedicate this dissertation to my beloved wife, Juliana and to  
Joyce and Guilherme.  
You are the reason of all.**

## **Acknowledgements**

First of all, I would like to express my gratitude to Prof. Dr. rer nat Bernd Mayer, who with motivation and supervision guided me to finish this great step in my life.

My deepest appreciation is also extended to Professor Dr. Max Mauro Dias Santos for serving as referee of this dissertation.

To Prof. Dr. Horst-Erich Rikeit, for supporting and teaching me about the German way of life. A special thanks go to Dr. Welchy Leite Cavalcanti, Dr. Paul-Ludwig Michael Noeske, Dr. Hauke Brünning and Mr. Kai Brune for teaching me theory during my studies which aroused my interest for this field of research.

To Dr. Stefan Dieckhoff, for the opportunity to work in OE-418 at Fraunhofer - IFAM.

I take this opportunity to thank my mother (in memoriam) and my father, for their love, support and encouragement during my life.

To the Coordination for the Improvement of Higher Level Personnel (CAPES), for supporting me, under the frame of the Brazilian Program Science without Borders.

To the State University of Ponta Grossa (UEPG), for the funding and support to the development of my work.

I would like to thank all my colleagues in Fraunhofer Institute for Manufacturing Technology and Advanced Materials (Fraunhofer - IFAM) for their support and pleasant ambience as well as all the other people that directly or indirectly were related to my studies and my work.

Finally, to my wife Juliana, my daughter Joyce and my son Guilherme, my family, who without their love, patience, smiles, kisses and hugs, this work would have no success and no motivation.



*“Try not. Do...or do not. There is no try.”*

*Master Yoda – The Empire Strikes Back*

## Table of Figures

Figure 1 - Bio-inspired micro-structured coating - Shark skin based riblet .....	1
Figure 2 - Streched marks of a shell <i>Placopecten magellanicus</i> . Source: [33] .....	5
Figure 3 - Real spacement of streched marks. Position $x = 0, 0.25L, 0.5L$ and $0.75L$ from the distance of the shell border, for two representative shells: (a) $L = 32\text{mm}$ ; (b) $L = 48\text{mm}$ . Continuous lines represent the limits for the optimal region of the streched marks based on drag reduction, specific for each shell, based on length and speed travel. Source: [33] .....	5
Figure 4 - Roughness geometry used by Lee and Lee[34]. .....	8
Figure 5 - Superficial and Sub superficial discontinuities - Detection methods. Based on [46] .....	14
Figure 6 - Internal discontinuities - Detection methods. Based on [46] .....	15
Figure 7 - Schematic structure of the laser sensor device for the investigation of a riblet structure. The intensity distributions of the reflections on the riblet sample are detected with the Central and Lateral Detectors based on [8] .....	20
Figure 8 - Schematic Representation of the three-dimensional Planar waves .....	27
Figure 9 - Schematic Representation of the three-dimensional spherical waves .....	27
Figure 10 - Schematic Representation of the three-dimensional cylindrical waves .....	28
Figure 11 - Schematic representation of the Huygens Principle .....	33
Figure 12 - Huygens Principle for a blocked wave front. ....	33
Figure 13 - Schematic representation of Young's experience .....	35
Figure 14 - Transition from Fresnel Diffraction pattern to Fraunhofer Diffraction pattern .....	37
Figure 15 - Difference between a flat wave front and a spherical wave front to diffracted waves (a) and incident waves (b). ....	39
Figure 16 - Schema for generation of the Fraunhofer diffraction pattern for a simple slit in a target. ...	40
Figure 17 - Schematic representation of the generation of the Fraunhofer diffraction pattern of a simple slot (a) schematic representation of the opening corresponding to a simple slot (b). ....	41
Figure 18 - Single Slit and the corresponding Fraunhofer diffraction pattern (Schematic Representation) .....	44
Figure 19 - Double slit and the corresponding Fraunhofer diffraction pattern (Schematic Representation) .....	45
Figure 20 - Diffraction Grid (a) and Horizontal Profile (b) of Diffraction grid in a Fraunhofer Pattern ...	48
Figure 21 - Schematic representation of the diffraction pattern generation for a rectangular opening of comparable dimensions. ....	48
Figure 22 - Schematic representation for an arbitrary gap. ....	49
Figure 23 - Schematic representation for a rectangular aperture. ....	50
Figure 24 - Schematic representation of a circular aperture. ....	52
Figure 25 - Integration Process to Analysis Criteria Evaluation of the Proposed Technique .....	56
Figure 26 - Sketch of the intact riblet modeling .....	59
Figure 27 - Schematic representation of the Reflection in a riblet structure, considering parameters to be input in the integration of Fresnel Equation .....	62
Figure 28 - Schematic representation of the interaction of light with the intact riblet surface. A): vertical incidence on the surface. The beam is reflected back to the central detector. B), C): Interaction with a riblet flank. By reflection, the beam is projected in the direction of $45^\circ$ to the base of the surface and then follows to the lateral detectors. ....	63
Figure 29 - 2D Plot – $120\ \mu\text{m}$ laser spot reflection – Intact structure – Generated by computational tool .....	63
Figure 30 - Sketch of the intact riblet structure in comparison to degraded riblet structures (50% degraded and 100% degraded) .....	64
Figure 31- Validation of the Computational Tool Calculations .....	66
Figure 32 - Operation of the Computational tool on quality assurance field in Production Line .....	67
Figure 33 - Operation of the Computational tool on quality assurance field in Maintenance Line .....	68
Figure 34 - Entity-relationship Model .....	71
Figure 35 - Analysis evaluation process flow chart .....	73
Figure 36 - Intensity plot calculated – Electric Field equation .....	74

Figure 37 - Intensity plot calculated – Fresnel Integration .....	75
Figure 38 - Symmetry evaluation.....	76
Figure 39 - Periodicity evaluation .....	77
Figure 40 - Distance variation based on wave equation .....	78
Figure 41 - Distance variation based on Fresnel integration.....	78
Figure 42 - Detail – Central Detector – Intact Riblet Sample – 19 riblets – Fresnel Pattern.....	80
Figure 43 - Detail – Central Detector – Intact Riblet Sample – 9 riblets – Fresnel Pattern.....	80
Figure 44 - Detail – Central Detector – Intact Riblet Sample – 9 riblets – Fraunhofer Pattern .....	81
Figure 45 - Detail – Central Detector – Intact Riblet Sample – 20 riblets – Wavelength Comparison..	81
Figure 46 - Measured distance comparison of different wavelength lasers calculated and theoretical values. ....	83
Figure 47 - Comparison between experimental measured intensity performed via laser sensor device and calculated intensity performed via computational tool with detailed graphic in evaluated region between the central maxima and 1st maxima. ....	84
Figure 48 - Schematic representation of the laser reflection on riblet flanks to lateral detector .....	85
Figure 49 - Intensity plot calculation of lateral detector (right side), Absolut calculations (a) and periodicity evaluation of calculations in log scale(b). ....	86
Figure 50 - Intensity plot calculation of lateral detector (right side), Expected variation of the peaks ..	87
Figure 51 - Intensity plot calculation of lateral detector (right side) - Detail in Logarithmic scale .....	88
Figure 52 - Intensity plot calculation - Left detector. Comparison between calculated and experimental data in logarithmic scale. ....	89
Figure 53 – Degraded riblet structure – laser reflection sketch on central detector.....	90
Figure 54 – Degraded riblet structure – Central detector plot evaluation .....	91

## Table of Contents

Chapter 1 - Introduction.....	1
Chapter 2 - State of the art.....	4
2.1 - Riblet Structured Coatings.....	4
2.2 - Non Destructive Tests.....	12
2.2.1 - Based Laser Sensor Device.....	19
2.3 - Applied Optics Theory.....	21
2.3.1 - Interference and Diffraction Theory.....	21
2.3.2 - General overview of interference and diffraction.....	22
2.3.3 - Huygens Principle.....	32
2.3.4 - Young experience.....	34
2.3.5 - Fraunhofer and Fresnel diffraction.....	37
2.3.6 - Diffraction: Simple Slit.....	40
2.3.7 - Diffraction – Theory for rectangular apertures.....	48
2.3.8 - Diffraction – Theory for circular apertures.....	51
Chapter 3 - Objectives.....	56
Chapter 4 - Boundary Conditions.....	58
Chapter 5 - Concept of a methodology to identify micro-structured surfaces.....	66
Chapter 6 – Description of the Computational tool development and application.....	70
Chapter 7 - Results Evaluation.....	73
Chapter 8 – Conclusions and Outlook.....	92
Chapter 9 - References.....	97

## List of Abbreviations

<b>Abbreviation</b>	<b>Definition</b>
<b>ABENDE</b>	Brazilian Association of Non Destructive Testing
<b>ASME</b>	North America Society of Mechanical Engineers
<b>ASTM</b>	American Society for Testing and Materials
<b>CO<sub>2</sub></b>	Carbon Dioxide
<b>DbMS</b>	Database Management System
<b>GHG</b>	Greenhouse Gas
<b>IFAM</b>	Institute for Manufacturing Technology and Advanced Materials
<b>NASA</b>	National Aeronautics and Space Administration
<b>NDT</b>	Non-destructive Tests
<b>OOP</b>	Object Oriented Programming
<b>SQL</b>	Structured Query Language

**Chapter 1 - Introduction**

In aerospace industry, status identification of structured surfaces, e.g. shark skin, called tiny ribs (riblets - Figure 1), is an option to support the quality assurance and keep desired performance of these coatings. Riblets are used as an alternative to drag reduction and consequently save fuel and reduce Greenhouse gas (GHG) emissions [2]. These riblets are part of strategical and technological possibilities to fulfill the decision taken by the European Union that CO<sub>2</sub> emissions from aviation and shipping industry must be reduced by 10% and 20% respectively, in a period of medium to long term [3], for instance, due to climate change caused by GHG emissions [4].

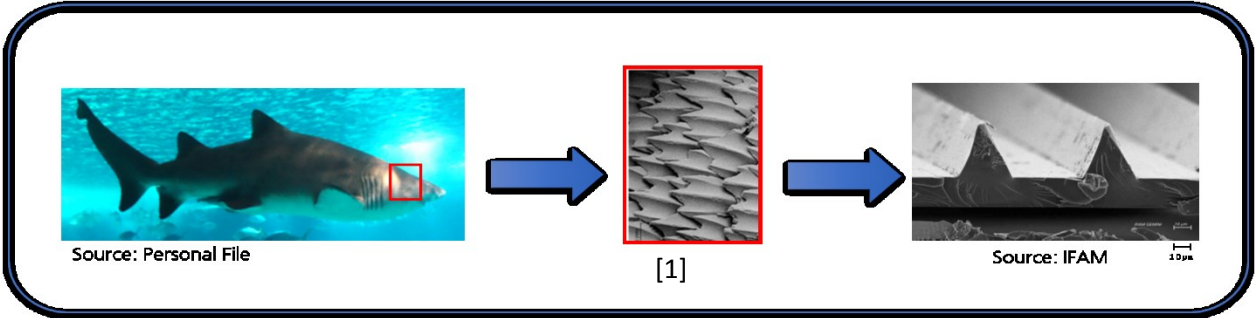


Figure 1 - Bio-inspired micro-structured coating - Shark skin based riblet

Quality assurance using Non-destructive tests (NDT) is a powerful tool in terms of reliability, costs and easiness. NDT improvements are related to safety of aviation components and structures. The NDT technique refers to testing methods specially used to analyze structural parts or objects without harming or affecting future usefulness. The main goals of NDT are to identify hidden defects or damages. Furthermore, via NDT material properties can be evaluated and the structure geometry can be measured [5]. According to the American Society for Testing and Materials [6] the concept of NDT is based on the “development and application of technical methods that examine materials and components, in order to detect, measure and evaluate discontinuities, defects and other imperfections. Integrity, properties and composition assessment and measure geometrical characteristics are evaluated by NDT as well”. In special attention to riblet structure coatings, geometrical characteristics and integrity are important parameters to keep the desired functionality. Among the methods of

possible tests to be applied to this specific analysis of coatings based on riblet structures, non-destructive testing tend to be powerful for this application.

Characterization of micro-structured surfaces has to be achieved in nanoscale level. Research on characterization of surfaces is being made by using full field of polarized light-scattering, and experimental findings have reached a good agreement with theoretical predictions considering different surface roughness. [7]

Development of NDT includes concepts of non-contact devices, such as the one proposed by Imlau et al [8], and it can be an alternative to evaluate the conditions of structured surfaces. Researchers from Osnabrück University presented a sensor development based on the intensity of the distribution principle of the scattered light generated by laser beam incidences normal to the riblet layer [9]. In the mentioned work, the calculations based on Huygens-Fresnel diffraction theory applied on riblet surfaces were implemented in a code based on Mathematica software, showing the expected applicability of the proposed method. The laser light behavior prediction is a relevant step for the implementation of this proposed technique. The calculations based on Huygens-Fresnel and Fraunhofer diffraction theories are the initial step to fulfill the computational tool implementation and to provide a knowledge database to be compared to experimental measurements.

The application of non-destructive testing must be taken into account in order to achieve the main objective, identifying the structural geometry of the coating based on riblet structure with the functionality of drag reduction.

The purpose of this work in the beginning is graphically reproducing the original riblet structure geometry, which will be the basis for all calculations and data analysis and ensure the quality of the coating characteristics. Aiming the continuous investigation of the proposed technique, it will be concentrated in defining the outlines of the expected calculations in a computational tool specially developed to identify the micro-structure coating status. The definition of the reliable criteria to analyze the outputs of the computational tool in comparison to experimental outputs is the main motivation for this work, being a basis to

further complex analysis of advanced cases of degradation in coatings used in aerospace industry, saving costs and time in the quality assurance tasks.

The “state of the art” chapter presents the theoretical funding related to non-destructive tests, micro-structured surfaces and applications and optics theories applied to develop the proposed method.

Based on described theoretical findings, the chapter 3 “Objectives” will explain the main purpose of this work, detailing the targets to be aimed with the sequency of the priority tasks in order to uptake the final results in agreement with the expected goals.

The chapter “Boundary Conditions” defines the work scope of this dissertation, detailing the materials, equipment and methods used to develop the experimental part of this dissertation, the chapter expounds about the original geometry used to define the riblet surface and the main parameters to set the algorithm calculations, the development techniques and theoretical foundation will be detailed as well.

The chapter “Concept of a methodology to identify micro-structure surfaces” will explain about the proposed methodology in order to be applied in aviation industry quality assurance, explaining the proposed method to be applied in production line and in maintenance line.

Chapter 6, “Description of the computational tool development and application” describes development and documentation of the computational tool specially developed to this work, the project and models related to database and software development are included in this chapter.

The chapter “Results and Discussions” discuss the main results obtained in explored cases and defines the main lines to a reliable interpretation of the presented outputs.

And finally, chapter “Conclusions and outlook” explains the contributions of the work to improve a robust computational tool able to identify micro-structured surface status, defining the main guidelines and criteria which can be adopted in further computational applications.



### Chapter 2 - State of the art

#### 2.1 - Riblet Structured Coatings

As a result of the identification of coherent structures in turbulent boundary layers, a large number of studies began to emerge in the 1970s concerned with the description of turbulent flows in the region of the wall. The concept of using a grooved surface, i.e. with micro-cavities or longitudinal rivets, to achieve a reduction in drag by friction induced changes in the coherent structure of a turbulent boundary layer was for example explored in the Choi (1989) [10].

The investigation of passive methods of surface drag reduction was initiated by Walsh and colleagues [11]; [12]; [13] at NASA's Langley Research Center. These authors studied several types of surfaces with parameterized grooves, concluding that, for a real gain in drag reduction, the groove size should be basically as thick as the viscous sublayer. Their studies obtained a reduction of 8% in trawl through a surface with triangular roughness. Choi, Pearcey and Savill (1987) [14] performed tests on a towing tank and a wind tunnel. Three-dimensional bodies have successfully demonstrated the efficiency of grooves in drag reduction on a surface with a double curvature and a non-zero pressure gradient. Compressibility and Reynolds numbers in the grooves were investigated in real-scale aircraft [15] and in a high velocity wind tunnel [16]. Both studies have confirmed efficiency in the reduction of trawling.

Efforts have been also made by several other researchers (Johansen and Smith 1983 [17], Hooshmand, Young e Wallace 1983 [18], Gallagher e Thomas 1984 [19] , Bacher e Smith 1985 [20], Bechert, Hoppe e Reif 1985 [21], Bechert et al. 1986 [22], Choi [23–26], Dinkelacker, Nitschke-Kowsky e Reif 1987 [27], Coustols e Cousteix 1986 [28], Nieuwstadt et al. 1986 [29], Reidy 1987 [30], Reidy e Anderson 1988 [31], Djenidi et al. 1988) [32] who studied the difference between the structure of a turbulent boundary layer on a grooved surface and a smooth surface.

Anderson et al. (1997) [33] published a study on drag reduction observing the micro-grooves that exist in the shells. The shells of several species have micro-grooves arranged radially, and consequently parallel to the flow during locomotion, Figure 2. In some shells the size of these grooves decreases - in their locomotion velocity - to adapt to the needs of drag reduction. In addition, the actual spacing of the striations gradually migrates to the region with theoretically ideal spacing with the increase of the shell length to values greater than 40 millimeters, Figure 3.

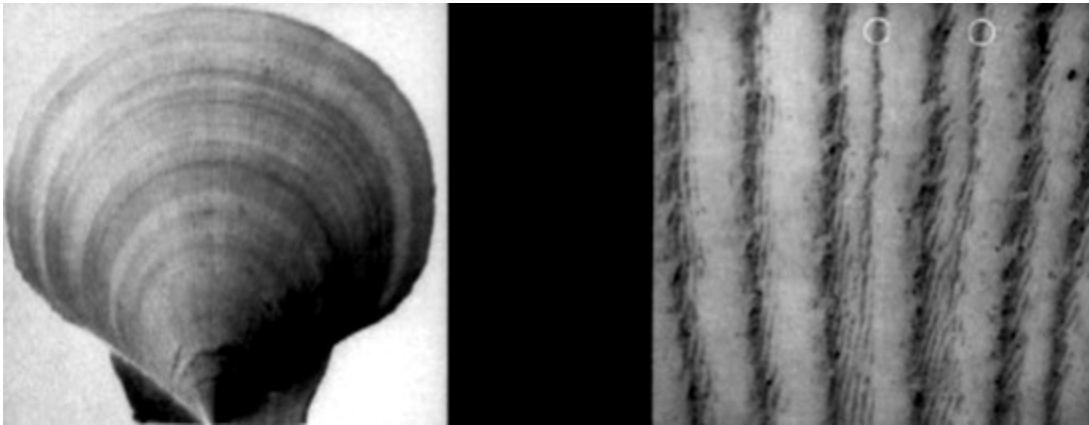


Figure 2 - Strecht marks of a shell *Placopecten magellanicus*. Source: [33]

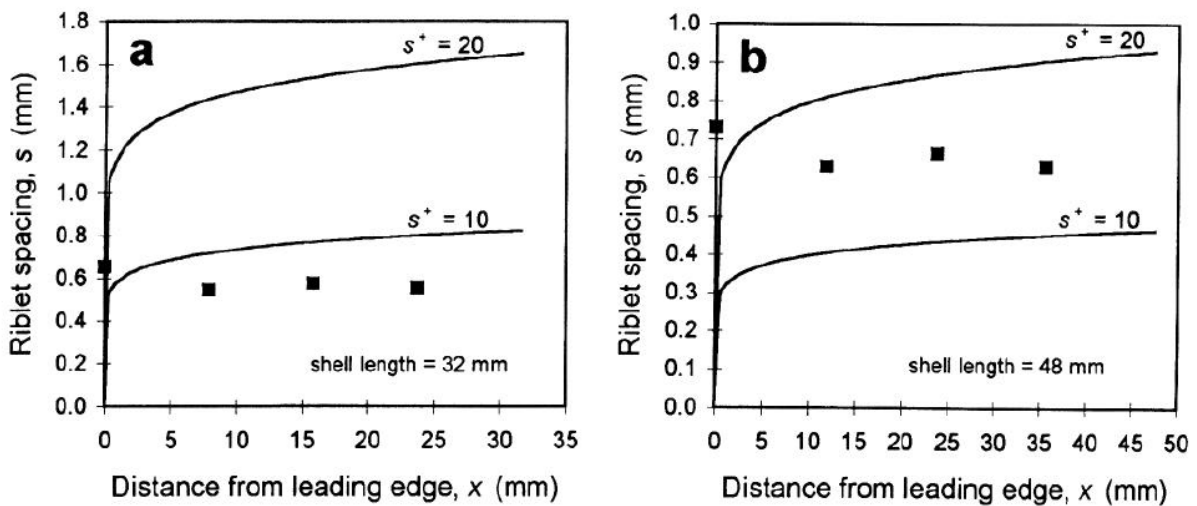


Figure 3 - Real spacement of stretched marks. Position  $x = 0, 0.25L, 0.5L$  and  $0.75L$  from the distance of the shell border, for two representative shells: (a)  $L = 32\text{mm}$ ; (b)  $L = 48\text{mm}$ . Continuous lines represent the limits for the optimal region of the stretched marks based on drag reduction, specific for each shell, based on length and speed travel. Source: [33]

Species of *Placopecten magellanicus* with 40 to 80 millimeters in length demonstrate great locomotive ability. The available data suggest that the longitudinal grooves may be a contributing factor to the success in the mobility of shells with this size range. The shells use a propulsion jet system for their locomotion. Water collected when the shells open, and, as in a valve, a membrane holds a volume of water between the shells, which is expelled in two jets adjacent to the joint. The displacement velocity common to shells with 65 mm ventral-dorsal length is approximately 0.55 m/s. Its displacement ability allows shells to escape from predators such as the starfish. As some authors suggest, they also use this ability to migrate along the stations. Of course, if the latter behavior can be seen as a significant part of the life cycle of a shell, the development of structural characteristics of drag reduction would not be surprising [33].

Recent years have witnessed the application of longitudinal grooves, or splines, in aircraft and hulls of high performance boats with the objective of reducing drag. Thus, a higher transport speed with a reduction in energy costs can be obtained. The physical mechanism identified with the use of striations involves a reduction in the surface shear stress due to changes in the viscous sublayer. Similar grooves (stretch marks, slots) in aquatic organisms may offer the same advantage. Anderson examined about 440 species of bivalves (molluscs covered by shells of two lateral valves - oysters and mussels) from 60 families representing more than 160 genera and concluded that radial striations of similar size to those of *Placopecten magellanicus* occur almost exclusively for the displacement of bivalves [33].

The theoretical and experimental work of researchers specializing in Fluid Mechanics has elucidated the function and efficiency of striations, with a drag reduction of 3% to 8% in several systems, including flat plates, high performance boat hulls, aircraft and shark skin [34]. Although the role of stretch marks (roughness) is not yet fully understood, researchers have formulated a theory based on the organization of surface vortices to explain the mechanism of drag reduction. According to this line of thought, there is a reduction in the drag component due to the occurrence of high shear generated by the action of the said

vortex tubes of the clamp type. At turbulent boundary layers, hair clip-shaped vortex tubes occur near to the surface, oriented so that the curve of the clip is downstream, and the two stems of the clip are pointing upstream and approximately parallel to the direction of the flow. As the clamp curve is drawn downstream of the flow, the remaining vortex tubes move toward each other in a perpendicular direction to the flow and parallel to the surface, which results in the projection of fluid towards the surface, giving rise to a phenomenon known as "explosion", something like "blast near the wall". The grooves may be able to block the translation of vortex tubes by arranging them on the surface in corridors aligned with the flow. This may inhibit the interaction between the vortex tubes and suppress the formation of bursts [35].

According to Anderson's Et al. (1997) [33], the spacing of the striations for optimal drag reduction can be determined as a function of internal scales of the flow,

$$S^+ = \frac{su_r}{\nu} \quad (1)$$

Where  $S^+$  is a dimensionless expression of the groove spacing,  $s$  is the actual spacing of the grooves,  $\nu$  is the kinetic viscosity of the fluid and  $u_r$  is the friction velocity. The equation is simply a rearrangement of the standard expression for dimensionless length parameter, in terms of the internal similarity variables,  $\nu$ ,  $\tau_w$ , and  $\rho$ . Such dimensionless parameters are used in fluid dynamics for reasons that, in general, any two systems with the same value of  $S^+$  will have similar behavior, although the real dimension,  $s$ , may be different [33].

Bechert (2000) [36] observed the reduction of trawl through the shark skins exhibiting high locomotor velocities; they, allegedly, use a passive method of drag reduction through roughness similar to grooves. Bechert (2000) [36] compared a surface with the same characteristics of the shark skin with a flat plate, obtaining a drag reduction of 7.3% to the striated surface. Initially the experiments were done in wind tunnel; afterwards they were conducted in an oil channel, where it was possible to increase the scale of the riblet in 10 times, that means, a riblet that measured 0.5 mm passed to measure 5 mm, which greatly

facilitated the construction of the experiment. The lateral spacing between the rivet ( $s$ ) was 4.6 mm with  $s^+ = 19$ .

According to Lee and Lee(2001) [37], the field of velocities on a riblet surface with semicircular grooves was investigated through the use of the hot wire method and velocity field measurements by particle image velocimetry. The free-stream velocity was set at  $3 \text{ ms}^{-1}$  and  $5 \text{ ms}^{-1}$ , corresponding to a drag reduction for  $s^+ = 25.2$  and an increase in drag for  $s^+ = 40.6$ , respectively. The flow conditions and the variables used in the study are summarized in Table 1.

$U_0(\text{m/s})$	$Re_\theta$	$u_r(\text{m/s})$	$s^+$	Walsh(1983)
3	2340	0.126	25.2	5% Drag reduction
5	4950	0.203	40.6	4% Drag increase

Table 1 Flowing conditions - Based on Lee and Lee(2001). [34]

The groove geometry used by Lee and Lee (2001) [37] have been a semicircular section with a peak distance of 3.0 mm( $s$ ) and a peak height of 1.5 mm( $h$ ), which, according to Walsh (1983) [38], is one of the optimal forms for application in drag reduction. The geometry can be seen in Figure 4. The experiment was carried out in a wind tunnel of 6.2 m in length, 0.72 m in width and 0.6 m in height, for a rough and smooth surface.

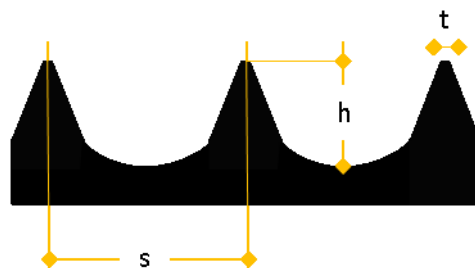


Figure 4 - Roughness geometry used by Lee and Lee[34].

For the case of drag reduction, the large longitudinal vortices scales are larger than the spacing between the ribs ( $s^+ = 25.2$ ), so that most of the longitudinal vortices are above the ribs and the flow in the valley is relatively calm. Most of the vortice centers of the longitudinal vortices are located above the virtual origin, they are concentrated mainly in the tops of the

ribs. The velocities of fluctuation and turbulent kinetic energy have small values within the viscous sublayer ( $y^+ < 5$ ). In the outer layer ( $y^+ > 30$ ), they are approximately equal or slightly smaller than on a flat plate.

For the case of drag increase ( $s^+ = 40.6$ ), however, the longitudinal vortices are smaller than the size of the spacing between the ribs, with most vortices within two valleys. High velocities from the external flow frequently penetrate the valleys. Within the valleys, the longitudinal vortices actively interact with increasing the exposed surface area, thereby increasing the friction. The fluctuation velocity and turbulent kinetic energy above the ribs have values greater than those of the flat plate.

Riblet film adhesives have been widely used in both wind tunnel surveys and flight tests. Viswanath (2002) [39] focused his work on the effectiveness of riblets for reducing viscous drag on wings at regimes of different speeds. These applications present problems in the performance of striations in pressure gradients and in the presence of three - dimensionality. On the basis of available experimental data, some general conclusions could be drawn which are informative from the point of view of design application, as well as reveal the characteristics of the flow associated with the splines.

The database generated in wind tunnel and flight experiences with high Reynolds numbers firmly establish the effectiveness of low velocity striations for moderate Supersonic Mach numbers. Taking the uncertainties in the data, the streak performance can be judged to be equivalent for the entire range of investigated Mach numbers. With optimized streaks, a viscous drag reduction in the 5-8% range can be achieved in two-dimensional airfoils with small angle of attack and in flows with slight adverse pressure gradients. There is a great coherence between the different measures that recommend a drag reduction for  $h^+$  (dimensionless of cavity height) in the range of 8-15 [39]. These measures are in agreement with the large amount of data available for zero pressure gradient flow. The correlation of viscous drag versus  $h^+$ , well established for zero pressure gradient boundary layer flows can

be a useful guide to choosing the ideal size of the stretch gradients for non-zero pressure gradient flows [39].

Frohnappfel et al. (2007) [40], experimentally proposed and tested a technique of passive control of turbulence near walls, based on changes in surface topology. An appreciation of parietal turbulence that emphasizes the degree of anisotropy of velocity fluctuations not only provides an understanding of physics behind the notable effects of turbulent drag reduction, but also leads to the logical design of a surface topology that is experimentally shown to be capable of producing a significant reduction of viscous drag. This is obtained by the turbulence force near the wall to satisfy axial symmetry in small and large scales very close to the wall with invariance under rotation on the axis aligned with the average flow.

The theoretical works of Jovanovic and Hillerbrand (2005) [41] show that the kinetic constraints imposed by axially symmetrical local turbulent forces very close to the wall tend towards the state of a component, and when the turbulence reaches this limit state it must be completely suppressed through the viscous sublayer. For this special state of turbulence, it has been shown that the turbulent dissipation disappears in the wall, forcing the dissipation of energy to occur from the average velocity field. Hence, the work done against the shear stress on the wall decreases, inducing a great drag reduction.

Following the process of fabrication and due to the aging, caused, for instance, by erosion, sand, ice, etc., in order to contextualize this dissertation, degradation of micro-structured functional coatings is possible.

Degradation can be defined as the “act or process of damaging or ruining something” [42]. Coating degradation is a combination of both chemical and physical processes [43]. In airplanes coatings there is deterioration in the coating performance due to weather and use. Anti-corrosion procedures are not useful to restore the original surface. So the coating needs to be completely stripped and reapplied, thus this process is expensive [44].

In next section, Non Destructive Tests (NDT) will be explained and defined with the purpose of contextualizing techniques and procedures used to identify the current status of micro-

structured coatings, saving costs and time in aerospace industry production and maintenance lines.



### 2.2 - Non Destructive Tests

Non Destructive Tests (NDT) are techniques that have the purpose of measuring, detecting properties or checking the performance of metallic materials (ferrous or non-ferrous) and non-metallic materials, in the form of finished or semi-finished parts or components, used in metal structures or structures [45] .

The basic principles of these tests are guided by the application of physical energies so that they do not cause damage to the inspected products. Among the definitions used and accepted by the great majority of NDT users, it is stated that: "These are tests that, when applied, do not affect or cause damage to the posterior functioning of the part (totally or partially)" [46].

It is noted that the test may provide some traceability, as long as it does not influence the operation of the component. Another definition, which presents a greater rigor, determines that "(these)are tests that do not produce posterior vestige after its application" [46].

The reasons why industries use non-destructive testing are: to maintain the good reputation of the company in order to ensure that manufactured products meet the required quality standards; generate more satisfactory profit margins, avoid disruption of essential services and, in particular, reduce the safety factor through accident prevention. Among the main reasons for NDT use, the following stand out: ability to detect discontinuities or defects in different dimensions, positions and formats. Determination of the physical properties of materials, such as optical, electrical, magnetic and mechanical properties, through the structural evaluation of components (micro-structure and matrix structure) [47].

According to Andreucci [48], NDT are evaluated as special processes by quality systems, mainly ISO-9001. All professionals working in this segment must be trained, qualified and certified according to the required quality. National entities, such as ABENDE (Brazilian Association of Non Destructive Testing) and international organizations such as ASME (North American Society of Mechanical Engineers) are able to validate such requirements.

The choice of a particular procedure over other methods is accomplished through the detection possibilities that this assay is capable of providing. If more than one method has this capability, it is possible to choose the one that best suits the reality of inspection. Another factor that can be taken into account is the speed in which the test is carried out, which can generate automation, incorporation in the manufacturing process and even in production control, provided that it is obviously economically viable [49].

Among non-destructive evaluation methods, distinct groups are classified according to the discontinuity to be determined:

- Inspection method on surfaces (discontinuities observed on external or subsurface surface). Examples of tests of this group: the visual test, penetrant liquids and magnetic particles.
- Method of volumetric inspection (discontinuities observed inside the materials). Examples of tests of this group: the ultrasonic test, radiographic test and thermography.

Table 2 presents a comparison between different test methods and their relative variables, such as: cost, geometry of discontinuities, and operating requirements [50].

<b>Test Method</b>					
<b>Variables</b>	Ultra sound	X Ray	Eddy Current	Magnetic particles	Penetrating liquids
<b>Result time</b>	Immediate	Slow	Immediate	Slow	Slow
<b>Geometry Effect</b>	Significant	Significant	Significant	Medium	Medium
<b>Defect types</b>	Internal	All	External	External	Superficial
<b>Sensibility</b>	High	Medium	High	Low	Low
<b>Formal records</b>	Expensive	medium	Expensive	Not usual	Not usual
<b>Operator Capabilities</b>	High	High	Medium	Low	Low

<b>Skills</b>	High	High	Medium	Low	Low
<b>Portability</b>	High	Low	Medium/High	Medium/High	High
<b>Composite materials</b>	Very Low	High	High	*only ferromagnetics	Low
<b>Dependency</b>					
<b>Automatization</b>					
<b>Capacity</b>	High	Medium	High	Low	Low

Table 2 Comparison between different test methods and their relative variables

Other techniques have the advantage of being used in real time. Examples of tests of this group: thermographic activity and acoustic emission [51].

Figure 5 and Figure 6 illustrate surface, subsurface and internal discontinuities and their different detection methods respectively.

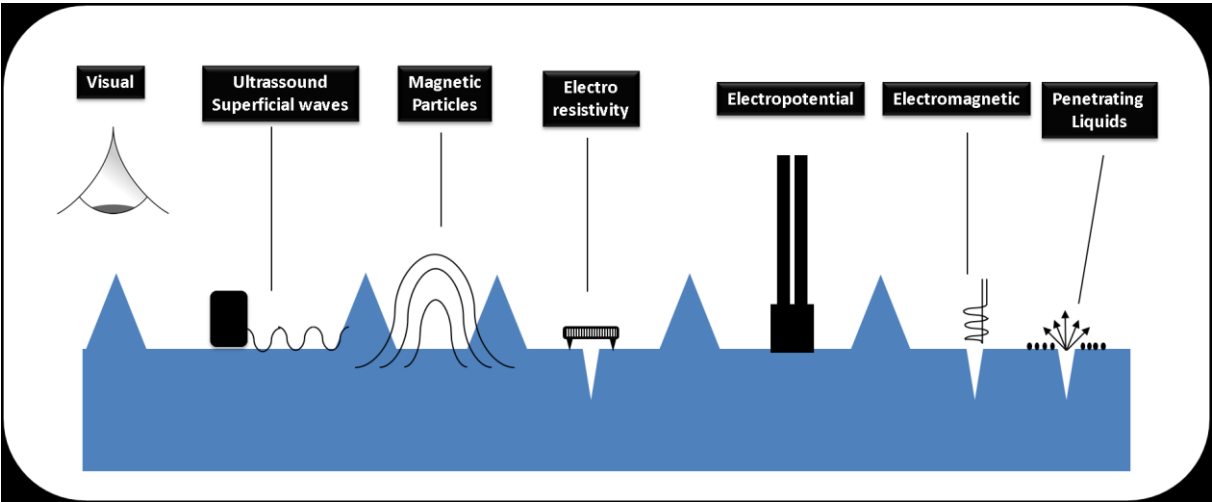


Figure 5 - Superficial and Sub superficial discontinuities - Detection methods. Based on [46]

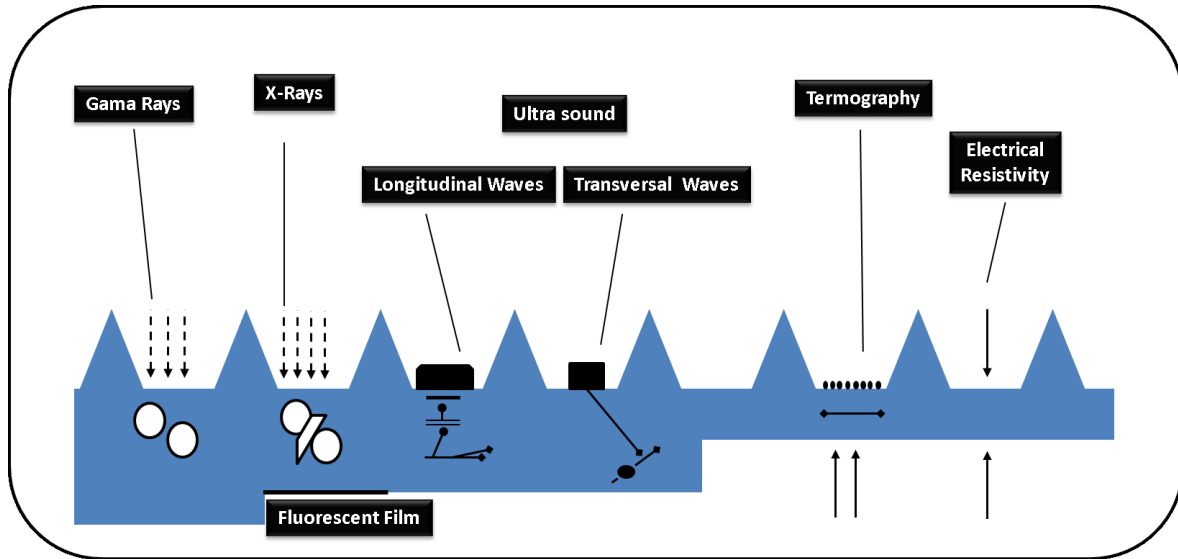


Figure 6 - Internal discontinuities - Detection methods. Based on [46]

The use of NDT can be used as an auxiliary instrument to the destructive test, since it can be used as complementary processes.

The tests are performed on the parts that will actually be put into operation, which generates a greater reliability in its use. All manufactured parts can be tested (provided there is an economic justification), and put into service, even if they differ in the manufacturing lot, as long as they meet the design requirements.

The assays have the ability to detect several properties in different regions of the material and can be implemented in sequence or simultaneously. The use of NDTs often does not require interruption of service; stopping machines for checking parts, as well as ensuring material integrity and operating conditions remain unchanged.

One of the major barriers faced by NDT is proving its ability to detect discontinuity either from the inner side or, preferably, from the external side of the component being evaluated.

Non-destructive tests are characterized by five requirements, which are [52]:

1. Choose a source that offers a specific type of inspection medium to the product being tested (sound, electromagnetic radiation).
2. The variation of the inspected medium in function of the discontinuities present or the changes in the properties verified.

3. A device for sensitive detection of the present modifications
4. Register of the presented variables by the detector so efficiently that it could be possible to be analyzed later
5. An operator or equipment capable of interpreting the required properties or the presence, size and location of discontinuities.

The primary objective of the non-destructive test is to provide the inspector with quantitative and qualitative information on the detected discontinuities, such as: corrosion, porosity, bubbles, and inclusions among others. In general, a discontinuity begins with small dimensions and, possibly, with the application of external loads, they can evolve creating catastrophic defects if not discovered in advance [53].

Inspectors should have requirements such as skill and experience as they are crucial in determining the quantitative and positioning of discontinuities. The understanding of the physical phenomena involved in the process is also essential for a correct interpretation.

The comparison or evaluation of the applicability of the test has statistical or probabilistic analysis as performance definitions. The industries use this information as parameters in the definition of the technique that presents better performance or better rates of detection [52].

The performance of inspections or a routine of non-destructive tests in the detection of defects shall be foreseen during the whole life of the component. The examples of NDT used in the industries are: hydrostatic test, water tightness, ultrasound, penetrating liquids, X-rays, gammagraphy, magnetic particles among others. [54]

The limitations of a given method, its advantages, disadvantages, sensitivity, precision and the discontinuities encountered may induce the need for more than one non-destructive test, since each technique has the capacity to provide specific information to certain classes of defects.

Table 3 presents a comparison of the advantages, disadvantages and use of the various types of non-destructive tests.

Method	Characteristics	Advantages	Limitations	Usages
<b>Ultrasound</b>	Changes in acoustic impedance caused by cracks, inclusions or interfaces	Can penetrate thick materials, excellent for crack detection, can be automated	Typically requires coupling to the material, either by surface contact or immersion in fluid such as water. Surface should be smooth.	Inclusions, lamination, cracks, pores, lack of fusion.
<b>X-Ray</b>	Changes in density by voids, inclusions, varied materials, location of internal parts.	They can be used for inspection of a range of materials and thicknesses, versatile, have films for inspection records.	Radiological safety, requires precautions, cracking detection can be difficult in orientation perpendicular to X-rays.	Welds of penetration in tubes, inclusions, voids, internal defects.
<b>Eddy Current</b>	Changes in electrical conductivity caused by various materials, cracks, voids or inclusions.	Promptly automated, moderate cost.	Limited to electrically conductive materials, limited penetration depth.	Heat exchanger tubes for walls, slabs and cracks.
<b>Magnetic Particles</b>	Leakage of magnetic flow generated by the surface or near the surface, cracks, voids, inclusions or materials with changes of geometry.	Cheap or at moderate cost, sensitive to both surfaces and near surface defects.	Limited to ferromagnetic materials, surface preparation and post-inspection demagnetization may be necessary.	Railway wheels with cracks, large parts.
<b>Penetrating Liquids</b>	Surface openings due to cracking, porosity, welding or folding.	Cheap, easy to use, portable, sensitive to small surface flaws.	Faults must be open to the surface. It is not useful in porous materials or rough surfaces.	Turbine blades with surface cracks or porosity.

Table 3 NDTs Comparison - Advantages/Disadvantages

Based on presented characteristics of commonly used NDT's applied to evaluate surfaces, applicability of a technique based on a laser sensor device, they could be a key to a fast identification of micro-structure surface status in functional coatings used on aerospace industry. Relatively, low costs and contactless process improves, in relation to traditional NDTs, allied with a powerful and fast computational tool specially designed to industrial application, a desired feedback for quality assurance of micro-structured coatings.

Next section will explain about the necessary knowledge on applied optics theory, specially concerning the diffraction theory, which is the key to implement and based the theoretical background to be delimited in this dissertation.

### 2.2.1 - Based Laser Sensor Device

To perform experimental evaluations on this work, an experimental fast sampling sensor setup using non-contacting laser probing was developed, based on the Huygens-Fresnel and Fraunhofer diffraction theories combined with ray tracing calculation methods. The experimental setup for investigating the reflection of a laser beam at the riblets is explained below (Figure 7).

The experiment can be performed with different lasers. For most experiments, the beam of a laser with a wavelength of  $\lambda = 632 \text{ nm}$  is used. The beam passes through the Mirror 1 and Mirror 2. The two mirrors serve to adjust and align the laser beam.

The structure itself consists of a system of mirrors and beam splitter. The two mirrors M1 and M2 deflect the beam which allows a vertical alignment with the riblet sample. The beam splitter DM1 is ultimately aligned in such a way that the beam tends perpendicularly to the sample. As is known, there are three directions of action. The reflex of the ray on the basis of the riblets is re-injected. A detection of this intensity can be achieved via the beam splitter DM1 with the Central Detector. This is to be understood in the following as the  $0^\circ$  Reflex. The transmission of the riblets is performed near the sample via Lateral Detectors,  $\pm 45^\circ$ -Reflex.

The riblet structures are arranged in such a way that the reflections are detected by the detectors. For this purpose, the sensors return a spatial distance of 8 mm to detect the entire intensity distribution. In addition, it is possible by this arrangement of the system to examine several types of lasers.



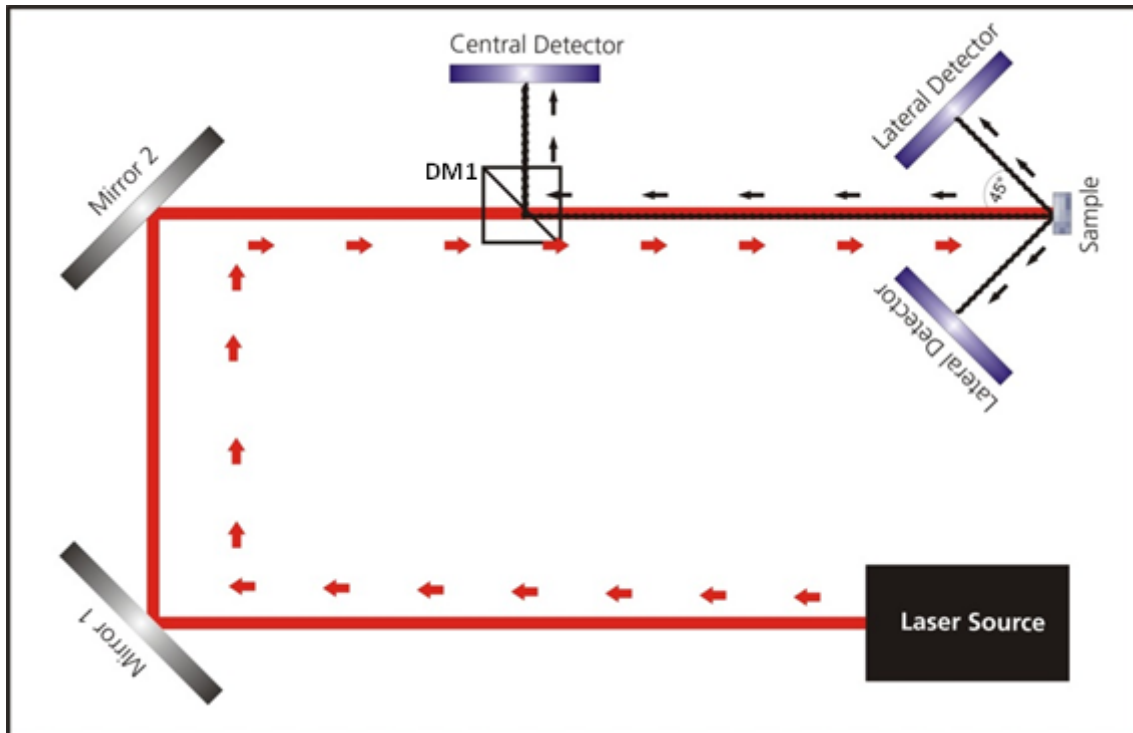


Figure 7 - Schematic structure of the laser sensor device for the investigation of a riblet structure. The intensity distributions of the reflections on the riblet sample are detected with the Central and Lateral Detectors based on [8]

The detectors used to this laser device are under the following specification (Table 4) [55]:

Item #	LC100
Detector Range (CCD Chip)	350 - 1100 nm
CCD Pixel Size	14 $\mu\text{m}$ x 56 $\mu\text{m}$ ( 14 $\mu\text{m}$ pitch )
CCD Sensitivity	240 V / ( lx · s )
CCD Dynamic Range <sup>a</sup>	333
CCD Pixel Number	2048
Integration Time <sup>b</sup>	1.055 ms – 50 s
Scan Rate Internal Trigger	Max 900 Scans/s <sup>c</sup>
S/N Ratio <sup>d</sup>	$\leq 2000 : 1$
External Trigger	
Trigger Input	BNC
Trigger Signal	TTL 5 V and 3.3 V
Trigger Frequency, Scan Rate	Max 450 Hz, 450 Scans/s <sup>c</sup>
Trigger Puls Length	Min 50 ns
Trigger Delay	4.5 $\mu\text{s}$
Number of GPIOs <sup>e</sup>	5
GPIO <sup>e</sup> Type	3.3 V TTL
Region of Interests (ROI)	16
Analog Output	Programmable 0 - 4 V
General Specs	
Interface	Hi-Speed USB2.0 (480 Mbit/s)
Dimensions ( L x W x H )	80 mm x 80 mm x 33 mm (3.13" x 3.13" x 1.30")
Weight	<0.4 kg

Table 4 Technical specification – Detectors [55]

## 2.3 - Applied Optics Theory

### 2.3.1 - Interference and Diffraction Theory

The phenomena observed in the overlap of two beams of light are analogous to those seen on overlapping two waves on the surface of the water. Although at present, the conception that the light has wave characteristics is an obtained data, it was not always like this, there was a long period of time during which the wave nature of the light was not accepted [56–60].

The wave theory of light was developed by Huygens in 1678 in counterpoint to the corpuscular theory of Newton. For a long time, this was the second vision of light that predominated. At the beginning of the 19<sup>th</sup> century, Young and Fresnel gave fresh impetus to the wave theory of light with their experiences of interference and diffraction, causing the wave theory to be accepted, although reluctantly [56–59]. The rejection of the corpuscular theory of Newton only fully unravelled with the determination of the speed of propagation of light by Foucault, which found that the speed of light showed different values for different materials and its maximum value reached for the void [56–59]. This was against the corpuscular theory that required that the speed of light in denser media was higher than the speed of light in a vacuum in order to explain the phenomenon of refraction.

The problem of non-acceptance of the wave nature of light was due in large part to the fact that the normal working range, corresponding to the effects of wave properties are not observed. The justification for the non-observation of the wave nature of light is that the dimensions of the lengths of wave associated with the light being very small. The light which corresponds to the visible region of the electromagnetic spectrum between frequencies  $3.84 \times 10^{14}\text{Hz}$  and  $7.69 \times 10^{14}\text{Hz}$ , that in terms of length of wave corresponds to a region that's going to  $390 \times 10^{-9}\text{m}$  until  $780 \times 10^{-9}\text{m}$ .

Thus, a small subject, as small as it can be, is able to block completely a light wave. An object whose dimensions are of the order of a hundred wavelengths (enough to block any

light wave) is still too small to be observed in plain sight. Therefore, the problem was the scale.

According to the wave theory, the light "circumvents" the obstacles it faces, so light in the region where there should be only a shadow of the object [59–63]. This effect is due to a phenomenon called diffraction of light. There is yet another phenomenon that results from the overlapping of some light waves; it is called interference of light. Many times you are not able to distinguish between diffraction and interference of light, there is even some confusion in the application of these two terms. The interference involves the deliberate production of two or more separate beams, while diffraction occurs naturally when somehow limited to a wave front.

In the formulation of the problem of diffraction it is considered essentially a wave in space, whose propagation is stopped by an obstacle or mask that changes locally its breadth and/or phase for a particular factor.

The principle of Huygens describes a very satisfying and simple mode of the phenomenon of diffraction of light making the approximation that the amplitude and phase of an electromagnetic wave can be described adequately by a scalar variable [56–67]. This approach is called scalar wave approach. Based on this approach, the chapter on the theory of interference and diffraction of light will be developed.

### **2.3.2 - General overview of interference and diffraction**

The light can be represented mainly in two ways, through the corpuscular theory or through the wave theory. The simplest way to represent the light results from the corpuscular theory according to which light is represented through straight rays of light (field of geometrical optics). However, when you can't discard the wavelength of light for this to be of comparable size to the size of the system, it is necessary to take into account the nature wave light, thus this is represented through waves. This is the domain of physical optics.

The essential characteristic of a wave is its non location. From a classic point of view the spread of a wave through a medium is a disturbance  $\psi$  that propagates itself in this mean transporting energy and time.

The more familiar and easier viewing waves are mechanical waves, namely the waves on strings, surface waves in liquids, the waves in spring and the sound waves in the air. Sound waves are longitudinal, i.e. the Middle suffers a disturbance in the direction of propagation of the wave while the waves are transverse in which ropes the disturbance suffered by half takes place in a perpendicular direction to the direction of wave propagation. There are two types of waves, longitudinal waves and transverse waves.

For both cases, although the energy transported by the wave propagates with the wave, the kind of material where the wave propagates remains in its region. For the waves there is no material transport. This feature distinguishes the wave clearly from a stream of particles.

The propagation of a wave in a medium is described mathematically by a differential equation, which is a function of position and time and it is called the wave equation. The most general form of the equation of wave to a dimension is obtained by the condition that any solution of the wave equation has to propagate in a given direction, with constant speed, without change in its shape over time with respect to a system of axes that move with the same velocity [56,57,59,64].

Thus, a wave that propagates according to the direction of the axis of  $xx$  in the positive or negative sense, is described by the equation

$$\psi(x, t) = f(x + vt) \quad (2)$$

where  $f(.)$  represents a differential function and where  $t$ ,  $x$  and  $v$  represents the time, direction and speed of wave propagation respectively, indicating the negative signal that the wave is moving in the positive direction of the axis of  $xx$  while the positive sign indicates the opposite situation.

The differential wave equation to a dimension is given by the equation

$$\frac{\partial^2 \psi}{\partial x^2} = \frac{1}{v^2} \frac{\partial^2 \psi}{\partial t^2} \quad (3)$$

The waveform is the one whose profile is a sine or cosine curve, known as harmonic waves, being given by the equation

$$\psi = A \sin[\kappa(x + vt) + \varepsilon] \quad (4)$$

where  $A$  and  $k$  are constants representing the amplitude and the constant wave propagation, and can vary without causing changes to the harmonic nature of the wave.  $\varepsilon$  is the initial phase of the wave. The argument of the sine function is called the phase of the wave and is represented by  $\phi$ .

The sinus or cosinus waves are periodic, representing regular pulses that are repeated infinitely. The only difference between the use of a sine function or cosine function in the representation of the shape of a wave is one of them to be early or late regarding another of  $\pi/2$  radians (90 degrees). Due to their periodicity, the form of a wave is repeated. If ever there is a diversion of a multiple integer of the wavelength ( $\lambda$ ) on all its points. Mathematically this may be expressed by the following equation

$$\psi = A \sin\{\kappa(x + \lambda) - vt\} + \varepsilon \quad (5)$$

where  $\lambda$  represents the wavelength or the spatial period. The relationship between the wavelength and the propagation constant is given by the following equation:

$$\kappa = \frac{2\pi}{\lambda} \quad (6)$$

Alternatively, if the wave is observed by a fixed position, it repeats that there is a difference in time of a multiple time period  $T$  for all points. In this case the equation for the wave is given by

$$\psi = A \sin\{\kappa[x - v(t + T)] + \varepsilon\} \quad (7)$$

Thus a relationship for the speed of propagation of the wave as a function of wavelength, is given by

$$v = \lambda V \quad (8)$$

where  $v = 1/T$  is the temporal frequency of the wave. Other amounts used in motion are the angular frequency temporal wave ( $\omega$ ) given by the equation  $\omega = 2\pi v$  and the wave number

( $\kappa$ ), given by the equation  $\kappa=1/\lambda$ . Every quantity that has been mentioned is also applicable to non-harmonious but periodic waves.

Using the previous definitions, a harmonic wave can be expressed, spreading in a certain mean, through the equations:

$$\psi = A \sin[\kappa(x \pm vt) + \varepsilon] \quad (9)$$

$$\psi = A \sin[\kappa(x \pm \omega t) + \varepsilon] \quad (10)$$

These are the most used in the representation of a wave. These waves are ideal waves ranging from  $-\infty$  to  $+\infty$  with a unique constant frequency, so with a single wavelength, monochrome. In practice this is not the case, the actual waves are not monochromatic being composed of more than one wavelength.

The velocity phase of a wave is given by the radius of the angular frequency and propagation constant. Any point on a harmonic wave in which the amplitude is constant; it is moved so that the phase remains constant in time. That's what happens in the case of circular waves generated on the surface of a liquid, for which the concentric circles represent curves where the phase remains constant in time, for all its points.

If there are two wave functions  $\psi_1$  and  $\psi_2$  they are both solutions of the wave equation, the wave function resulting from the addition of these two wave functions is also a solution of the wave equation. This is known as the principle of overlapping and it means that when two individual disturbances reach the same point in space they overlap, by adding or subtracting another one, without affecting its motion For two wave functions with similar amplitudes the result of overlap will vary, depending on the phase difference between them, between a maximum value, in the case of the two wave functions are in phase and a minimum value for the situation of opposition of phase [56–67]. This phenomenon is called interference.

Until here, only the one-dimensional wave functions were referenced. However, in the more general situation is the existence of three-dimensional waves defined by a wave equation, being also three- dimensional which is the function of  $x$ ,  $y$ , e  $z$  (In rectangular coordinates).

The three-dimensional wave equation is a generalization of equation (2) to one dimension and it's given by:

$$\nabla^2\psi = \frac{1}{v^2} \frac{\partial^2\psi}{\partial t^2} \quad (11)$$

where  $\nabla$  represents the Laplacian operator. Three-dimensional waves can be divided into three main groups: flat waves, spherical waves and cylindrical waves. Plane waves are the simplest case of a three dimensional wave. They exist when all surfaces, where the disturbance features constant phase, form a set of perpendicular planes to the direction of propagation (see Figure 8) [56–58,64,67]. The collimated laser beams are an example of a flat wave front to propagate in space. The mathematical expression for a plane wave perpendicular to a given vector  $\vec{k}$  (spread vector), which passes through a generic point  $r$  of coordinates  $(x_0, y_0, z_0)$ , is  $\vec{k} \cdot \vec{r} = const.$  Thus, the wave function for a harmonic plane wave spreading in space is given by

$$\psi(r, t) = A e^{i(\vec{k} \cdot \vec{r} \mp \omega t + \varepsilon)} \quad (12)$$

where  $A$ ,  $\omega$  and  $k$  are constants, which as stated above represent the amplitude, angular frequency and constant wave propagation, respectively. As this disturbance propagates along  $\vec{k}$  direction, has to every point in space and time a given phase. For a given time, the areas between all points of equal phase are known as wave front. If the amplitude  $A$  is constant at all points, the wave function will have the same value in all that wave front. In the most general case as  $A$  is function of position, the amplitude is not constant across the front of the wave and the wave is no longer homogeneous.

The importance of the plane waves in optics comes firstly from the easyness with which you can generate, and secondly because any three-dimensional wave can be expressed as a combination of plane waves with different amplitudes and directions of propagation [56].

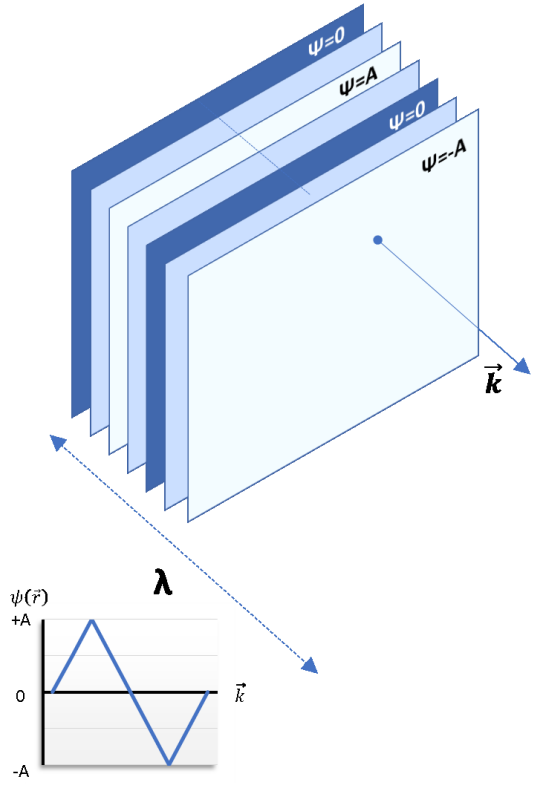


Figure 8 - Schematic Representation of the three-dimensional Planar waves

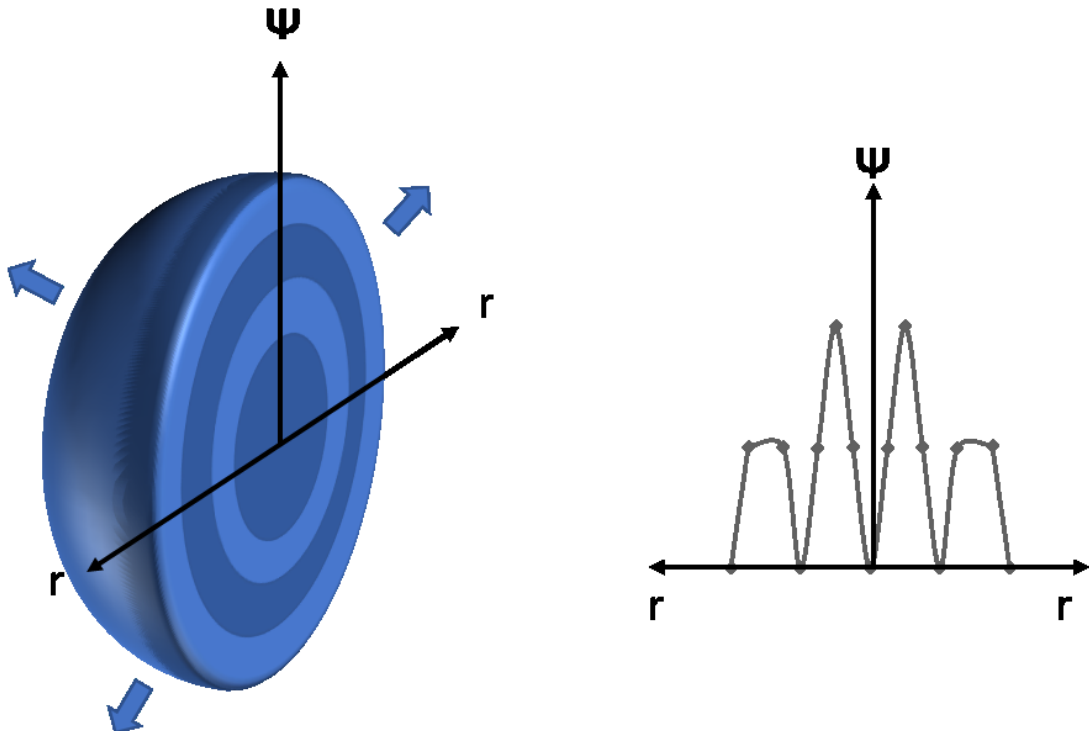


Figure 9 - Schematic Representation of the three-dimensional spherical waves



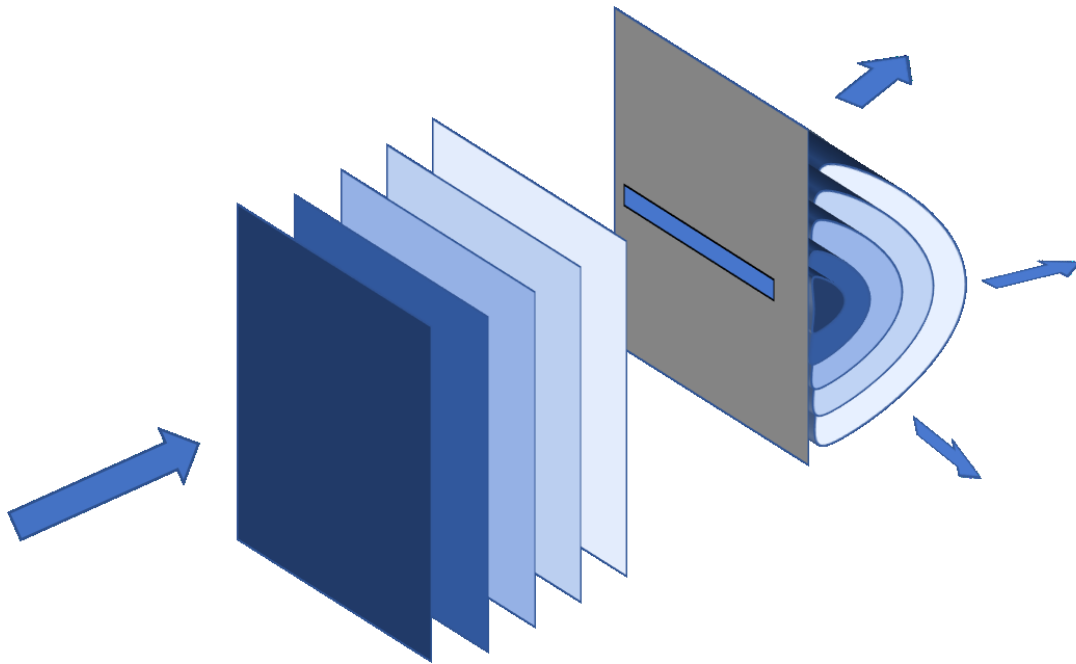


Figure 10 - Schematic Representation of the three-dimensional cylindrical waves

Relation to spherical waves they consist of a set of concentric spheres that increase in diameter as they expand in space (see Figure 9). These types of waves are described, for reasons of convenience, in terms of spherical coordinates. The wave function for three-dimensional spherical waves has the form

$$\psi(r, t) = \left(\frac{A}{r}\right) e^{i(\vec{k}\vec{r} \mp \omega t + \varepsilon)} \quad (13)$$

where  $A$  is a constant that represents the intensity of the source. Due to the factor  $1/r$ , *spherical waves* decrease of amplitude changing their profile as they expand in space.

The third type of three-dimensional waves is cylindrical waves. When a plane wave front strikes a plane opaque target containing a thin slot and long enough, a disturbance in the form of a cylindrical wave is obtained (in Figure 10). In this case the phenomenon is described in terms of cylindrical coordinates. The wave function for the cylindrical waves presents the following form

$$\psi(r, t) \approx \left(\frac{A}{\sqrt{r}}\right) e^{i(\vec{k}\vec{r} \mp \omega t)} \quad (14)$$

The most common situation is the existence of multiple waves reaching a point or to co-exist along the same direction. It is then necessary, according to the principle of superposition previously mentioned; to calculate the resulting effect from the combination of these several waves. As it has already been mentioned, the disruption resulting from the superposition of multiple waves at a particular point is given by the algebraic sum of several individual waves. Two situations can occur resulting in completely different results: overlapping waves have amplitude and different stages but have the same frequency or beyond different amplitudes and phases also have different frequencies.

In the first case the addition of waves with the same frequency as the spreading in the same direction, it is still a harmonic wave with the same frequency of the constituent waves but with different amplitude and phase [56,58,64]. The general expression for the global disturbance resulting from the superposition of N disruption is the following

$$\psi(x, t) = A \sin[\omega t + \alpha(x, \varepsilon)] \quad (15)$$

where  $\alpha(x, \varepsilon)$  represents the spatial part of the phase of the resulting disruption and it is given by

$$\tan \alpha = \frac{\sum_{i=1}^N A_i \sin \alpha_i}{\sum_{i=1}^N A_i \cos \alpha_i} \quad (16)$$

and  $A$  represents the amplitude of the resulting disturbance given by:

$$A^2 = \sum_{i=1}^N A_i^2 + 2 \sum_{j=1}^N \sum_{i=1}^N A_i^2 A_j^2 \cos(\alpha_i - \alpha_j) \quad (17)$$

If the various phases are random disturbances, the phase difference is also random. In this case the sum of the terms in cosine will tend to zero as  $N$  increases. So for identical sources to the total disturbance amplitude is given by  $A^2 = \sum_{i=1}^N A_i^2 = N A_i^2$ . The square of the amplitude of  $N$  identical sources with random phases is equal to the sum of the squares of the amplitudes of each of the sources.

If on the other way the  $N$  sources (identical) are consistent and in the process at the point of observation, this is  $\alpha_i = \alpha_j$ , the resulting disturbance is given by  $A^2 = (\sum_{i=1}^N A_i^2)^2 = N^2 A_i^2$ . The result is the square of the range of  $N$  identical coherent sources with the same phase is equal to  $N^2$  times the sum of the amplitude squares of each source.

Still in the case which the disturbances have the same frequency but spread in opposite directions the resulting disturbance is a standing wave, preventing a disturbance from spreading, whose profile is constant in space and is given by:

$$\psi(x, f) = 2A \sin kx \cos \omega t \quad (18)$$

In this case, the amplitude is equal to  $2A \sin kx$  varying harmonically with  $\cos \omega t$ .

Another situation is the overlapping of disturbances with similar amplitudes but with different frequencies. In this case the resulting disturbance ceases to be harmonic and is given by:

$$\psi(x, t) = 2A(x, t) \cos(\bar{k}x - \bar{\omega}t) \cos(k_m x - \omega_m t) \quad (19)$$

where  $\bar{\omega}$  and  $\bar{k}$  represent the angular frequency average and propagation constant average respectively and  $\omega_m$  and  $k_m$  represent the frequency of modulation and the spread of modulation, respectively. The overall effect is low-frequency disturbances as engaging modulating high-frequency disturbances. The resulting disturbance features so the phenomenon of beats and the frequency of double frequency modulation rate of surrounding [56,64]. The speed of propagation of disturbances of high frequencies is the phase speed while the propagation speed of surrounding (disturbances of low frequency) is called speed group.

In the specific case of light being electric and magnetic vector fields, the light is then a vector phenomenon. The disturbance resulting from the superposition of electromagnetic waves can be expressed in terms of electric field or magnetic field. As a general rule, it uses the electric field for variables in wave equations, because it is easier to be detected.

According to the principle of superposition, the intensity of the electric field at a point in space, resulting from the interaction of several electric fields at this point, it is the algebraic sum of the intensities of all individual fields acting at a point. As the electric field has a very high frequency of variation, of the order of  $10^{14}$  Hz it is not possible or it is impracticable to work with instantaneous values of the field. Working with a quantity of irradiance, which is proportional to the time average of the electric field intensity square. The irradiance is a

quantity that has the advantage of being able to be measured directly through specific detectors. Let us consider two wave forms

$$\vec{E}_1(\vec{r}, t) = \vec{E}_{01} \cos(\vec{k}_1 \cdot \vec{r} - \omega t + \varepsilon_1) \quad (20)$$

$$\vec{E}_2(\vec{r}, t) = \vec{E}_{02} \cos(\vec{k}_2 \cdot \vec{r} - \omega t + \varepsilon_2) \quad (21)$$

where  $\vec{k}_1$  and  $\vec{k}_2$  represents the propagation vectors of each wave,  $\vec{r}$  represents the position vector and  $\varepsilon_1$  and  $\varepsilon_2$  represents the initial phases of each wave. The definition of irradiance, yields the following expression

$$I = \varepsilon_0 c \langle \vec{E}^2 \rangle T \quad (22)$$

The total irradiance resulting from the superposition of two waves  $\vec{E}_1(\vec{r}, t)$  and  $\vec{E}_2(\vec{r}, t)$  is then given by  $I = I_1 + I_2 + I_{12}$ , where  $I_{12}$  is the interference term given by  $I_{12} = 2 \langle \vec{E}_1 \cdot \vec{E}_2 \rangle T$ .

Calculating this term in function of the global phase difference that results from the pathways difference of the two waves:

$$I_{12} = \vec{E}_{01} \cdot \vec{E}_{02} \cos \delta \quad (23)$$

Considering that  $\vec{E}_{01}$  is parallel to  $\vec{E}_{02}$  (most common situation) the interference term is given by:

$$I_{12} = 2\sqrt{I_1 I_2} \cos \delta \quad (24)$$

Where  $\delta = (\vec{k}_1 \cdot \vec{r} + \varepsilon_1 - \vec{k}_2 \cdot \vec{r} - \varepsilon_2)$  is the global phase difference between waves.

The total irradiance is given by:

$$I = I_1 + I_2 + 2\sqrt{I_1 I_2} \cos \delta \quad (25)$$

In the case of all waves present amplitudes equal to  $I_0$ , the previous expression reduces to

$$I = 2I_0(1 + \cos \delta) \quad (26)$$

Or

$$I = 4I_0 \cos^2 \frac{\delta}{2} \quad (27)$$

In conclusion:

- Two orthogonal linearly polarized waves do not interfere, since  $I_{12} = 0$  (equation 23).

- The maximum irradiance is obtained when  $\cos(\delta) = 1$ , this is when  $\delta = 0, \pm 2\pi, \pm 4\pi\dots$  or when two waves are in phase. This is the condition of completely constructive interference.
- The minimum irradiance is obtained when  $\cos(\delta) = -1$ . In this case  $\delta = \pm\pi, \pm 3\pi \pm 5\pi$  and both waves are in opposition of phase. This is the condition of totally destructive interference.
- $0 < \cos \delta < 1$  results in condition of constructive interference  $I_1 + I_2 < I < I_{\text{Max}}$ .
- $0 > \cos \delta > -1$  results in condition of destructive interference  $I_1 + I_2 > I > I_{\text{Min}}$ .
- $\cos(\delta) = 0$  is the situation of squaring where  $I = I_1 + I_2$ .

The final considerations, related to the utmost importance about the study of the phenomena of interference and diffraction, one must have in mind that:

- For two light beams to produce a stable pattern of interference they should have approximately the same frequency; otherwise there will be variations in the phase difference very quickly, which originates the average value of the interference term to be zero during the detection range.
- To be able to observe a pattern of fringes it is not necessary that the two sources are in phase with each other but that the phase difference between them remains constant, that is, that the two sources have spatial coherence.

### 2.3.3 - Huygens Principle

When a punctual source projects the shadow of an object on a target, the easiest way is to think that shadow was well defined, in accordance with the corpuscular theory of light. However, as mentioned above, because of the wave nature of light, if it is carefully examined, this shade has edges of separation between light and shade areas of light and shadow areas. This effect is originated by the deflection of a certain amount of light into the shadow zone (Figure 11(a)).

To explain this behavior of the light, Huygens proposed a principle according to that each point on a front of progressive wave acts as a source of secondary spherical waves, which

propagate at the same speed of the original wave and its engaging, after some time, it constitutes a new wave front (Figure 11 (b) and (c)).

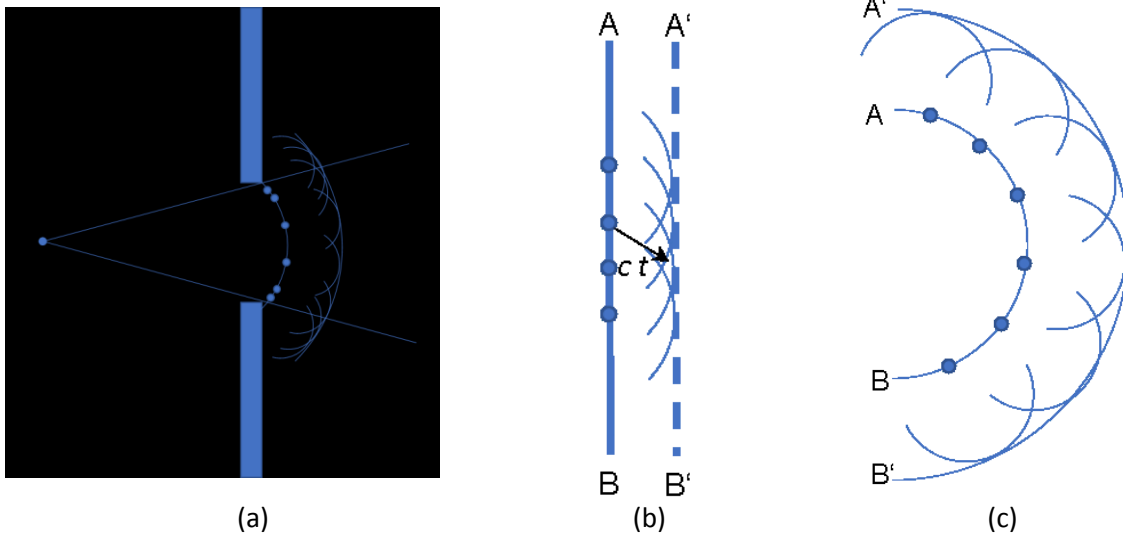


Figure 11 - Schematic representation of the Huygens Principle

The principle of Huygens is particularly useful when the waves affect an obstacle and their wave fronts are partially blocked. For these cases, Huygens showed the waves around the obstacle juxtaposing to shadow zone [59–63]. This work around the obstacle is known as diffraction. In Figure 12, three demonstrative scenarios of the Huygens principle are presented: for an edge, for a large aperture and a very small, comparable to the wavelength of the radiation.

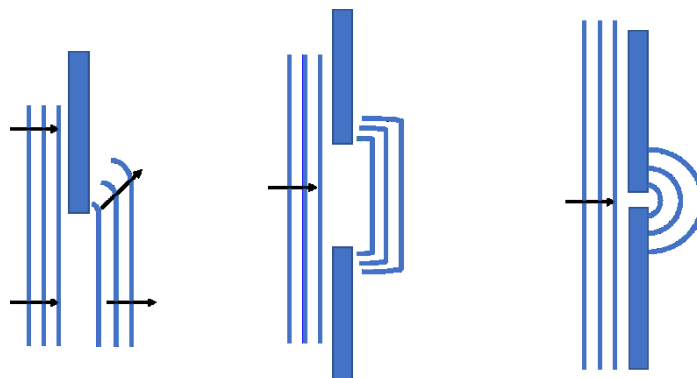


Figure 12 - Huygens Principle for a blocked wave front.

These effects can easily be observed in a tub of water blocking the wave front according to the examples presented in Figure 12.

The diffraction can be divided into two types, the Fraunhofer diffraction and Fresnel diffraction. The first occurs when the source and the target are sufficiently separated from the obstacle or the opening, and the wave fronts are regarded as flat (far field diffraction), the second occurs when the source or the target, or both, are close to the obstacle or opening. In this case the wave fronts are spherical and we are in a situation of near-field diffraction.

The figures or patterns resulting from the observed diffraction at a target, or captured with a detector, are called diffraction patterns and represent a distribution of light intensity for various angles of observation. The observation of this distribution of the intensity of light at a target reveals greater intensity in the direction of wave front and advance a decrease as the angle of view increases.

### 2.3.4 - Young experience

Since Huygens proposed his wave theory of light in 1678 and until there was a clear evidence of the wave nature of light over a century has passed. Thomas Young in 1802 was the person who, for the first time, held such a demonstration, the wave nature of light. In this experiment, presented schematically in Figure 13(a), Young used two openings that let two beams pass of a front of plane wave and monochromatic incident in these openings. These two beams overlapped and interfered creating lit and unlit zones which could be visible at a target [56–67].

Taking into account Figure 13(b) and considering that the point  $P$  is far enough from the two openings  $S_1$  and  $S_2$ , and the distance to the target is much larger than the separation between the openings, the difference between distances  $S_1P$  and  $S_2P$  is equal to the segment ( $\Delta$ ) in the figure. As the target is the distance of openings, the arc  $S_1Q$  can be approximated to a line segment. In this way, the length of the segment ( $\Delta$ ) can be calculated

based on the triangle rectangle  $S_1S_2Q$  (Figure 13(a)). If  $\theta$  is the angle between the plane of the openings and the thread  $S_1Q$  so  $(\Delta)$  is given by

$$\Delta = a \sin \theta \quad (28)$$

where  $a$  represents the distance between the centers of the two slits.

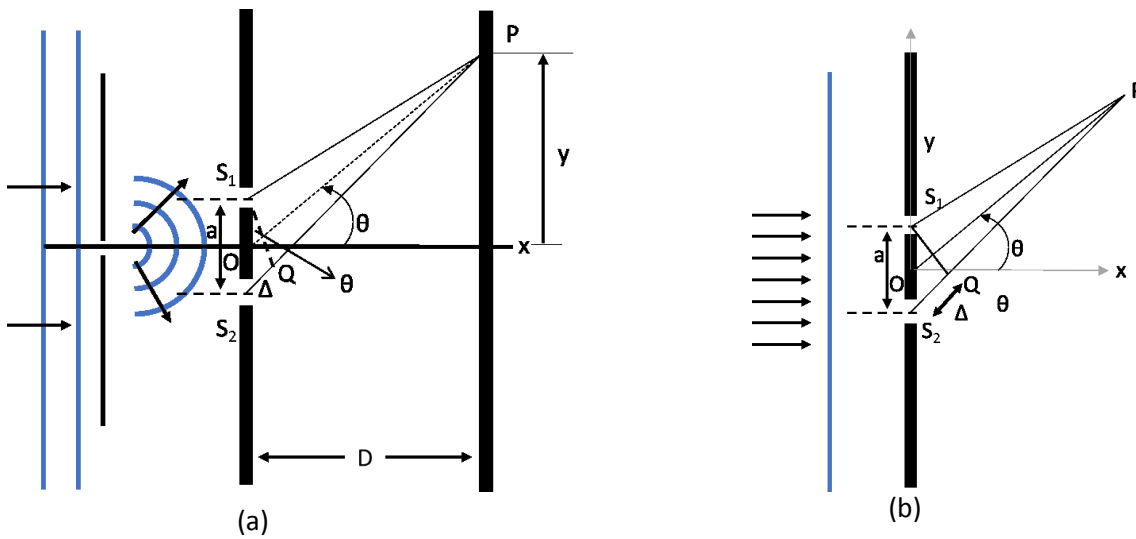


Figure 13 - Schematic representation of Young's experience

Even within the same approach,  $\theta$  can be seen as the angle between the optical axis  $Ox$  and the line segment from the midpoint between the two openings at the point  $P$ . So and within the approximations made the condition of constructive interference in  $P$  (wave fronts in stage) occurs when

$$S_2P - S_1P = \Delta = m\lambda = a \sin \theta \quad (29)$$

While destructive interference (wave fronts in phase opposition) occurs when

$$S_2P - S_1P = \Delta = \left(m + \frac{1}{2}\right)\lambda = a \sin \theta \quad (30)$$

where  $m$  represents the order of interference and can take the values zero or an integer. As the two wave fronts are generated from the same beam they have the same initial phase and the same propagation constants. Thus, the phase difference between the two wave fronts is



due only to the difference of the two wave fronts pathways to reach the point  $P$ . Then you can write that

$$\delta = k(r_1 - r_2) = \left(\frac{2\pi}{\lambda}\right) \Delta \quad (31)$$

where  $r_1$  and  $r_2$  are the distances between  $S_1$  and  $P$  and between  $S_2$  and  $P$ , respectively.

Substituting equation 31 in equation 27 is obtained

$$I = 4I_0 \cos^2 \left(\frac{\pi a y}{\lambda D}\right) \quad (32)$$

where  $y$  represents the height of the optical axis and the point  $P$  and  $D$  represents the distance between the two openings and the target.

The maximum positions of interference occur so for values of  $y$  data by

$$y_m = \frac{m\lambda D}{a} \quad \text{with } \mu = 0, 1, 2, 3, \dots \quad (33)$$

There is a constant separation between adjacent maximum given by  $\Delta y = \lambda D/a$ . The minimum irradiance is situated in intermediate positions between the various consecutive highs. The equations 29 and 30 can infer (except for the case of the most central) that the maximum and minimum position depends on the wavelength. Consequently, when white light falls into two openings, as in Young's experience, the central maxima features white color but superior maxima order features small rainbow-like colors. In this way, Young became the first to determine the wavelengths of visible light and showed what distinguishes physically different colors is its wavelength, in accordance to which Grimaldi proposed about 1665 [60]. Still in relation to Young's experience, provided that the distance between the target and the plan of openings must be large enough (so to say that  $\Delta = a \cdot \sin \theta$ ) is a fundamental condition. This condition is equivalent to the condition that the phase of any elementary wave from the bulkhead is a linear function of distance in the bulkhead. This is the condition for the existence of Fraunhofer diffraction from which the interference produced by two openings is a special case.

### 2.3.5 - Fraunhofer and Fresnel diffraction

Consider the situation in which a punctual source far illuminates a small opening and that the observation is made a target next. In those circumstances, the projected image on the target is practically equal to the opening showing however some fringes on its periphery. Moving it further away, the image seen on the target is still recognizable as the original opening although fringes observed in the periphery are better structured and more visible. This phenomenon is known as Fresnel diffraction or near-field. If the plan of survey is too far away from the aperture it is no longer possible to recognize the shapes of the original object observing a fringe pattern that covers a vast region of the target. Further increasing the distance, there is a variation in the dimensions of the pattern observed and not on its form (Figure 14). This situation corresponds to the Fraunhofer diffraction or distant field. An illustration of the transition between the Fresnel diffraction and Fraunhofer diffraction is shown in Figure 14 for the case of a simple slit.

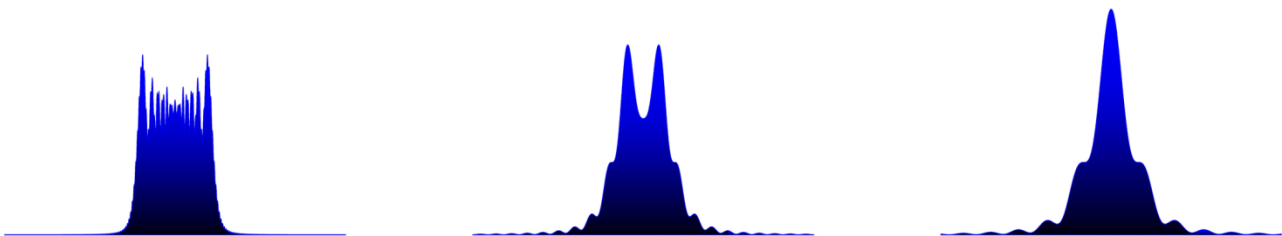


Figure 14 - Transition from Fresnel Diffraction pattern to Fraunhofer Diffraction pattern

The phase of each contribution in a point in space, due to differences in optical paths, is extremely important for the determination of the resulting field. When the wave fronts are virtually flat, the differences of routes can be described by a linear function of two variables. This linearity in the variables of the opening features mathematically the Fraunhofer diffraction regime [56,59]. Fresnel diffraction prevails however whenever the source, the observation point or both are so close to the opening in such a way that the curvature of the wave fronts can no longer be despised [56,59,64].

To determine the relative contribution phases of opening elements for a given observation point  $P$  it is necessary to define the position of all points equidistant from that point (see Figure 15(a)). If the note is flat situated at a distance less than  $R$ , you cannot use flat surfaces as reference but before spherical surfaces. If on the contrary the point  $P$  belongs to a plan situated at a distance greater than  $R$ , such that the maximum deviation between a spherical wave front and a plane wave front ( $\Delta$ ) could be less than  $\lambda/8$ , the difference between the ball and the plan ceases to be important and surfaces may be considered to be flat. The same is true regarding the separation between the light source and the opening. If the light source is in a plane situated at a distance less than  $R$ , they are spherical wave fronts while the source to find more than the  $R$  wave fronts can be considered flat (see Figure 15(b)). The distance  $R$  between the two schemes is known as Rayleigh distance and is given by:

$$R = \frac{b^2}{\lambda} \quad (34)$$

where ( $b$ ) represents the width of the opening, in this case a slit,  $\lambda$  represents the wavelength of the incident radiation and  $R$  is the smallest of distances between the source and the opening and between the opening and the point of observation.

So, the following conditions for the occurrence of Fraunhofer diffraction or Fresnel can establish: Fraunhofer diffraction:  $b^2 < \lambda R$

Fresnel diffraction:  $b^2 \geq \lambda R$

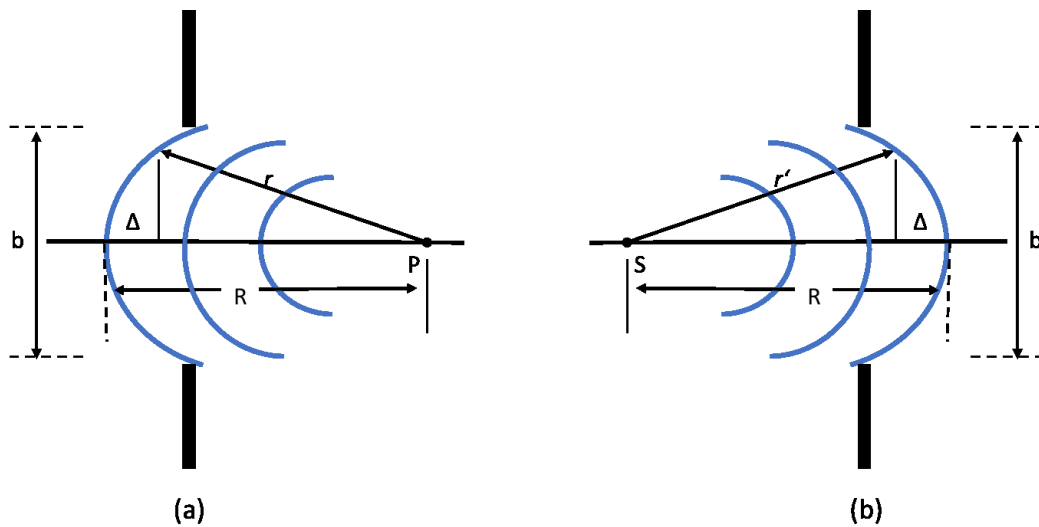


Figure 15 - Difference between a flat wave front and a spherical wave front to diffracted waves (a) and incident waves (b)

The theory associated with Fraunhofer diffraction is much simpler to be treated mathematically than Fresnel diffraction. Experimentally the Fraunhofer diffraction is easily seen by expanding and collimating a beam of light (usually laser) with converging lenses and focuses it later in a target with another convergent lens placed after opening. This type of mount causes the light source and the target is effectively an infinite distance from the aperture.

This dissertation will be considered only the Fraunhofer diffraction because that will serve as a theoretical basis to the realization and understanding of the experimental part. The most well-known examples of Fraunhofer diffraction will be presented and described, diffraction by a slit in particular simple, by a rectangular aperture (square) and by circular openings and eclipsic. The diffraction by a subject where there is only phase variation will be presented and described.

2.3.6 - Diffraction: Simple Slit

The simplest case of diffraction is what results from a simple slit  $b$  wide illuminated by a plane wave front with uniform amplitude (see Figure 16). The slit has a length  $L$  infinity deleting in this way the possibility of existence of diffraction for part of the crack. The resulting diffraction pattern is due solely to the width of the slit.

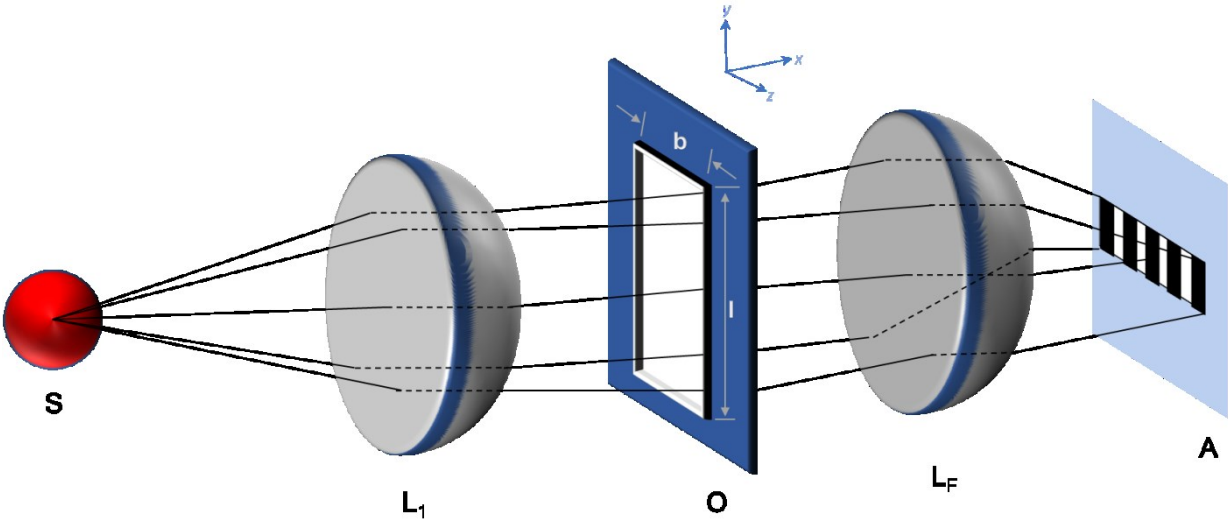


Figure 16 - Schema for generation of the Fraunhofer diffraction pattern for a simple slit in a target.

- S = Source
- L1 and Lf = Lens
- O = Obstacle
- A = Shield

The diffraction pattern of a simple slot is, according to Huygens ' principle, the result of the superimposition of all the spherical wave produced from each point which is the front of plane wave incident on slit. As shown in Figure 17(a) the waves that reach the point  $P$  are out-of-phase with each other due to their different optical paths. A ray passing through the center of the slit and get to the point  $P$  has a different optical path of the lightning to pass by the end of the slit.

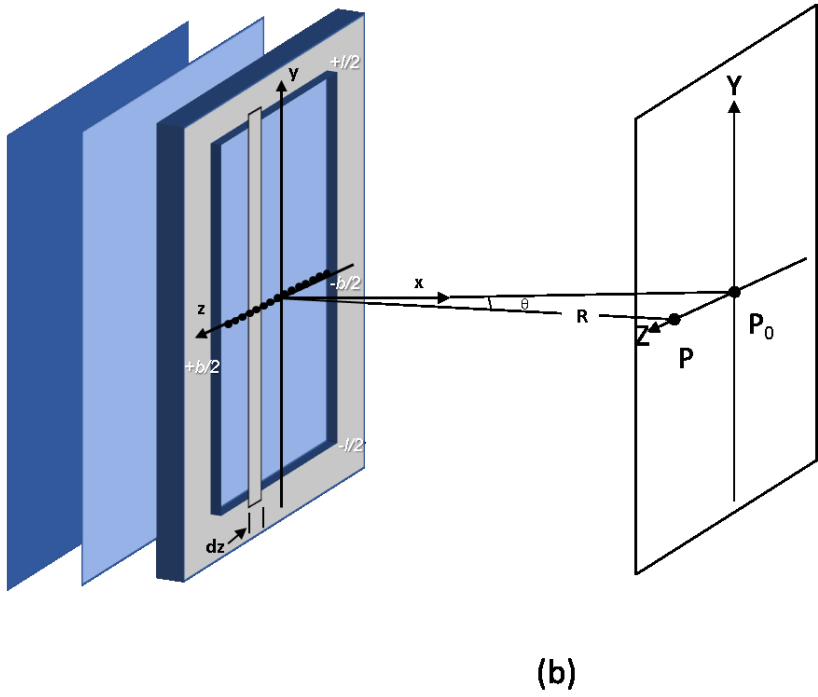
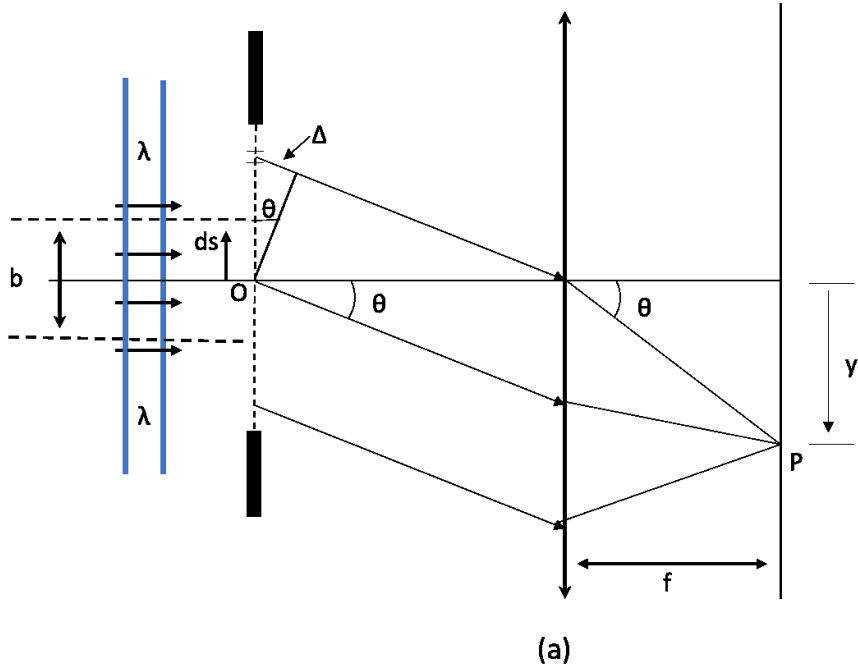


Figure 17 - Schematic representation of the generation of the Fraunhofer diffraction pattern of a simple slot (a) schematic representation of the opening corresponding to a simple slot (b).

The wave front corresponding to the width of the slit represents a continuous set of sources of secondary spherical waves. Each infinitesimal interval  $dz$  (Figure 17(b)) of the wave front can be considered as a source of secondary spherical waves that interfere at the point  $P$  (Figure 17(b)). The waves that reach the point  $P$ , expressed in terms of electric field variation, can be represented by

$$dE_p = \left(\frac{dE_0}{R}\right) e^{i(kR - \omega t)} \quad (35)$$

where  $R$  corresponds to the optical path between the range  $dz$  and the point  $P$ . Considering  $R_0$  is the resulting secondary wave optical path from the center of the slit ( $z = 0$ ), then any other wave from an interval  $dz$  situated at a height  $r$  of the optical axis is given by the expression

$$dE_p = \left(\frac{dE_0}{R}\right) e^{i[k(R_0 + \Delta) - \omega t]} \quad (36)$$

where  $(\Delta)$  represents the optical path difference compared to the wave originates at the point  $z = 0$ . For the amplitude, the optical path difference is not important since  $\Delta \ll R_0$ .

In the meantime, in relation to the phase, as this is extremely sensitive to small variations, it is not possible to neglect the factor  $\Delta$ .

The amplitude of the waves depends on the size of the intervals  $dz$ . When all contributions are added by integration, over the width of the slit, the total effect on  $P$  is obtained. So, it is possible to write

$$dE_0 = E_L dz \quad (37)$$

where  $E_L$  is the amplitude per unit of width of slit to a unit distance. For replacement on equation 36 and considering that the optical path difference is given by the equation 28, has

$$dE_p = \left(\frac{E_L dz}{R_0}\right) e^{i(kR_0 + kz \sin \theta - \omega t)} \quad (38)$$

Integrating the previous equation about the width of the slit and separating the part that represents the amplitude (in brackets) from the part that represents the phase is obtained

$$E_p = \left(\frac{E_L}{R_0} \int_{-\frac{b}{2}}^{\frac{b}{2}} e^{ikz \sin \theta} dz\right) e^{i(kR_0 - \omega t)} \quad (39)$$

Where:

$$E_p = \frac{E_L}{R_0} \frac{1}{ik \sin \theta} \left[ e^{(ikb \sin \theta)/2} - e^{-(ikb \sin \theta)/2} \right] e^{i(kR_0 - \omega t)} \quad (40)$$

Performing

$$\beta = \frac{1}{2}(kb \sin \theta) \quad (41)$$

Is possible to conclude that

$$E_p = \frac{E_L b}{R_0} \text{sinc}(\beta) e^{i(kR_0 - \omega t)} \quad (42)$$

represents the resulting wave which is a simple harmonic wave whose amplitude varies with the position of  $P$  through  $\beta$ . The amount  $\beta$  represents the phase difference between waves emitted from the center of the slit edges. The physical quantity used for the detection of amplitude of the wave is the irradiance as defined by equation 22. So, the expression that reflects the total irradiance is the following

$$I = \varepsilon_0 c \langle E_p^2 \rangle = I_0 \text{sinc}^2(\beta) \quad (43)$$

where  $I_0$  includes all factors constant and is given by  $I_0 = \frac{1}{2} \varepsilon_0 c (E_L b / R_0)^2$ . Through this equation is possible to trace the irradiance variation with height, relative to the optical axis, on target.

The maximum irradiance  $I_0$  occurs when the function  $\text{sinc}(\beta)$  reaches its maximum value, when  $\text{sinc}(\beta)=1$ , corresponding to  $\beta=0$ , following equation 41, that leads to  $\theta=0$ . In this case, the point of maximum irradiance is the central point being the corresponding maximum named central maximum or zero-order. The central maximum represents the point at which all the secondary waves have the same phase. From this point, the irradiance decreases until it reaches a minimum value ( $I=0$ ) then increasing until it reaches a maximum value which follows another and so on to both sides of the central point. The diffraction pattern is symmetric with respect to the central point.

The minimum irradiance occurs at the points for which  $\text{sinc}(\beta)=0$ , that is, when  $\sin \beta=0$ .

In this case:  $\beta = \pm \pi, \pm 2\pi, \pm 3\pi, \dots$ . From equation 41 results so that  $\frac{1}{2}(kb \sin \theta) = m\pi$  or  $m\lambda = b \sin(\theta)$ . But as  $\sin \theta = y/f$  (small angles approximation) the minimum points occurs on the target where



$$y \cong \frac{m\lambda f}{b} \quad \text{with } m = \pm 1, \pm 2, \pm 3, \dots \quad (44)$$

The secondary maximum irradiance does not occur exactly on midway between two successive lows being diverted towards the central diffraction maximum pattern of an amount that decreases with the increase of  $\beta$  [56]. The secondary maximum diffraction pattern matches with the maximum of the sinc function, to satisfy the condition points

$$\frac{d}{d\beta} \left( \frac{\text{sinc } \beta}{\beta} \right) = 0 \quad (45)$$

Solving the previous equation, the nonlinear equation is obtained

$$\beta = \tan \beta \quad (46)$$

Thus, the values for occurrence of secondary Maxima are the solutions of the equation 46,  $\beta = \pm 1.43\pi, \pm 2.46\pi, \pm 3.47\pi$  and so on.

The Fraunhofer diffraction pattern of one slit (Figure 18) presents a series of lines perpendicular to the direction of the length of the slit. If the source on time were replaced by linear incoherent source diffraction pattern extended giving rise to a number of bands. Any point of the linear source generates a standard independent diffraction.

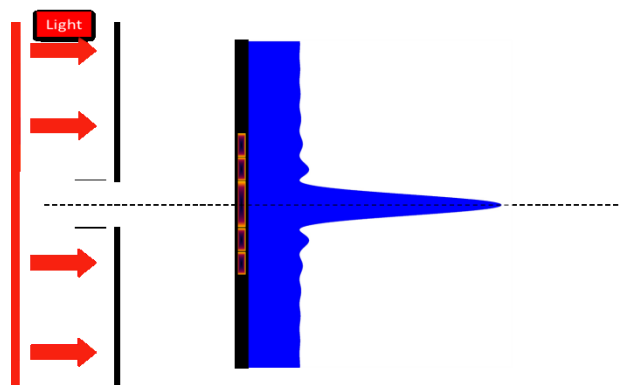


Figure 18 - Single Slit and the corresponding Fraunhofer diffraction pattern (Schematic Representation)

The dimensions of the diffraction pattern are inversely proportional to the size of the slit (equation 44). Considering the size of the slit increasing, the diffraction pattern contracts until

on the edge; then, for a slit of infinite dimensions, the diffraction pattern is reduced to a point without dimensions, becoming a delta function.

In case of a double slit (Figure 19), each slit raises on the target a typical diffraction pattern of a simple slit which although similar in magnitude can have significant variations of phase. At any point in the target the contributions of the two slits overlap and due to the existing coherence between secondary waves of two openings will occur (Young's for two slits) beyond the diffraction by single slit [56,58,61,64]. In the case of the flat wave front relate normally to the plane of the slits, the secondary waves are emitted in the process, being the interference pattern at a particular point determined by differences in optical paths between the waves emitted by the two slits. The resulting pattern is formed by the interference pattern of two modulated by diffraction pattern openings of single slit. Also in Figure 19 is observed the single slit envelope that is shown by the red line.

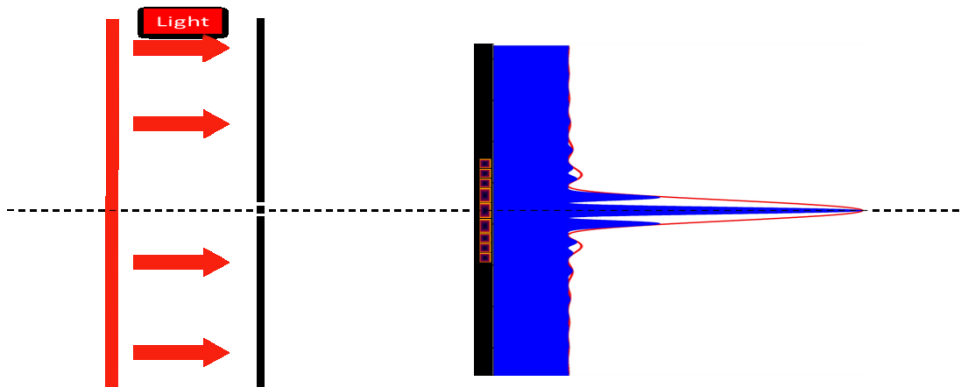


Figure 19 - Double slit and the corresponding Fraunhofer diffraction pattern (Schematic Representation)

The expression of irradiance for a double slit is obtained based on the analysis of a single slit with slight reformulations. Returning to equation 38, the amplitude in the case of the double slit is given by

$$E_p = \left( \frac{E_L}{R_0} \int_{-1/2(a+b)}^{-1/2(a-b)} e^{ikz \sin \theta} dz + \frac{E_L}{R_0} \int_{1/2(a-b)}^{1/2(a+b)} e^{ikz \sin \theta} dz \right) e^{i(kR_0 - \omega t)} \quad (47)$$

where  $a$  represents the split between the slits and  $b$  the width of the slits. Solving this integral and doing

$$\beta = \frac{1}{2}(kb \sin \theta) \quad (48)$$

$$\alpha = \frac{1}{2}(ka \sin \theta) \quad (49)$$

It is obtained:

$$E_p = \frac{2E_L b}{R_0} \text{sinc}(\beta) \cos \alpha e^{i(kR_0 - \omega t)} \quad (50)$$

Thus, the irradiance can be expressed by

$$I = 4I_0 \text{sinc}^2(\beta) \cos^2 \alpha \quad (51)$$

Where  $I_0$  is given by:

$$I_0 = \frac{\epsilon_0 c}{2} \left( \frac{E_L b}{R_0} \right)^2 \quad (52)$$

The diffraction minima occurs when  $\beta = m\pi$ , with  $m = \pm 1, \pm 2, \dots$ , or as a function of  $\theta$  when

$$B \sin(\theta) = m\lambda. \quad (53)$$

The interference Maxima occurs when  $\alpha = p\pi$ , with  $p = \pm 1, \pm 2, \dots$  when

$$A \sin(\theta) = p\lambda \quad (54)$$

When the two previous conditions are satisfied to the same point, that is, to the same value of  $\theta$ , the corresponding fringe to a maximum of interference is missing. The condition for the existence of missing orders is obtained through the radius of minimum conditions of diffraction and interference maximum, that is,  $a = (p/m)b$  or  $\alpha = (p/m)\beta$ .

For the case of  $N$  slits (Figure 20(a)), the equations used for two slits are widespread with its integration on  $N$  slits. So the final irradiance is given by the following expression

$$I = I_0 \left( \frac{\sin \beta}{\beta} \right)^2 \left( \frac{\sin N\alpha}{\sin \alpha} \right)^2 \quad (55)$$

The factor  $\beta$  represents the envelope of the term diffraction, while the factor in  $\alpha$  describes the term of interference between slits. The interference term consists of primary and secondary maximums equally spaced between which there are corresponding to minimum irradiance points. The global standard is the result of the product of these two terms. In Figure 20(b) presents the horizontal profile of diffraction pattern.

The main interference maxima occurs whenever the numerator and denominator of the interference term of the equation 55 tends to zero, that is, when  $\alpha = 0, \pi, 2\pi, \dots$ , while the minimum of interference (zeros of irradiance) occurs whenever the numerator of the interference term of the equation 55 is zero and the denominator is not zero, that is, whenever  $N\alpha$  take the values  $0, \pi, 2\pi, \dots, p\pi$ . Except for the cases when  $p$  is equal to  $0, N, 2N, \dots$ , once for these situations the numerator and denominator assumes zero value with maximum interference principal then.

The secondary maxima occur about midway between two minima, approximately when  $\sin \theta = \pm \frac{3}{2} \frac{\lambda}{Nd}, \pm \frac{5}{2} \frac{\lambda}{Nd}, \dots$ . The irradiance to these secondary maxima is approximately  $1/22$  of the maximum main irradiance [56]. Between two main maxima there are  $N - 1$  minima equally spaced apart by  $N - 2$  secondary maxima. When the number of slits increases, the number of secondary maxima also increases, causing the main maximum are increasingly thin. So, for a large number of slits, if the font used is monochrome, the pattern observed in a target will be composed mainly of bright lines, distinct and spatially well resolved. If the light source is not monochrome, the diffraction pattern features a central bright line corresponding to the central maximum or zero-order, showing maximum orders consisting of colored lines corresponding to the various wavelengths which constitute the source of light. This is the working principle of diffraction grids widely used in spectroscopy. Diffraction networks are typically composed by several hundred lines (slits) per millimeter. As higher as this number is, greater is the resolution obtained with the diffraction grid, that is, the stripes corresponding to the spectrum of a given light source will be better visualized.

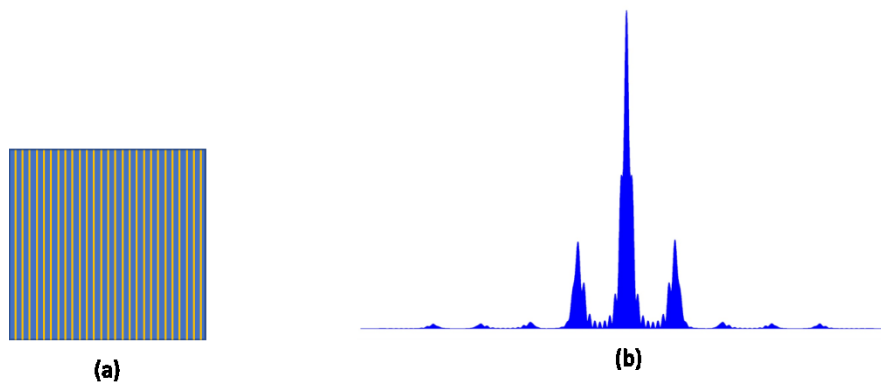


Figure 20 - Diffraction Grid (a) and Horizontal Profile (b) of Diffraction grid in a Fraunhofer Pattern

### 2.3.7 - Diffraction – Theory for rectangular apertures

A single slit, in the study of Fraunhofer diffraction was carried out based on the approximation that the length of the slit was infinitely superior to its width, so the incident wave front undergoes a scattering solely in the perpendicular direction to the length of the slit. However, if the length and width of the gap have reduced and have comparable dimensions, the wave front is spreading in both of the vertical and horizontal direction. The diffraction pattern will be the combination of these two effects (Figure 21).

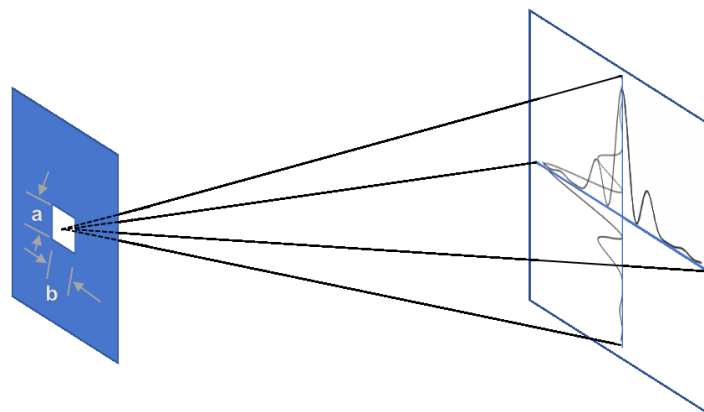


Figure 21 - Schematic representation of the diffraction pattern generation for a rectangular opening of comparable dimensions.

The more general situation of an arbitrary aperture is shown in Figure 22.

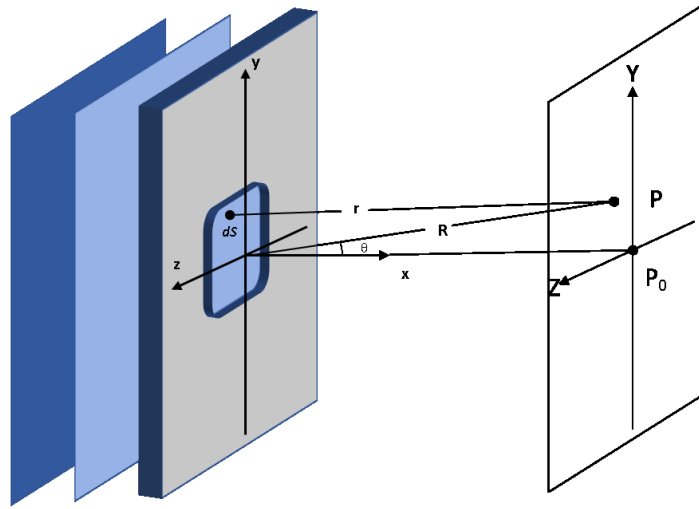


Figure 22 - Schematic representation for an arbitrary gap

In accordance with the Huygens principle, each differential element of area  $dS$  of the surface from an aperture can be considered as being filled by coherent point sources. If the linear dimensions  $dS$  are small, relatively compared to the wavelength, all secondary waves will be on phase at the point  $P$ , constructively interfering. This result does not depend on  $\theta$  and  $dS$  can be considered as a source of spherical waves. The optical perturbation on  $P$  is obtained using equation 35. Being  $dE_0 = E_A dS$  the equation 35 can be written as

$$dE_p = \left(\frac{E_A}{r}\right) e^{i(kr - \omega t)} dS \quad (56)$$

The distance between  $r$  and  $dS$  with coordinates  $(0, y, z)$ , and  $P$  with coordinates  $(X, Y, Z)$ , which is represented in Figure 22 is given by

$$r = [X^2 + (Y - y)^2 + (Z - z)^2]^{1/2} \quad (57)$$

Developing previous equation and knowing the distance between  $P$  and  $O$  is given by  $R = (X^2 + Y^2 + Z^2)^{1/2}$  that develop:

$$r = R \left[ 1 + \frac{(y^2 + z^2)}{R^2} - 2(Y_y + Z_z)/R^2 \right]^{1/2} \quad (58)$$

Once  $R$  is much larger than the dimensions of the aperture, the second term of the previous equation can be despised. By the binomial expansion and considering only the first two terms of the expansion is obtained

$$r = R[1 - (Y_y + Z_z)/R^2] \quad (59)$$

and replacing  $r$  in the equation 56:

$$E_p = \frac{E_A e^{i(kR - \omega t)}}{R} \iint_{\text{aperture}} e^{ik(Y_y + Z_z)/R} dS \quad (60)$$

More specifically to the case of a rectangular aperture in Figure 23 and being  $dS = dy \cdot dz$  :

$$E_p = \frac{E_A e^{i(kR - \omega t)}}{R} \int_{-b/2}^{b/2} e^{ikY_y/R} dy \int_{-a/2}^{a/2} e^{ikZ_z/R} dz \quad (61)$$

After the integration,

$$E_p = \frac{AE_A e^{i(kR - \omega t)}}{R} \left( \frac{\sin \alpha}{\alpha} \right) \left( \frac{\sin \beta}{\beta} \right) \quad (62)$$

Where  $\alpha = kaZ/2R$  and  $\beta = kbY/2R$ , or as a function of  $\theta$ , if  $\alpha = (ka/2)\sin\theta$  and  $\beta = (kb/2)\sin\theta$ .

So, the irradiance can be determined by

$$I = I_0 \left( \frac{\sin^2 \alpha}{\alpha} \right)^2 \left( \frac{\sin^2 \beta}{\beta} \right)^2 \quad (63)$$

Where  $I_0$  is the irradiance at the point  $P_0$  and that is given by

$$I_0 = \frac{\epsilon_0 c}{2} \left( \frac{AE_A}{R} \right)^2 \quad (64)$$

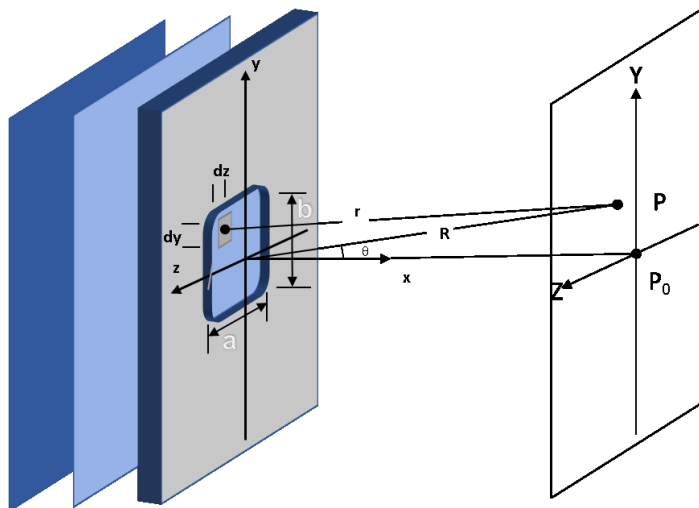


Figure 23 - Schematic representation for a rectangular aperture.

When  $\alpha=0$  or  $\beta=0$ , equation 63 takes the form of irradiance for a simple slit.

When  $\alpha$  or  $\beta$  are non-zero integers multiples of  $\pi$ ,

$$Y = \frac{m\lambda R}{b} \quad (65)$$

Or

$$Z = \frac{p\lambda R}{a} \quad (66)$$

the irradiance given by equation 64 takes the zero value and minima irradiance arises for these points. Secondary maxima is located approximately midway between two minims, i.e. for  $\beta = \pm 3/2\pi, \pm 5/2\pi, \dots$  and the same happening to  $\alpha$ .

For each secondary maxima  $\sin(\beta) = 1$  and as on the axis ( $\beta$ ), since that  $\alpha=0$ ,  $(\sin\alpha/\alpha) = 1$  the irradiance are approximated by  $I/I_0 = 1/(\beta)^2$ . In the same way along the axis  $\alpha$  relative irradiances are  $I/I_0 = 1/\alpha^2$ . Thus, the irradiance radius decreases from 1 to 1/22, to 1/62, to 1/122, etc

### 2.3.8 - Diffraction – Theory for circular apertures

The Fraunhofer diffraction patterns of a circular aperture have important practical applications, particularly in the study of instruments and optical systems, since most of the lenses and apertures are circular. The image of a distant pinpoint source formed by positive lens, free of aberrations, is never a point but rather a Fraunhofer diffraction pattern (resolution limit). The result is a series of Maxima and minima circular and concentric, where the central maximum is known as the Airy disk.



Considering a circular opening with radius  $a$ , starting on  $O$  and with perpendicular axes  $O_z$  and  $O_y$ , such as presented in Figure 24, and assuming that the distribution of the light through the opening is constant and equal to  $E_0 = E_A/R$  is possible to determine the resulting disturbance on a  $P$  point from a distant target.

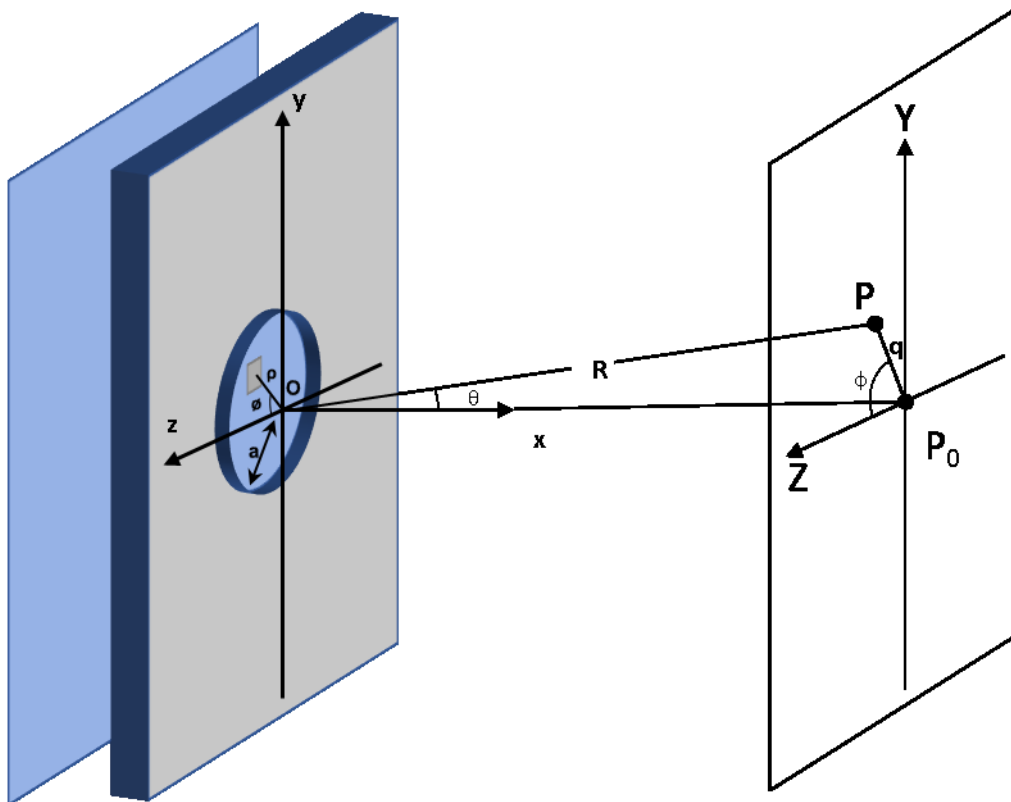


Figure 24 - Schematic representation of a circular aperture.

As previously shown, the expression for the optical perturbation  $P$  resulting from an arbitrary aperture in the case of a far away target is given by the equation 60. In this case, due to the symmetry of the opening it is convenient to use polar spherical coordinates instead of rectangular coordinates. If  $(\rho, \phi)$  are spherical polar coordinates in terms of aperture plane and  $(q, \Phi)$  polar spherical coordinates in the plane of observation of diffraction pattern, the relationship with the rectangular coordinates is given by the following expressions

$$z = \rho \cos \phi \text{ and } y = \rho \sin \phi \quad (67)$$

$$Z = q \cos \Phi \text{ and } Y = q \sin \Phi \quad (68)$$

In this new coordinate system the surface element is given by the expression  $dS = \rho d\rho d\phi$ .

Substituting these expressions into the equation 60 is obtained

$$E = E_0 e^{i(kR - \omega t)} \int_{\rho=0}^a \int_{\phi=0}^{2\pi} e^{i(k\rho q/R) \cos(\phi - \Phi)} \rho d\rho d\phi \quad (69)$$

Due to the axial symmetry, the result is independent of  $(\Phi)$ . So, whereas  $\phi=0$ , to simplify the equation,

$$E = E_0 e^{i(kR - \omega t)} \int_{\rho=0}^a \int_{\phi=0}^{2\pi} e^{i(k\rho q/R) \cos(\phi)} \rho d\rho d\phi \quad (70)$$

In assumption that

$$J_m(u) = \frac{i^{-m}}{2\pi} \int_0^{2\pi} e^{i(mv + u \cos v)} dv \quad (71)$$

is the Bessel function of order  $m$ , the equation 70, for  $m=0$ , reduces to

$$E = 2\pi E_0 e^{i(kR - \omega t)} \int_0^a J_0(k\rho q/R) \rho d\rho \quad (72)$$

To calculate this integral is used a property of Bessel functions (recurrence relation) expressed mathematically by

$$\frac{d}{du} [u^{m+1} J_{m+1}(u)] = u^{m+1} J_m(u) \quad (73)$$

that for integration and for  $m=0$  reduces to

$$u J_1(u) = \int_0^u u' J_0(u') du' \quad (74)$$

From the equation 72 with the change of variable  $u' = k\rho q/R$  and  $d\rho = (R/kq) du'$  is obtained

$$E = 2\pi E_0 (R/kq)^2 e^{i(kR - \omega t)} \int_0^{kaq/R} u' J_0(u') du' \quad (75)$$

Using the equation 74, the equation 75 can be expressed by

$$E = 2\pi \alpha^2 E_0 e^{i(kR - \omega t)} \left[ \frac{J_1(kaq/R)}{kaq/R} \right] \quad (76)$$

Assuming  $R$  remains constant throughout the space of the diffraction pattern, the irradiance will come given by

$$I = I_0 \left[ \frac{J_1(kaq/R)}{kaq/R} \right]^2 \quad (77)$$

Where  $I_0 = (\epsilon_0 c^2) [(\pi a^2)^2 E_A^2 / 2R^2]$ , which is the same result that was obtained for an rectangular aperture. In assumption that  $\sin \theta = q/R$ , the previous equation can be written as a function of  $\theta$  as

$$I = I_0 \left[ \frac{2J_1(ka \sin \theta)}{ka \sin \theta} \right]^2 \quad (78)$$

This equation was derived for the first time by Sir George Biddell Airy in 1835 and represents a distribution with a very bright central maximum known as the Airy disk. This central disc is surrounded by a dark ring corresponding to the first zero of the Bessel function.

This first minimum occurs when  $u=3.83$ , that means,  $kaq/R = 3.83$ . Radio  $q_1$  that goes to the Center of the first minimum may be considered as the limit of the Airy disk. The minimum of higher order when occur  $kaq/R= 7.02, 10.17, 13.32$ , etc. The first minimum is then given by

$$q_1 = 1.22 \frac{R\lambda}{2a} \quad (79)$$

where  $2a$  represents the diameter of the aperture. The secondary maxima occurs for values of  $u$  that satisfy the condition

$$\frac{d}{du} \left[ \frac{J_1(u)}{u} \right] = 0 \quad (80)$$

Through the recurrence relation between Bessel functions  $\frac{d}{du} [u^{-m}J_m(u)] = u^{-m}J_{m+1}(u)$  is

$$\frac{d}{du} \left[ \frac{J_1(u)}{u} \right] = -\frac{J_2(u)}{u} \quad (81)$$

So, to satisfy the equation 80,  $J_2(u)=0$ , this situation occurs when  $u$  is equal to 5.14 , 8.42 , 11.6 , etc.

Replacing  $u$  by 0 , 5.14 , 8.42 and 11.6 and knowing the corresponding values for  $J_1(u)$  , the radius of the irradiance of a diffraction pattern circular opening for the secondary maximum decreases to 1.75% of the maximum value for the first secondary maximum, to 0.42% for the second and to 0.16% for the third, etc.

Comparing the results obtained for the Fraunhofer diffraction from a circular aperture with those obtained from a rectangular aperture, is verified that the minima to the rectangular aperture are equally spaced, occurring for  $\pi, 2\pi, 3\pi, 4\pi, 5\pi, \dots$  while for a circular aperture the minima occurs for  $1.220\pi, 2.233\pi, 3.238\pi, 4.241\pi, 5.243\pi$  etc. Thus, the diffraction pattern for a circular aperture doesn't show equidistant values to the minima of each other,

note that with the increase of  $q$ , the minima or maxima adjacent separation tends to a constant value equal to  $\pi$ .

These concepts about the theory of interference and diffraction were presented and discussed and several wave equations of one, two and three dimensions were described, as well as the principles of overlapping oscillations, the Huyghens principle and the experiment of Young.

Emphasis has been placed on the Fraunhofer diffraction since it is one of the theories that underlie this dissertation. For this reason, the phenomenon of Fraunhofer diffraction produced both by the general apertures (single, double, rectangular aperture and circular aperture) has been discussed and deepened. These openings are fundamental since, being this dissertation dedicated to the study of the recognition of the optical pattern of the micro-structure coatings, specially focused on riblet structures, the base of theory for this study is the model that maintains that any regular geometry where the optical theory is applied to describe the pattern acquired by an optical detector embedded on a laser sensor device can be theoretically defined and developed.

**Chapter 3 - Objectives**

This dissertation aims at developing evaluation criteria to validate the applied software outputs in order to build a reliable computational tool to support analysis and making decisions in aviation industry production and maintenance, specially applied on micro-structured coatings evaluation, and, in this particular case, taking riblet based structured coatings as object of study.

Using the support of a laser sensor device setup, developed at Fraunhofer – IFAM, a computational tool was developed and evaluated, approaching theoretical definitions related to optics, to identify the surface status of micro-structured coatings. The main identified criteria were summarized to be exploiting in further studies and applications.

Summarizing, the main objective of this dissertation is:

- Development of Computational Analysis Criteria Based on a Laser Sensor Device to Identify the Surface Status of micro-structured Coatings for Aerospace Industry

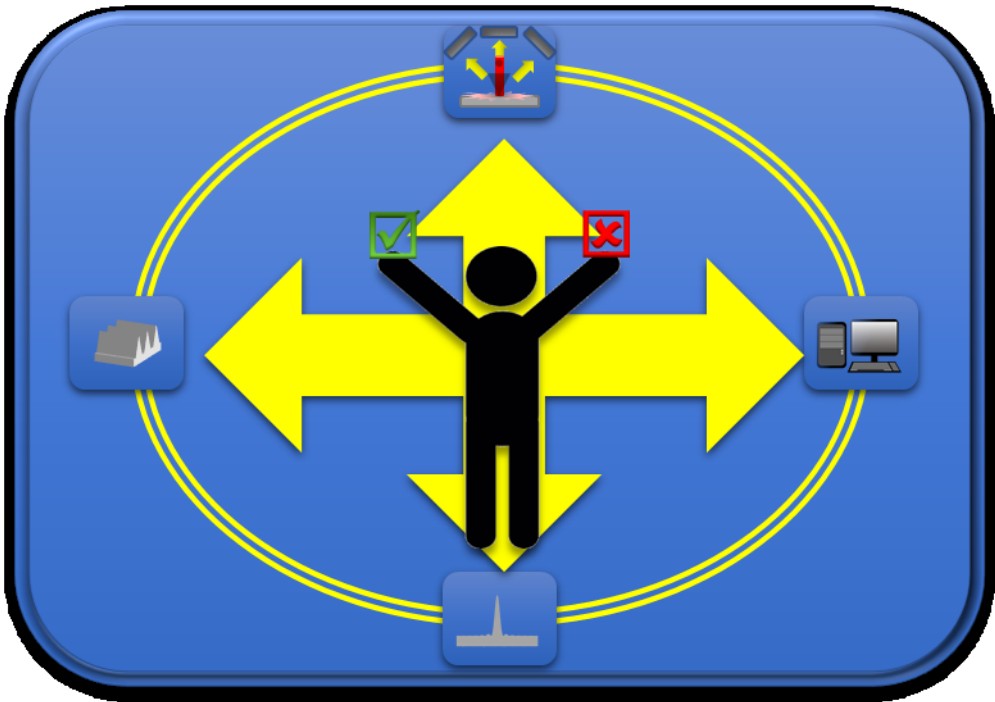

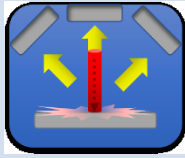




Figure 25 - Integration Process to Analysis Criteria Evaluation of the Proposed Technique

### Chapter 3 – Objectives

---

In order to reach the aiming, this dissertation intends to describe and accomplish the following specific targets:

	Graphical reproduction of a micro-structured surface based on pre-determined geometrical parameters.
	A graphical renderization of the laser light incidence on the surface and respective reflection and hitting on the detectors, computationally reproducing a pre-determined laser sensor device and specific parameters of the device setup.
	Validation of the theoretical findings, implementing the calculations in a computational tool to reproduce the expected intensity acquired by the detectors and, based on this, to be a support to evaluate and describe the analysis criteria to be followed and improved on further prototypes and studies.
	Description of the analysis criteria found and its application in the process of comparison and identification of the surface status.

To finish this objectives chapter, in accomplishing the proposed objectives, this work aims to contribute to current interdisciplinary studies, in this particular instance, computational science, physics and engineering.

### Chapter 4 - Boundary Conditions

The proposed methodology to identify and validate the guidelines to evaluation criteria of micro-structured surface status performs the calculations using Object Oriented Programming (OOP), based in a code developed in Java language and supported by a consistent Database Management System (DbMS). In order to be applied in production and maintenance lines on aviation industries, it is necessary to provide specific tools and techniques based on computer science field with the intention of support making decision on quality assurance of the structured coatings.

First step to reach the target is to build a graphical representation of the surface. The original geometry of the riblet structured surface defined in this dissertation is based on the structure developed by Fraunhofer – IFAM, as cited by Stenzel et al [3]. The model consists in sharp-peaked riblets whose characteristics are presented in Figure 26, with the following characteristics: triangular shape, distance between bottom center riblets ( $d_R$ ), height ( $h$ ) of the riblet and angle of the riblet tip ( $\alpha$ ).

The riblets are generated one by one, following cartesian coordinates in space and defined according to Equation 82 and shown in Figure 26:

$$X_r = 2 * h * \tan(\alpha/2) \quad (82)$$

Where

$X_r$  = riblet width

$h$  = height of the riblet

$\alpha$  = angle of the riblet tip

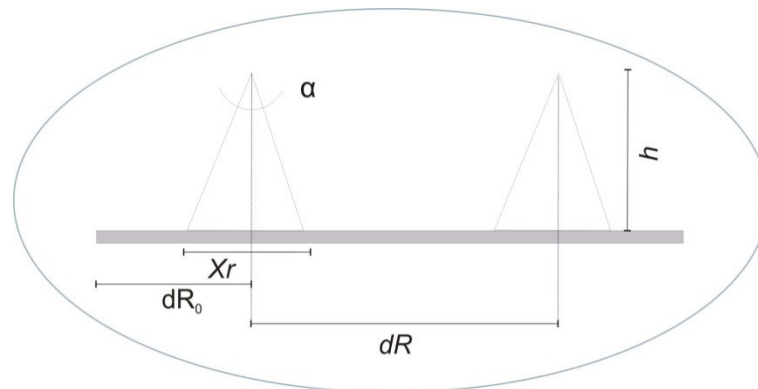


Figure 26 - Sketch of the intact riblet modeling

The original geometry starts in a plane section, with the half measure of the distance between riblet tips, as:

$$dR_0 = dR/2 \quad (83)$$

Where  $dR$  is the distance between riblet bottom centers.

Aiming to reproduce the status of the surfaces on airplanes with riblet coating applied, rebuilding the riblet geometry in degraded state is necessary. In this dissertation, a pattern of degradation is considered to be able to validate the output data and a total degradation of the structured coating is the investigated degradation pattern used as test approach to the calculations. A total degradation, considering totally smooth surface of the sample, is the easiest case to validate the calculations and support the further research steps. This part of the work is the software development to perform analysis and treatment of output data provided by a laser sensor (Figure 7) defined by Imlau et al [8]. The computational tool is used to interpret the obtained diffraction patterns and as a way to simulate the structured surface status from a given pattern. Thus, the software is developed to generate consistent information for analysis and decision-making regarding the surface structure and its maintenance.



A previous study developed by Imlau [8] underlying the performed calculations seeks to validate the results obtained in the current dissertation, where the findings can be theoretically grounded by other calculation approaches, for instance using Mathematica software.

The theory behind the work consists of OOP encapsulation techniques and abstraction concepts in order to incorporate the laser and surface characteristics within the code in appropriately designed objects, classes and subclasses. The OOP abstraction is the key for the code design and the reflection of the laser beam is the key to evaluate the integrity of the riblet surface.

In this stage the relevant attributes of optical phenomena, surface characteristics and their interactions have been designed and not needed features have been discarded. The resulting computational tool provides a user friendly graphical environment. The visualization interface allows developers and final users to set up different platforms for analyses accordingly to their requirements. Scattering intensity distributions obtained experimentally and through the computational tool are presented. They are obtained by intact surfaces and for different surface degradation levels and patterns, varying parameters as incidence angle and beam wavelength.

Most part of the laser characteristics are related to the Huygens-Fresnel behavior, that means, the wave will behave mainly as a spherical wave. The laser beam is a monochromatic light, it has a coherent pattern and it is in accordance with the experiments of Thomas Young (Slit experiment) [68]. The calculations of the intensity are related to the properties of the laser system:

<b>Wave length</b>	632.8nm
<b>Resolution</b>	2048 pixels (1 pixel ≈ 14μm)
<b>Angular Frequency</b>	2,97.1015 rad/s
<b>Distance between sample and the central detector</b>	40 cm

Table 5 Analysis parameters

These parameters were applied in two equations to be validated. The first equation (equation 84) is given by the electric field equation and the second equation (equation 85) is given by the calculations using Fresnel diffraction theory.

$$E_p = E_0 * \sin(\omega t + \varphi) \quad (\text{Sinusoidal wave}) \quad (84)$$

$$I_p = \frac{I_0}{2} \left[ \left( \sum_{i=1}^n C(U_{2i}) - \sum_{i=1}^n C(U_{2i-1}) \right)^2 + \left( \sum_{i=1}^n S(U_{2i}) - \sum_{i=1}^n S(U_{2i-1}) \right)^2 \right] \quad (85)$$

Related to equation 84, intensity calculated in a point p on detector is obtained by the square of the electric field calculated, as demonstrated on equation 86:

$$I_p = E_p^2 \quad (86)$$

Assumption is made that  $\omega t$  is a variation between  $-2\pi$  and  $2\pi$ , and  $\varphi$  is a relation between a reference point on detector and the amount of calculations to the surface, and is assumed that  $E_0$  is equals 1.

Using Equation 84, starting from Fresnel integration, a diffraction pattern is calculated which should be acquired by the detectors. Applying Fresnel integration on the equation, in combination with transcendental functions with complete tables of values, this functions can be calculated beyond Euler spiral [69], which is a geometric representation of Fresnel integration in a complex plan.

Nowadays, these integrations can be fast solved using computational tools. Reis et al. [70] used this approach to characterize a diffraction grid with n non-symmetric slits and arbitrary

widths, and the results can be a base to further steps of this research, which will introduce more detailed structured surfaces, considering variations on intensity patterns acquired by detectors, aiming characterization of the analyzed samples.

Equation 84 assumes that  $n$  is the number of reflections to a central detector without interference, and  $U_2$  is related to calculations taking into account the last position of reflection on surface for each continuous reflection and  $U_{2-1}$  is related to calculations taking into account the first position of reflection on surface for each continuous reflection, as shown in Figure 27 and described on equation 84.

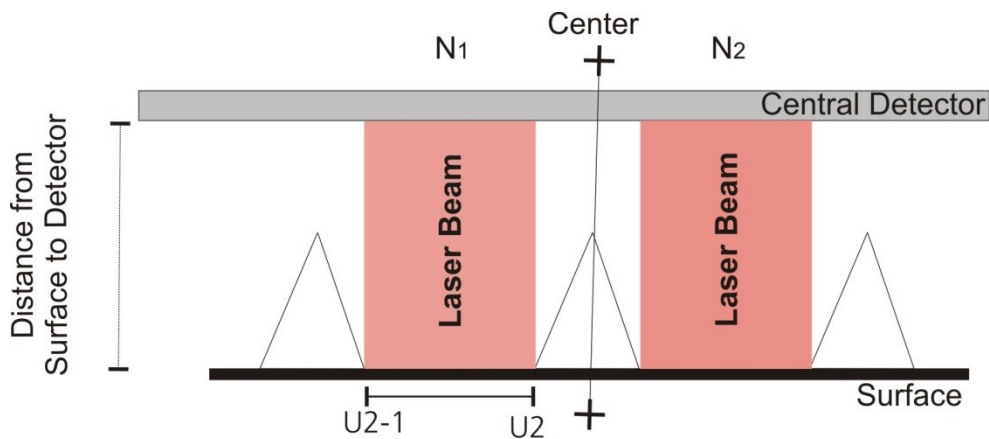


Figure 27 - Schematic representation of the Reflection in a riblet structure, considering parameters to be input in the integration of Fresnel Equation

To apply the proposed techniques, the computational tool is setted with the main parameters to virtually build a sample with the characteristics used to perform riblets at Fraunhofer Institute-IFAM, and to be able to change the main parameters as needed to simulate different types of riblets.

The main parameters are: height of the riblet ( $h$ ); distance between riblets ( $d$ ), which is related to the distance between bottom centers of the riblets; angle at the tip of the riblet ( $\alpha$ ), length ( $x$ ) and the width ( $y$ ) of the sample.

The structure of the laser beam is filled in the next step and is based in a code previously developed by Vriesman [71]. The user should input the parameters to set the laser incidence

## Chapter 4 – Boundary Conditions

and the laser reflection will be graphically reproduced. The main parameters are the initial position of the laser ( $I_{x0}$ ), related to the position on the x axis of the original geometry; the number of the laser beams ( $I_{xn}$ ); and the distance ( $I_d$ ) between the laser beams; all these parameters are saved to generate a 2D visualization of the sample with the laser beam incidence and the reflection of the beams. In this step all beam incidences and reflections are calculated, which allows building a 2D visualization of the structure (Figure 28 and Figure 29). In Figure 28 (A) is represented the laser reflection to the central detector, in a  $0^\circ$  reflection. In Figure 28 (B and C) are represented the laser reflection to the lateral detectors in  $\pm 45^\circ$  degrees reflection. In Figure 29 is shown a graphical visualization generated by the computational tool, representing the laser reflection on  $0^\circ$  reflection (yellow),  $-45^\circ$  reflection (blue) and  $+45^\circ$  reflection (green).

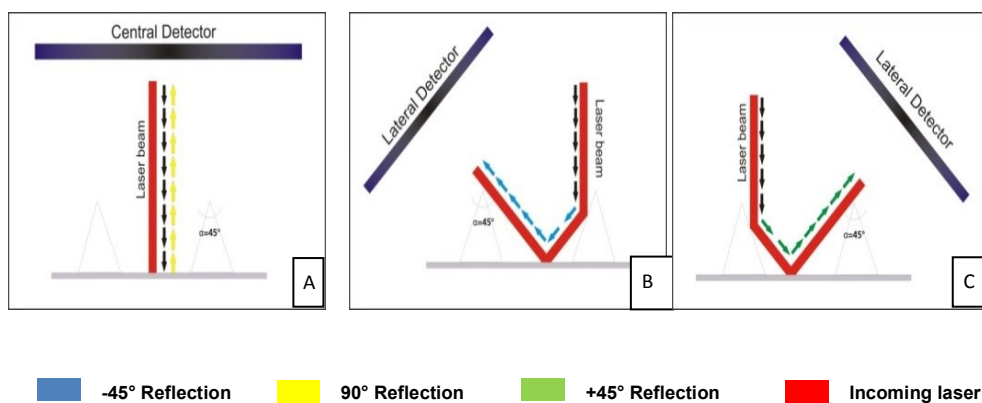


Figure 28 - Schematic representation of the interaction of light with the intact riblet surface. A): vertical incidence on the surface. The beam is reflected back to the central detector. B), C): Interaction with a riblet flank. By reflection, the beam is projected in the direction of  $45^\circ$  to the base of the surface and then follows to the lateral detectors.

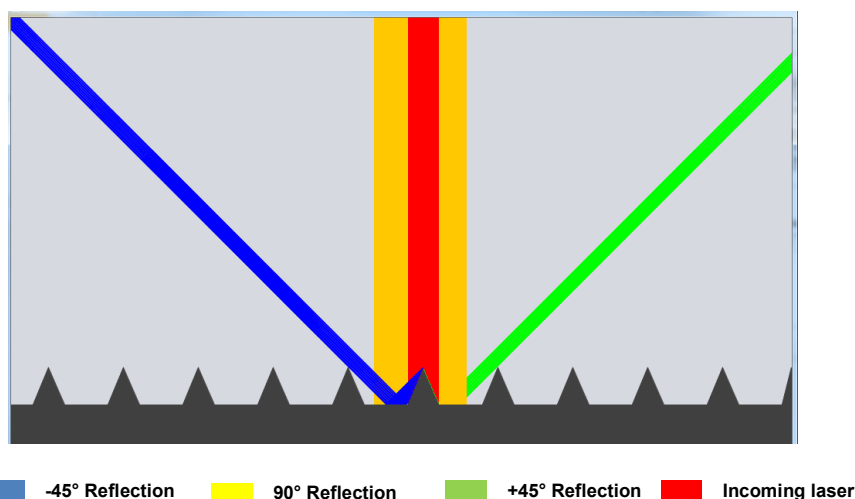


Figure 29 - 2D Plot –  $120\ \mu\text{m}$  laser spot reflection – Intact structure – Generated by computational tool

The riblet degradation is simulated in the next step. At this stage of development, set the degradation as a regular degradation with a perfect flat cut on the tip of the riblet.

The percentage of degradation varies from 0% to 100%, related to the percentage for the exact point on the structure of the riblet where the degradation will start, that is, 100% is the maximum point to degradation. On Figure 30 a riblet structure surface with 50% of flat degradation is presented, a completely degraded riblet structure (100% of degradation) and an intact riblet structure.

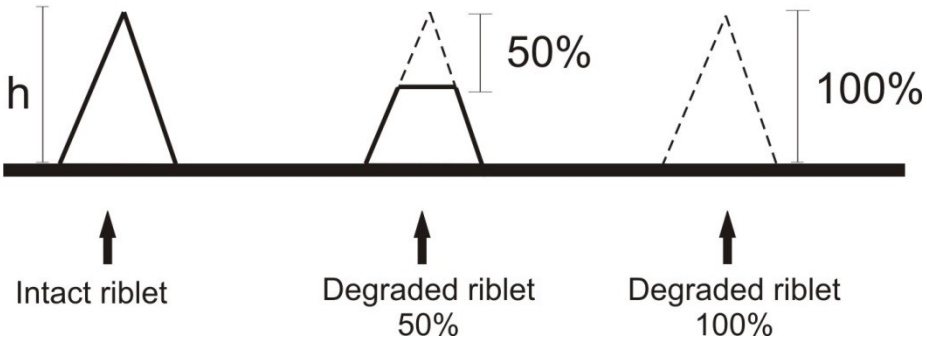


Figure 30 - Sketch of the intact riblet structure in comparison to degraded riblet structures (50% degraded and 100% degraded)

In the current work, a totally flat surface is analyzed in strict calculations on the central detector, and the main parameters are given as:

<b>Central Detector width</b>	28672 $\mu\text{m}$
<b>Distance from sample to central detector</b>	variable according to evaluations, from 3cm to 50cm
<b>Laser Wavelength</b>	variable according to evaluations, from 400nm to 750nm
<b>Sample width</b>	1005 $\mu\text{m}$
<b>Laser spot</b>	1000 $\mu\text{m}$

Table 6 Analysis parameters - Central detector distance and laser wavelenght variations

To previous analysis, taking an intact sample, in this case, could have 10 riblets on the surface, considering distance between riblets bottom center (dR) as 96 $\mu\text{m}$ .

However, considering a total degradation of the sample, with only 1 reflection on the surface ( $n = 1$ ) directly to the central detector, the reflection width on the detector can be calculated as  $1000\mu\text{m}$ .

The calculations performed in this dissertation result in a spatial step in order of  $7\mu\text{m}$ , which means the calculations are performed for equidistant positions on detector. The detector used as base to calculations presents a resolution of 2048 pixels, with 28672 nm width, corresponding to each pixel approximately  $14\mu\text{m}$  width. Thus, the calculations performed in this work, are defined to get a double precision of the real detector defined in previous works.

**Chapter 5 - Concept of a methodology to identify micro-structured surfaces**

The proposed methodology to identify status of micro-structured surfaces, define as main variables the reflection intensity of a light emitted by a laser source and related position of this reflection acquired by detectors positioned in pre-determined positions, in order to comprehend the entire reflected area of the laser light.

The calculated and acquired data can be compared as showed their integration explained on Figure 31

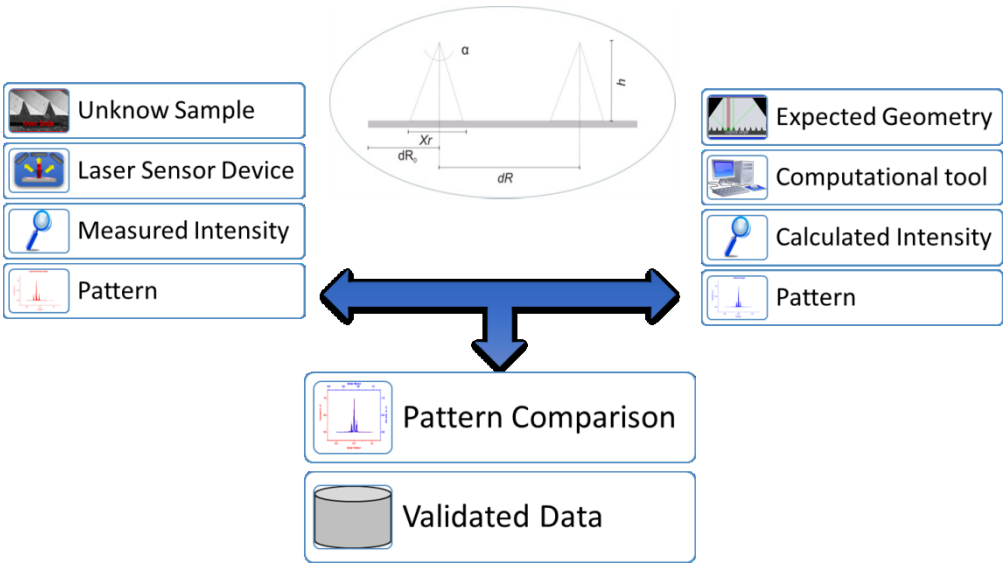


Figure 31- Validation of the Computational Tool Calculations

1<sup>st</sup> step of the methodology is the validation of the Computational tool calculations; this task is possible when the proposed task sequence is followed:

- Define the riblet geometry to be validated
- Acquire experimental data via laser sensor device
- Import experimental data of the same intensity as acquired by the detectors
- Identify the acquired pattern

In other hand,

- Set the expected riblet geometry on the computational tool
- Perform the calculations

- Check the generated calculated pattern

With reflection data saved on database, the computational tool will be able to perform the pattern comparison and saving the validated data to be used as a base of further evaluations.

With a considerable database of validated patterns, the proposed methodology is able to follow the next proposed steps; the 2nd step is described on Figure 32 which describes the operation of the proposed technique using a computational tool in Production Line of aerospace industries.

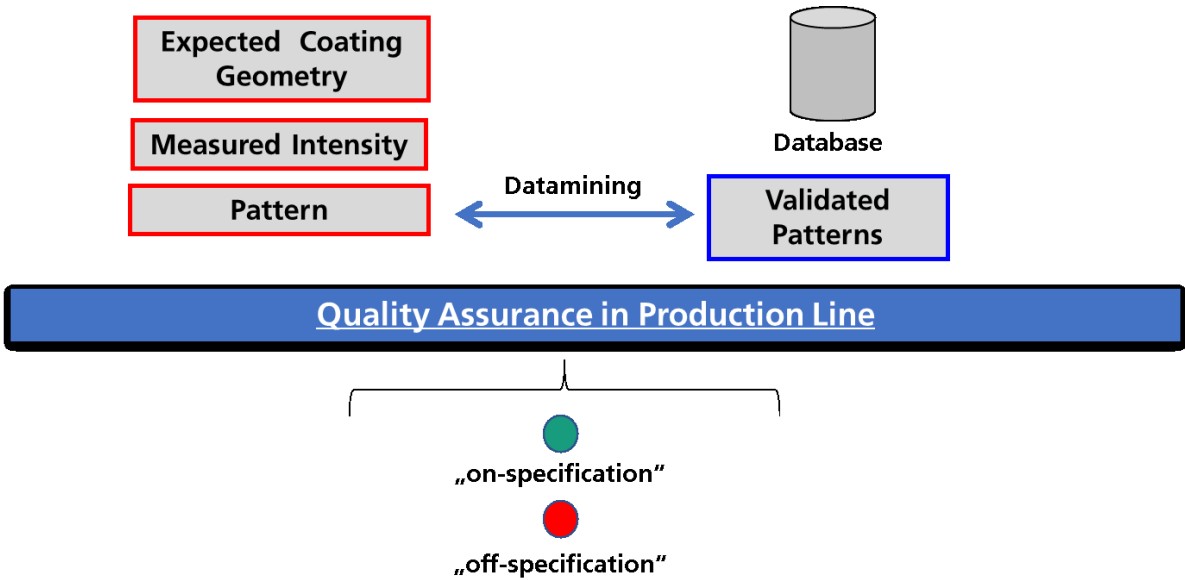


Figure 32 - Operation of the Computational tool on quality assurance field in Production Line

In production line of aerospace industries, the quality assurance of the process is a guarantee of the expected results in relation to the performance, costs and safety. The correct coating geometry is the key, as previously cited, to save fuel and increase the speed of the airplanes. In this proposed technique, a software with the expected geometry is set and after the measurement of the riblet area, in production line, datamining techniques can be used, as cited by [72–74], in order to compare and identify the main patterns, as it will be described on chapter 6 to assure that applied micro-structured coating is “on-specification”, according to quality threshold defined by the process.



Next proposed application is on the quality assurance of micro-structured coatings in maintenance line of aerospace industries. As described on Figure 33.

In this case, we also have expected riblet geometry, but, due to ageing or erosion, caused, for instance, by sand or ice, the sample status is unknown. Following the same proposed methodology, a laser sensor device will measure the sample and, the acquired intensity will be saved in a database provided by a computational tool. The expected geometry for this sample will be compared with the acquired pattern and, using data mining techniques, beyond the acceptable threshold percentage of the degradation on the micro-structured coating, with computational resources it is possible to identify, the percentage of the degradation and a range of possible degradation types, supporting on decision-making of strategical application of the product.

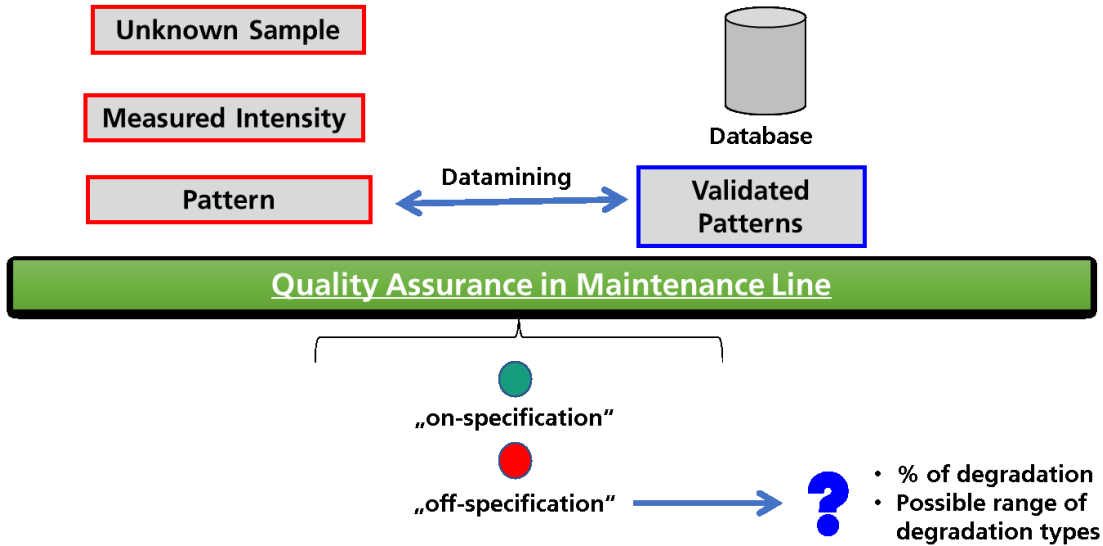


Figure 33 - Operation of the Computational tool on quality assurance field in Maintenance Line

A range of applications can be optimized by applying the suggested methodology, depending on the expected goal of the decision makers in industry or in academy. The possibility of micro-structured surface status identification supported by a computational tool, together with a laser sensor device, need an analysis criteria definition, in order to provide for engineers,

decision makers and software developers, guidelines that feedback reliable information about the evaluated surface and its updated status, as a new product in a production line or providing a reliable database to investigation on quality assurance field in maintenance line.

### Chapter 6 – Description of the Computational tool development and application

In order to evaluate the proposed technique, a computational tool was developed to fulfill the required parameters to feedback reliable data to making decision in production or in maintenance lines of aerospace industries.

This computational tool, responsible by configuration and processing of the proposed technique, is based on studies performed by Imlau et al [8], as previously cited and was developed on the Programming Language Java [75], with Java Standard Edition technology [76], using the development environment Netbeans [77], and to build software interface the framework JavaFX [75] was used.

To further applications, as it will be described on chapter "Conclusions and outlook", it is necessary a reliable and consistent database project. Implementation of the database system, to support all necessary requirements of data integrity, relationship and performance, developed by using a methodology based on structured data design and implemented in a Database Management System SQL-Server Express [78].

Database project, specifically designed to this project is shown on Figure 34 and allows this project to support several riblet definitions based on riblet geometries developed on Fraunhofer IFAM Institute and based on [3].

Explaining, the database model was designed to support several projects, with diverse parameters configurations. Each project, saved on "Sample" table can be related to several surfaces (Table "Surface"), with diverse degradation types and degradation levels, measured on percentage.

Each surface can be analyzed by varying several parameters, saved on table "Portion", according to desired analysis, these parameters are:

- Angle of the lateral sensors
- Start position on the surface (in  $\mu\text{m}$ , in relation to position 0)
- Number of the laser beams to reach the surface (each beam is equivalent to  $1\mu\text{m}$ )
- Interval distance between each laser beam (in  $\mu\text{m}$ ).

- Laser Wavelength (in nm).
- Distance from the sample to Central Detector (in cm).
- Distance from the sample to Lateral Detectors (in cm).

Entity – Relationship Model

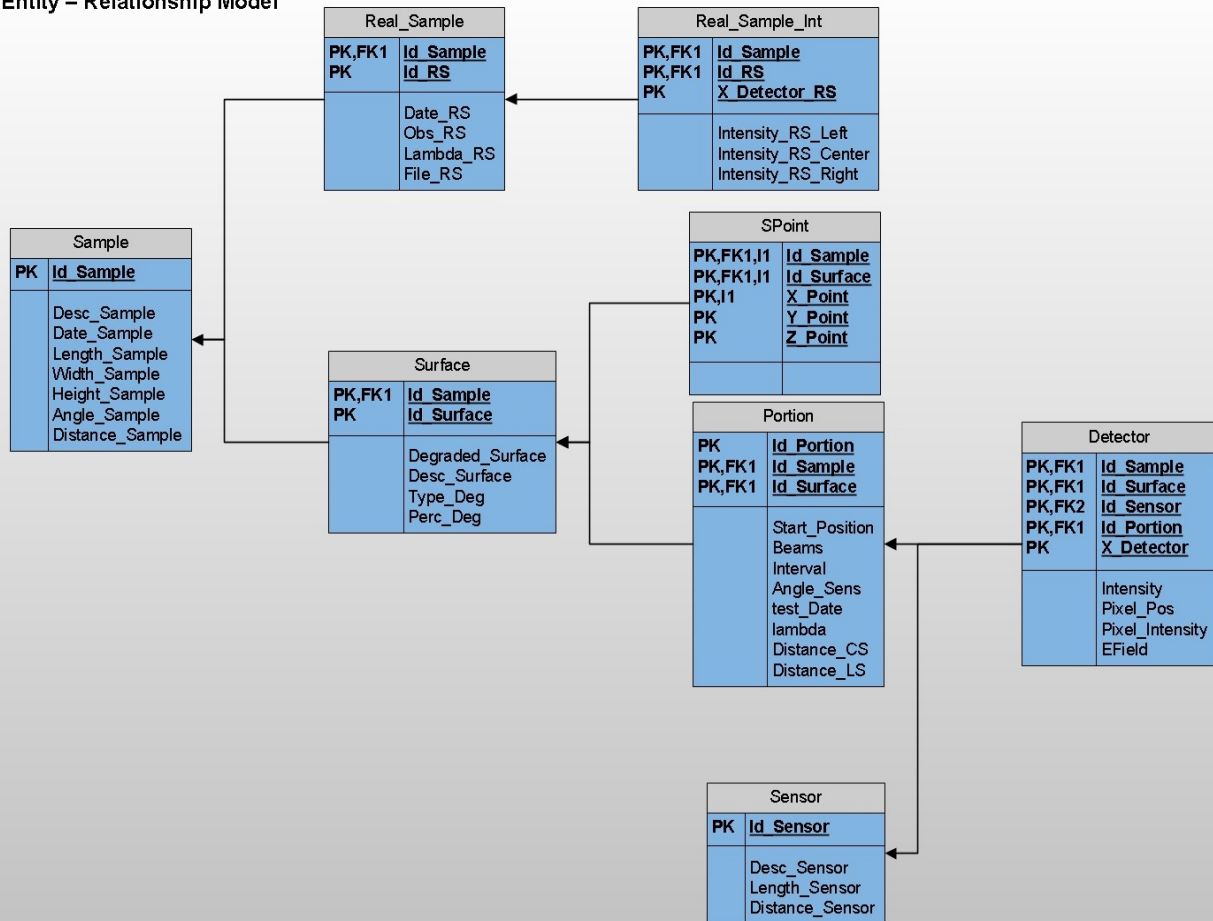


Figure 34 - Entity-relationship Model

The application of the database normalization is saved on table “Sensor”, the description of each detector to documentation, and the length of the detector (in  $\mu\text{m}$ ). Table sensor can be related to several records on table “Portion” and vice-versa, this way, it is necessary to create a table to link this relationship.

The table responsible to save all calculated outputs of the system is called “Detector”; data concerning the position on the detector (“X\_Detector” field, in  $\mu\text{m}$ ) and referenced calculated intensity (“intensity” field), are the main target of the calculations, enabling the computational

tool to provide optimal expected results in order to compare with the measured intensity performed via laser sensor.

Data acquired via laser sensor device, especially the laser setup used in this dissertation, are saved in 2 tables. In table “Real\_Sample” there is a relation with table “Sample”, and store data related to date of the measurement, the name of the imported file and the laser wavelength used.

To save the acquired intensity by the laser sensor device, all specific data are saved on table “Real\_Sample\_Int”, with the measured position on detector (in  $\mu\text{m}$ ) and related intensity on right detector, central detector and left detector.

Relevancy of the reliable data model is the key to perform further evaluations and data mining process. The main goal of the developed database application is to provide a consistent knowledge database to which it can be a support to further evaluation results, to be discussed in the next chapter.

Chapter 7 - Results Evaluation

Figure 35 shows a flow-chart representation of the step by step procedure of investigations of evaluation tasks and definition of analysis criteria performed in this work.

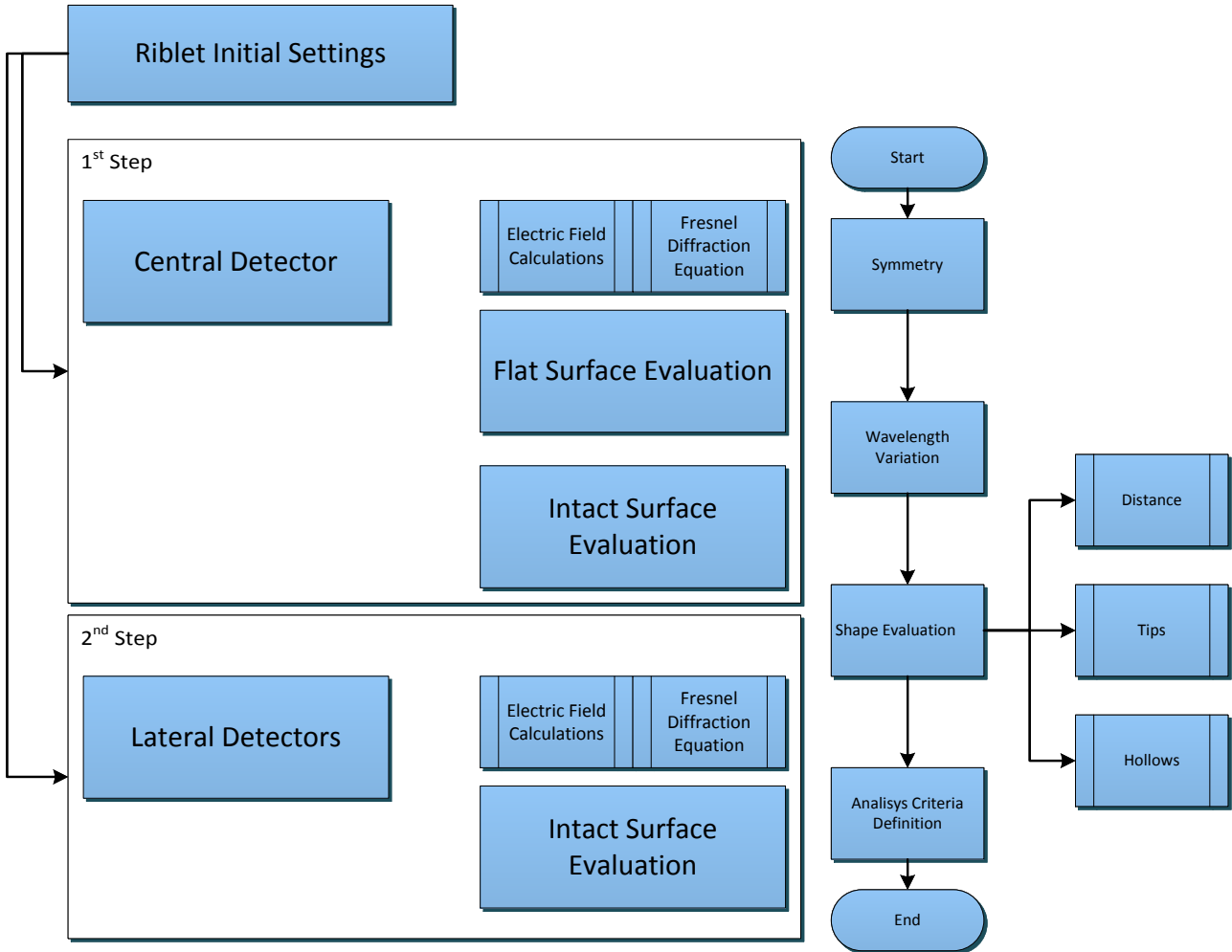


Figure 35 - Analysis evaluation process flow chart

Initial results applying the calculations presented in this dissertation show a good agreement with the theoretical approach. At first, a completely degraded sample, considering the completely flat surface was evaluated and performed calculations that expected characteristics of the laser light reflection, as symmetry and periodicity of the wave were reached. In Figure 38 normalized calculations using equation 84 (Figure 36) and equation 85 (Figure 37) are shown.

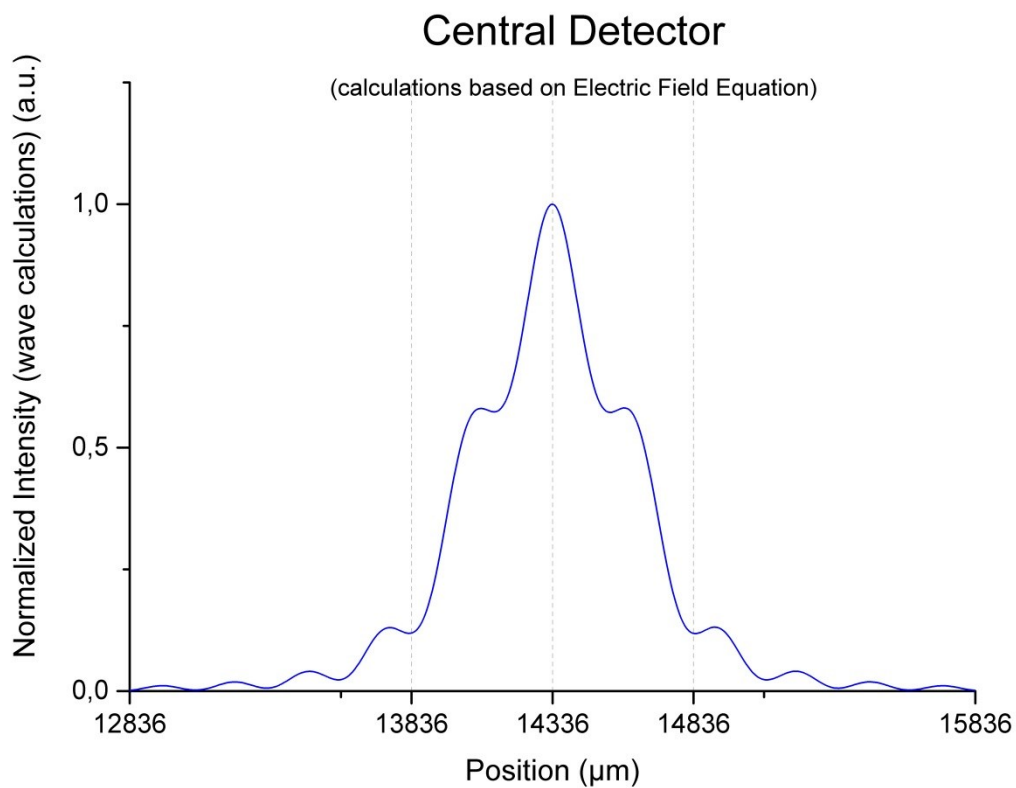


Figure 36 - Intensity plot calculated – Electric Field equation

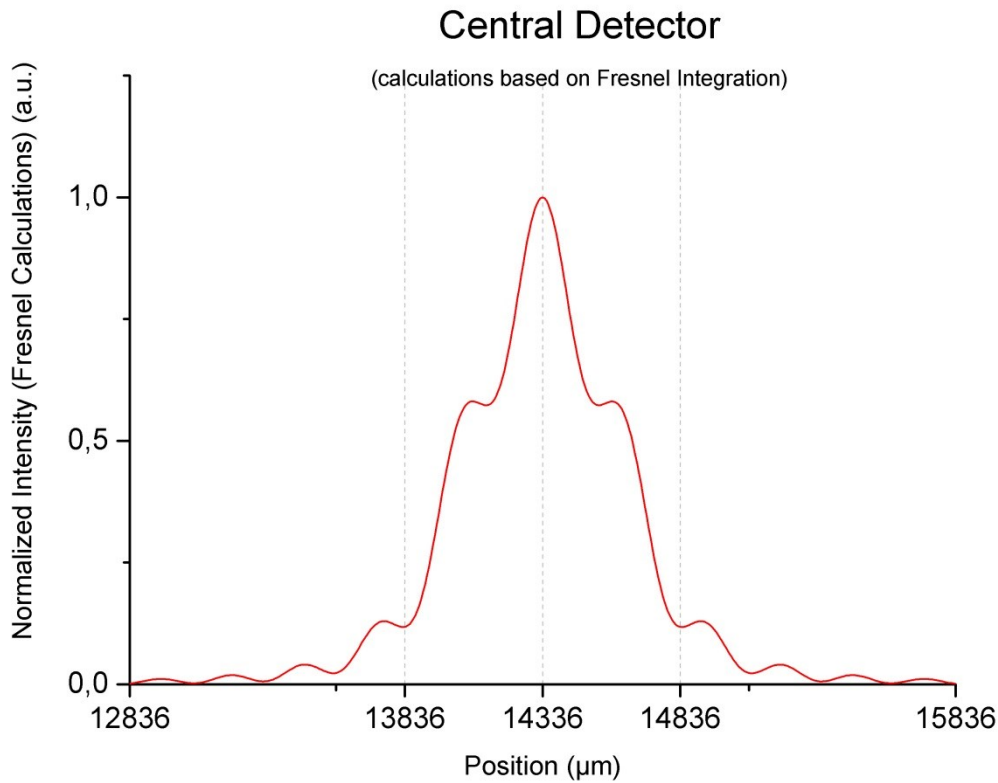


Figure 37 - Intensity plot calculated – Fresnel Integration

Comparing Figure 36 and Figure 37, the similarity of results performed by both different calculations can be identified. Evaluating the symmetry of both, the findings shown in Figure 38 present a great accuracy comparing the intensity calculated in relation to detector center, in this evaluation the difference between the both sides in relation to center of central detector are calculated, and if it tends to zero, that means there's no difference, then a good symmetry is reached. Figure 38 shows the comparison between the symmetry calculations in relation to calculated intensity, finding expected symmetry level, with variations due the precision used. Even with high calculated intensity, specially observed around detector center, calculated symmetry tends to zero, as expected.



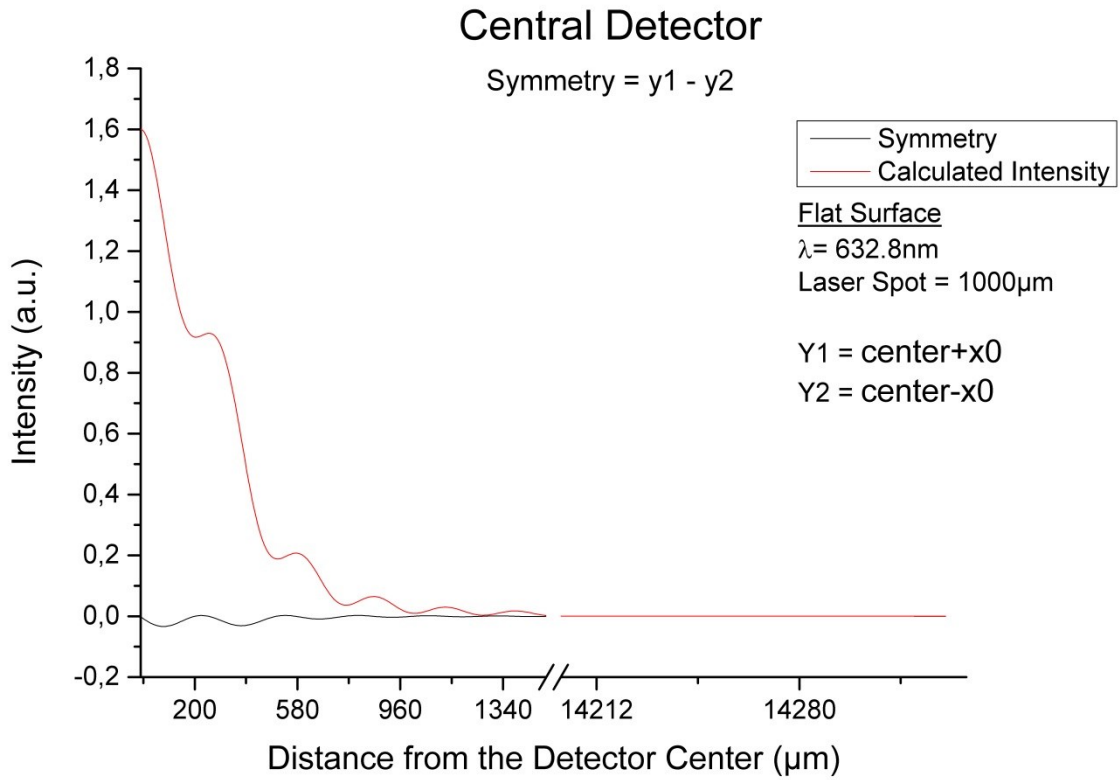


Figure 38 - Symmetry evaluation

An analysis of the plots presented in Figure 36 and Figure 37, concerning the periodicity of the calculations, is presented on Figure 39, where expected calculations are shown in a logarithmic scale.

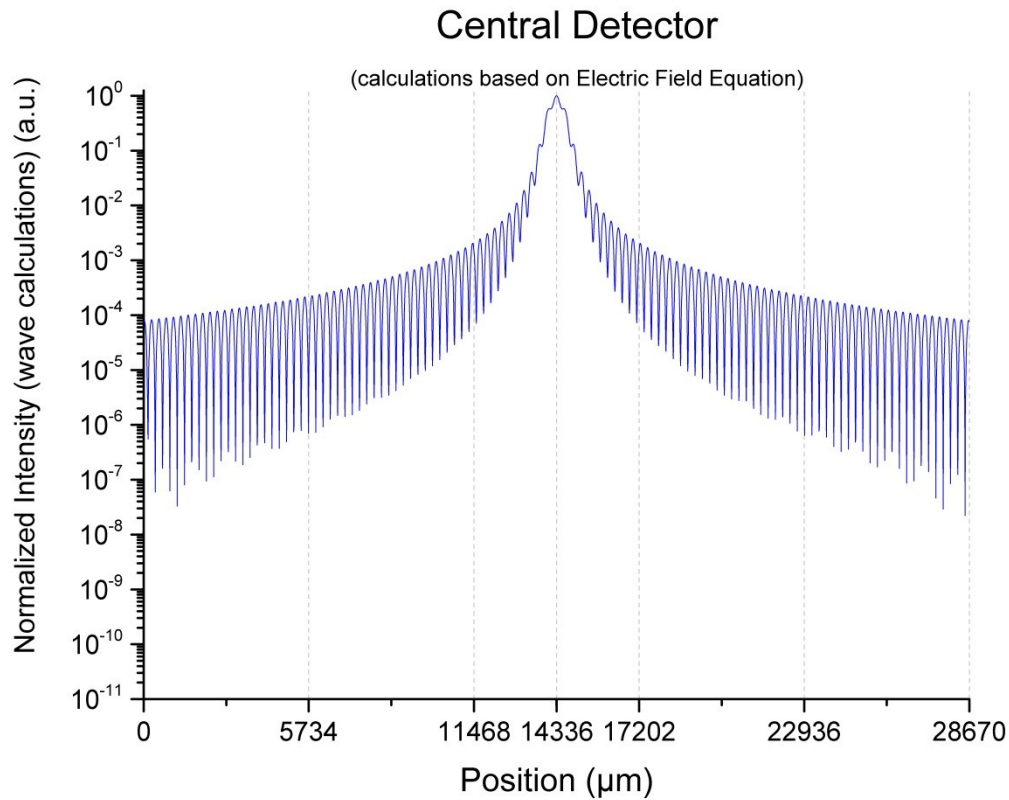


Figure 39 - Periodicity evaluation

The next result of the calculations considering a totally degraded flat riblet surface, performed based on equation 84 (Figure 40) and equation 85 (Figure 41) show a result which could be an expected result according to literature. Following Born [69], meaning varying the distance from the sample surface to the analyzing detector, the change from Fresnel pattern to Fraunhofer pattern can be identified and the proposed calculations are validated, observing the change of the shape if the distance increases, corroborating theoretical foundation, and, in this particular case, observed on calculations performed to distances in 3cm (Fresnel Pattern), 50cm (Fraunhofer Pattern), and an intermediary calculation on 28.7cm, where is observed the changing.

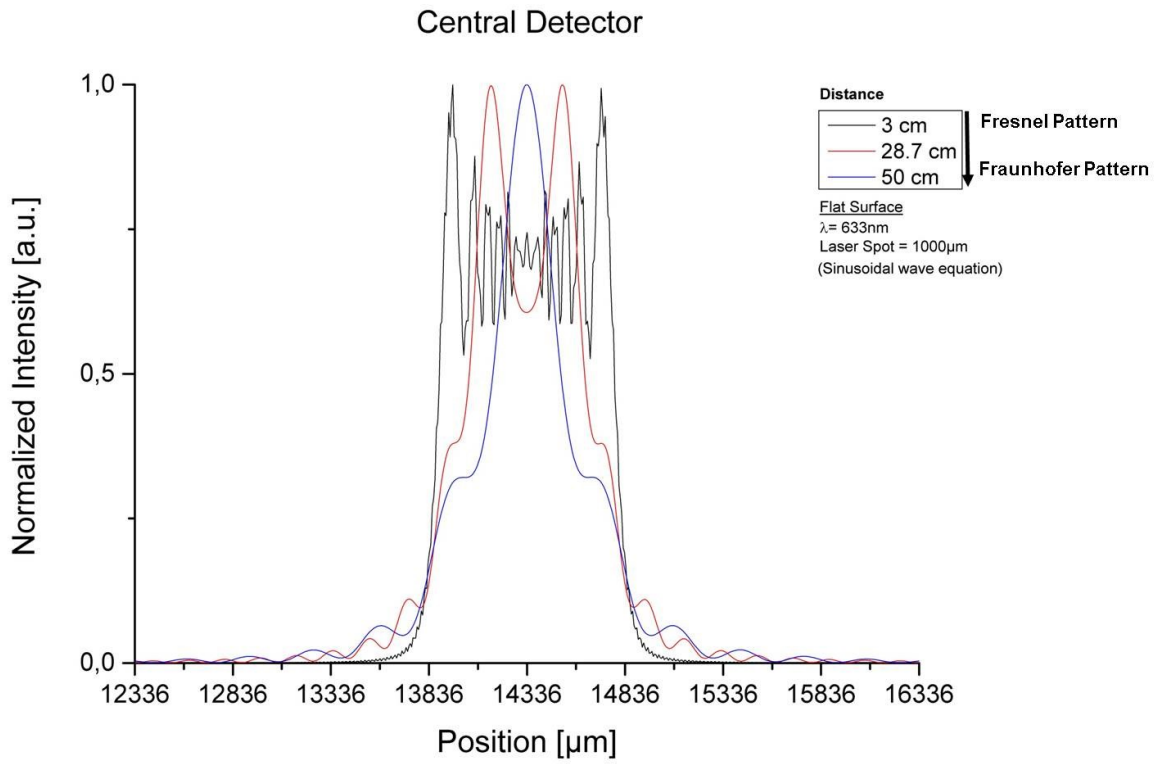


Figure 40 - Distance variation based on wave equation

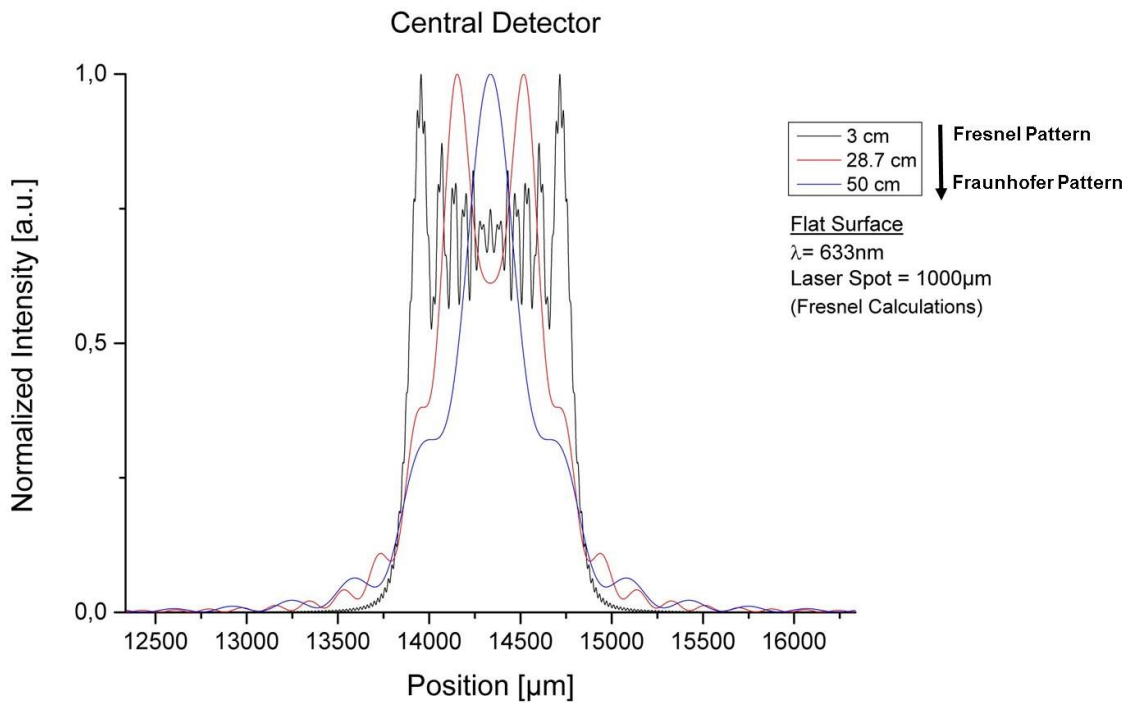


Figure 41 - Distance variation based on Fresnel integration

Evaluation of intact riblet structures, observing only the results performed on the central detector can provide information about the number of the riblets and the distance between riblet bottom centers ( $dR$ ). Both data can be easily identified on the Fresnel pattern, as compared in Figure 42 and Figure 43, where it is possible to identify 9 riblet structures (Figure 42) and 19 riblet structures (Figure 43). The distance between the lower intensities on the hollows (minima), are related to the distance between the riblets, making the evaluation possible if the performed calculation is in accordance with the input parameter related to the distance between riblet bottom centers ( $dR$ ). Identification of the number of hollows was performed in a first step identifying the number of peaks inside the laser spot area with the software Origin 9.1, using the gadget Quick Peak; the gaps between the peaks identified are considered hollows.

As observed in Figure 44, it is possible to identify the Fraunhofer pattern, and the area between the central maxima and the first maxima, it is possible to observe the number of riblets on the structure. The number of hollows, between central maxima and 1st maxima, on both sides, represent the number of riblets, in the evaluated case, 9 riblets and as shown on Figure 44, these 9 riblets are related to 9 hollows.

Inside the visible light spectrum, between 400nm and 750nm wavelength it is possible to observe, considering Fresnel pattern with the distance from the riblet surface until the central detector equals to 3 cm, no variation on the distance between the peaks. Allowing analysis concerning the distance between riblets bottom centers based on the calculations, as shown on Figure 45.

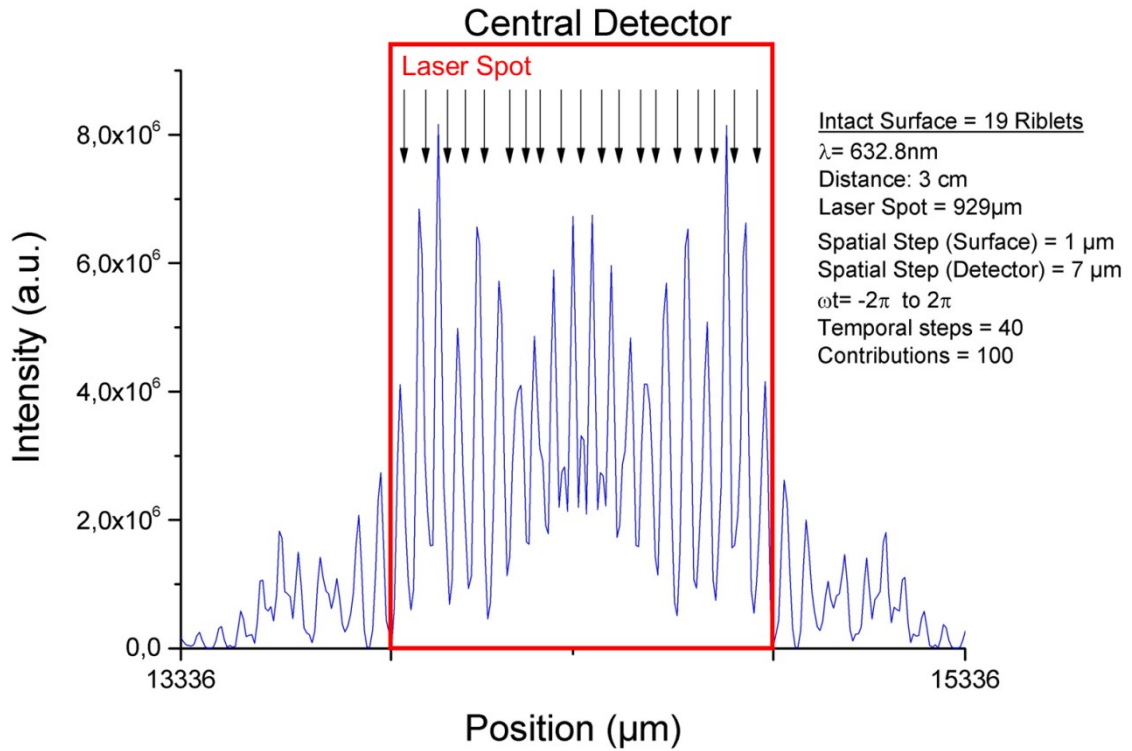


Figure 42 - Detail – Central Detector – Intact Riblet Sample – 19 riblets – Fresnel Pattern

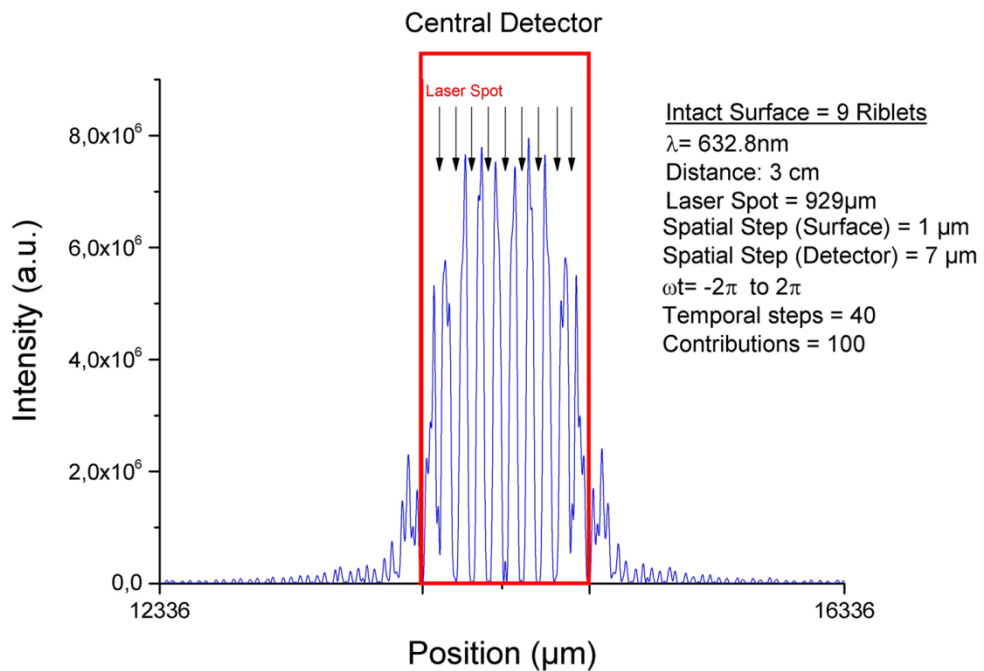


Figure 43 - Detail – Central Detector – Intact Riblet Sample – 9 riblets – Fresnel Pattern

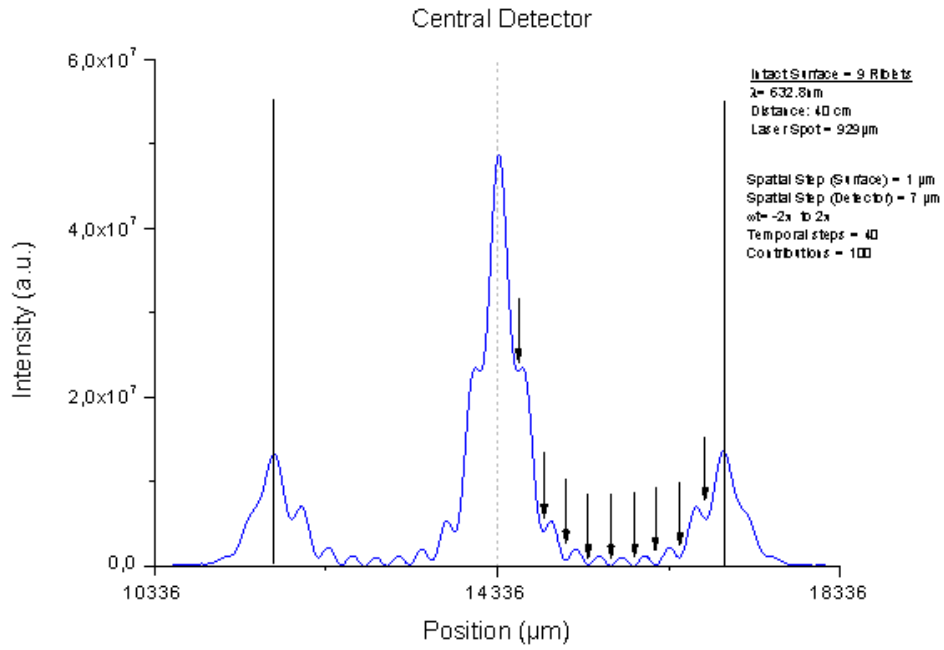


Figure 44 - Detail – Central Detector – Intact Riblet Sample – 9 riblets – Fraunhofer Pattern

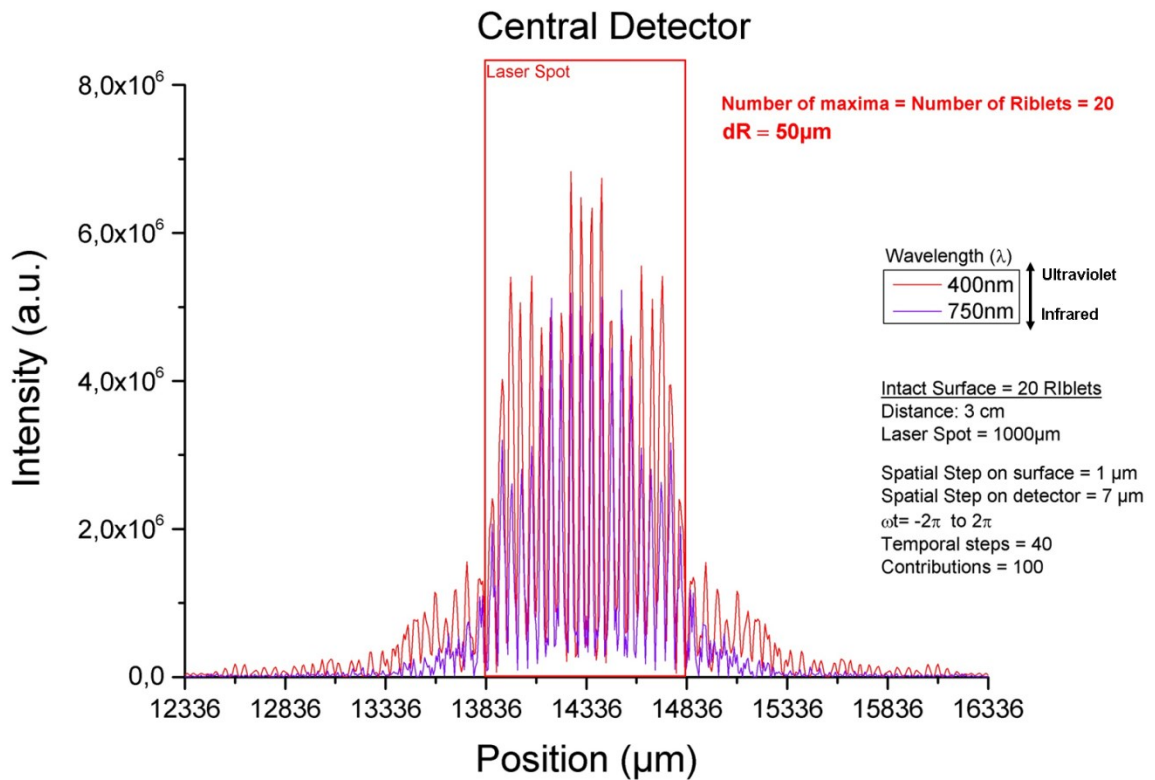


Figure 45 - Detail – Central Detector – Intact Riblet Sample – 20 riblets – Wavelength Comparison

The number of the hollows observed between the central maxima and the 1st maxima on both sides on the experimental measurement is the same as observed on the calculated intensity plot and it is equal to 20, reproducing the statement that the number of hollows (minima) can be used to identify the number of riblets on the structure. There's a difference observed between both plots specially in relation to the positioning of the central maxima, due the possibility, using the computational tool, to precisely define the position of the laser spot, and experimentally the adjustment of the laser and the sample are not easy.

A point to be observed is in relation to the resolution of the detectors, in this experimental evaluation, the detector resolution is 2048 pixels in a detector area width equals to 28672 $\mu\text{m}$ , in comparison to the calculated intensity by the computational tool, in order of a spatial step defined to 7 $\mu\text{m}$ , doubling precision is equivalent.

The measurements show that the wavelength and divergence depend on the distance from the first order to the main maximum of the order 0, and the structure of the surface is comparable to an optical grating. If the laser beam falls perpendicular to the surface, the reflected beams interfere with the base surface of the sample, applying the Bragg condition,  $d$  can be calculated as:

$$d_n = n \cdot \lambda = g \cdot \sin(\theta_n).$$

In this case, the lattice constant corresponds to the spacing of the periodic arrangement of the riblet structures ( $g = 100 \mu\text{m}$ ). Calculating the divergences and the respective wavelength, the theoretical distance from the 0 to the 1st major maxima can be determined and compared with the calculated ones by computational tool. The values for this result from the evaluation of the graph of the  $0^\circ$  reflex, is shown in Figure 45 and presented results show agreement between the theoretical calculations and performed calculations made via proposed computational tool. On the range of the wavelength of the visible spectrum it is possible identify a good assessment, not so accented if the wavelength tends to be out of the visible spectrum, although it still presents values within the margin of error consistent with the application.

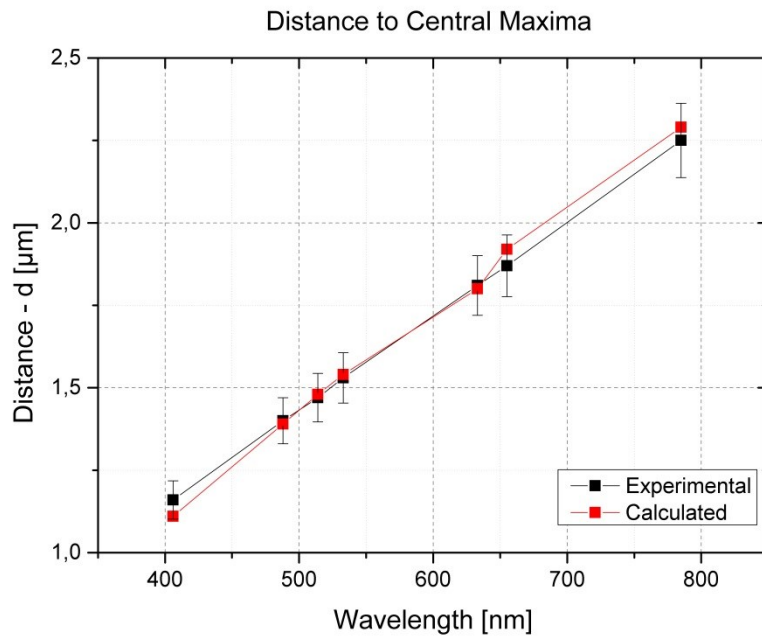


Figure 46 - Measured distance comparison of different wavelength lasers calculated and theoretical values.

In agreement with the experimental measurements performed by the laser sensor device, Figure 46 shows the comparison regarding calculated intensity by the computational tool and the experimental measurements, where it is possible to observe the supra cited parameters to be evaluated.

To perform this evaluation, the proposed model is:

<b><i>Central Detector width = 28672 µm</i></b>
<b><i>Distance from sample to central detector = 40cm</i></b>
<b><i>Laser Wavelength = 632,8nm</i></b>
<b><i>Sample width = 1000µm</i></b>
<b><i>Laser spot = 1000µm.</i></b>
<b><i>Number of riblets = 20 riblets</i></b>
<b><i>Distance between riblets bottom centers = 50µm</i></b>

Table 7 - Applied parameters for the evaluation model

In assessment with real measurements performed via laser sensor device, developed at Fraunhofer – IFAM, applying normalization from 0 to 1, and adjusting the maxima intensity



## Chapter 7 – Results Evaluation

point, performed calculations show in relation to previous described evaluations that calculated intensity via developed computational tool could reproduce the intensity experimentally acquired by the laser sensor device. Parameters of evaluation, as symmetry and number of calculated maxima, in this case performed via software Origin, using the gadget quick peaks, show equal number of maxima as shown on Figure 47.

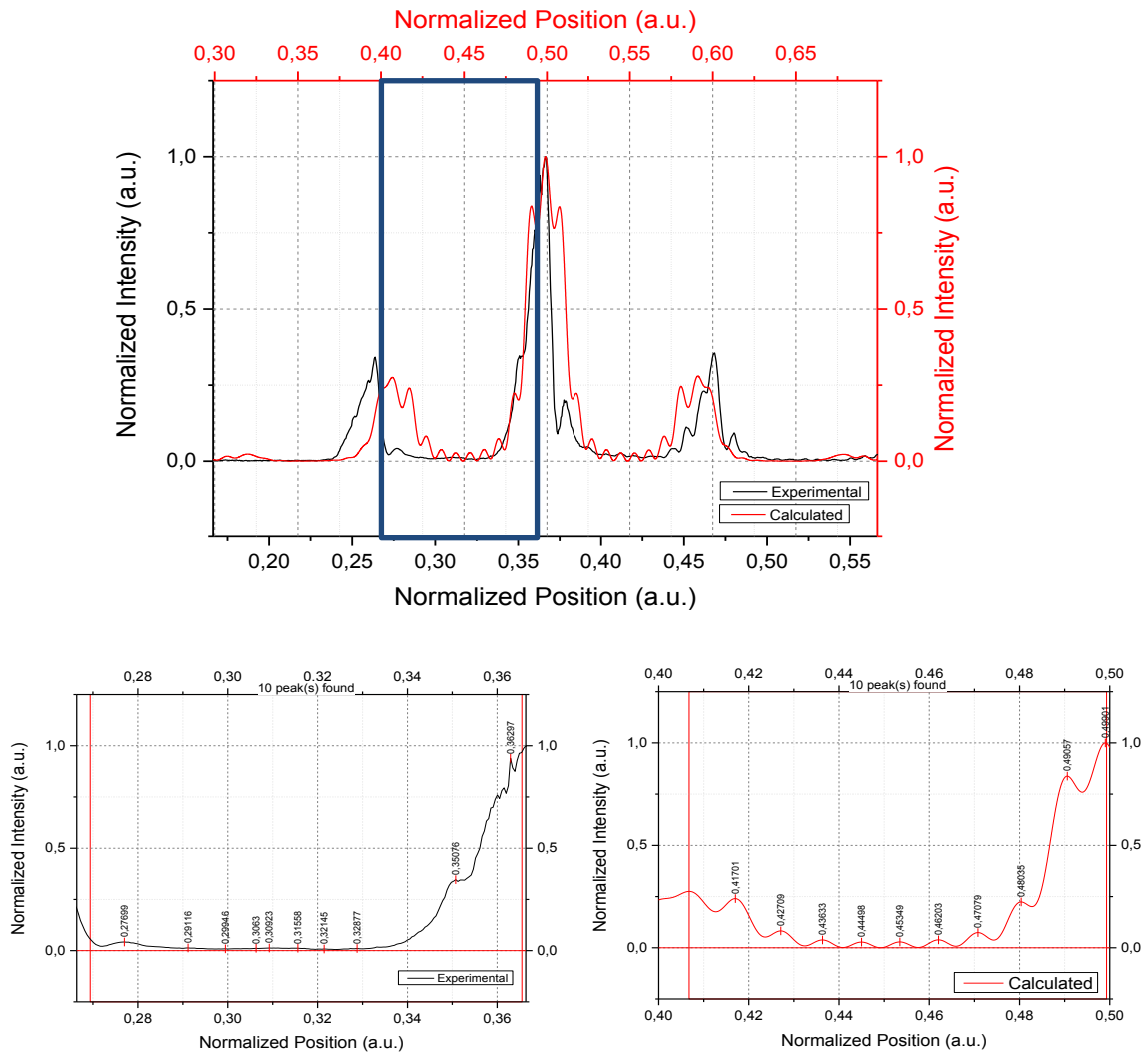


Figure 47 - Comparison between experimental measured intensity performed via laser sensor device and calculated intensity performed via computational tool with detailed graphic in evaluated region between the central maxima and 1st maxima.

Taking into account observed differences among the normalized position, is assumed that in the experimental results it is not possible determine the exactly position where the laser spot will start. The presented evaluation can establish a relation between the experimental measurements, the calculated measurements and the number of the riblets on the measured surface, allowing the computational tool for further deep surface evaluations.

Following to 2<sup>nd</sup> evaluation step, this task consists in analysis of the calculated intensity performed on lateral detectors. Performing the same methodology applied to evaluate the calculations performed on the central detector, symmetry and periodicity are presented on the calculated results. Figure 49a shows the entire calculated intensity range on right detector. The values calculated are spaced from  $7\mu\text{m}$  and the variation of  $\omega t$  is defined with 40 temporal steps between  $-2\pi$  and  $+2\pi$ . It is possible to observe periodicity of the calculations, confirmed by Figure 49b, which shows the same calculations in log scale.

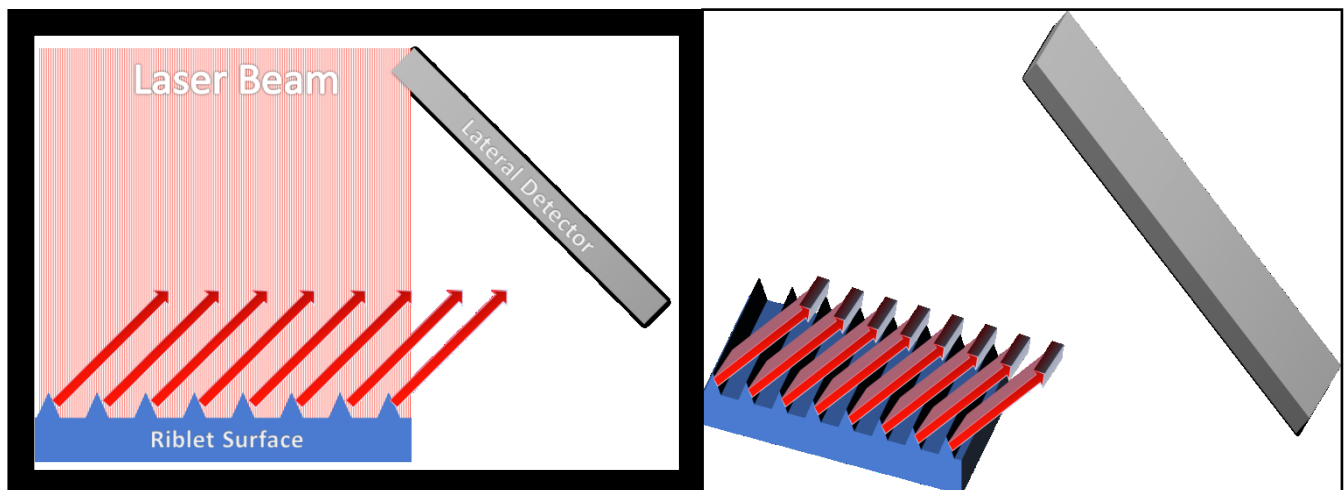


Figure 48 - Schematic representation of the laser reflection on riblet flanks to lateral detector

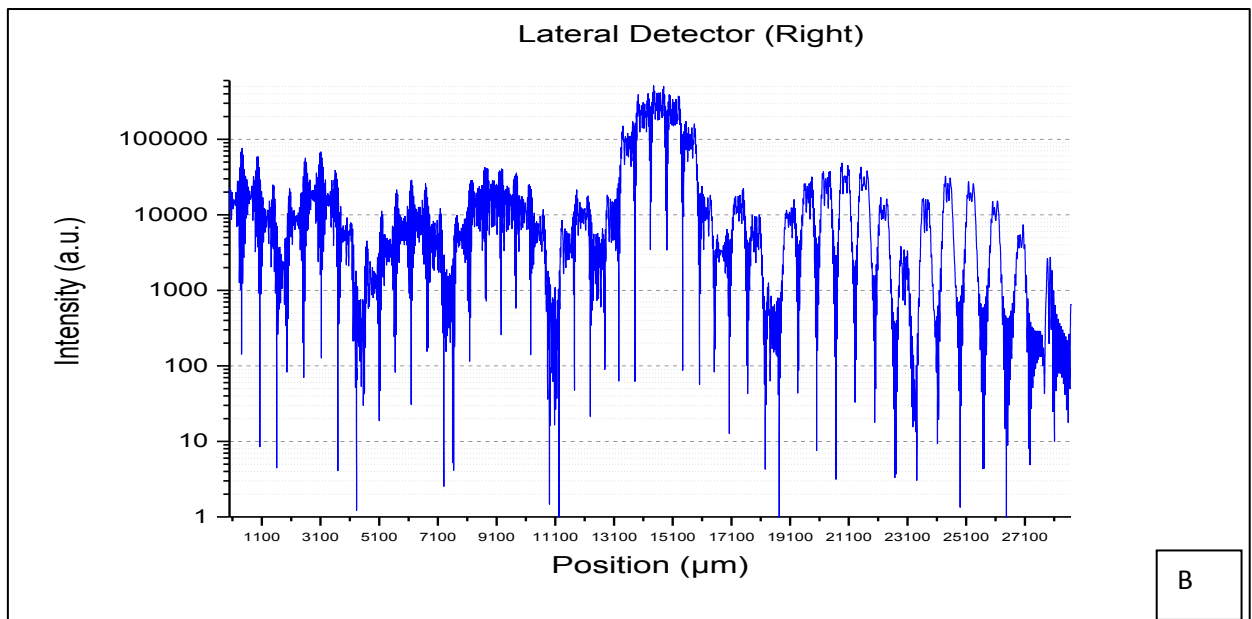
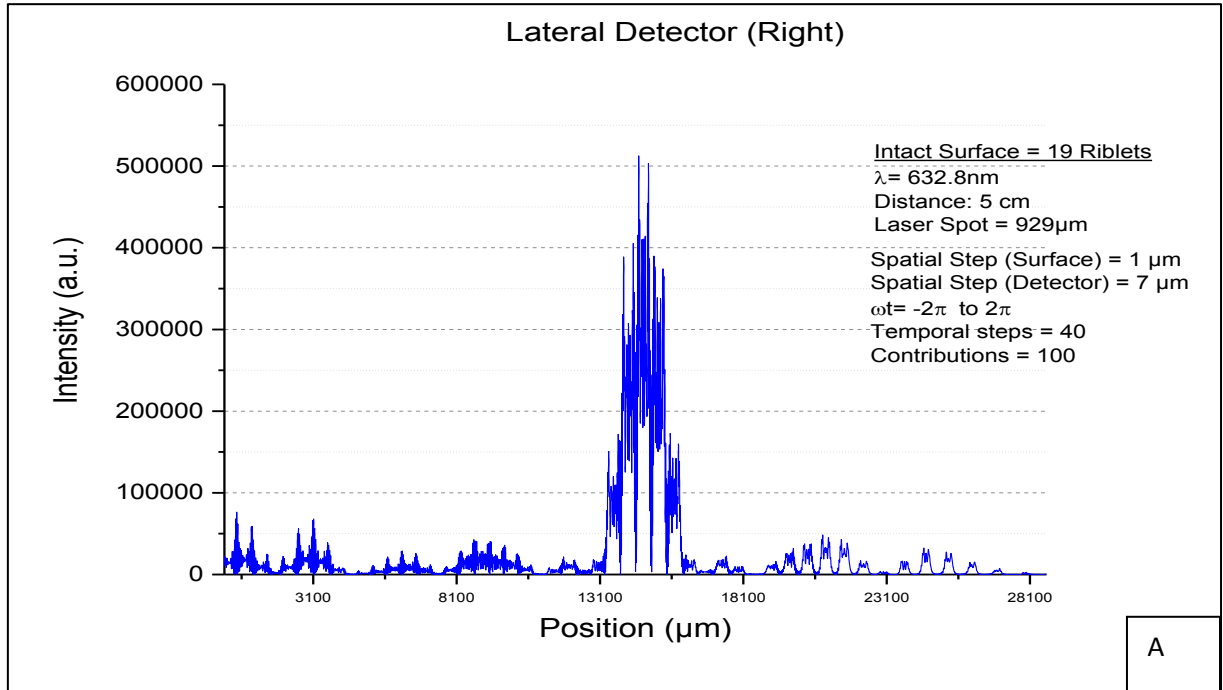


Figure 49 - Intensity plot calculation of lateral detector (right side), Absolute calculations (a) and periodicity evaluation of calculations in log scale(b).

## Chapter 7 – Results Evaluation

A complementation of this analysis is the evaluation related to the distance between the maxima observed on lateral detector calculations. By applying the Bragg condition to confirm the performed calculations it is possible to identify the expected results shown on Figure 50. As applied to evaluate the central detector intensities, on the lateral detector a spreading of the intensity related to the applied angle to the calculations is observed. The distance calculated, it is assumed that is on Fresnel pattern, there's a regular variation between each set of maxima, as shown on detailed plot on Figure 50, analyzing the highest set of maxima, with the direct incidence of the reflected laser light, the return of the expected variation of the peaks.

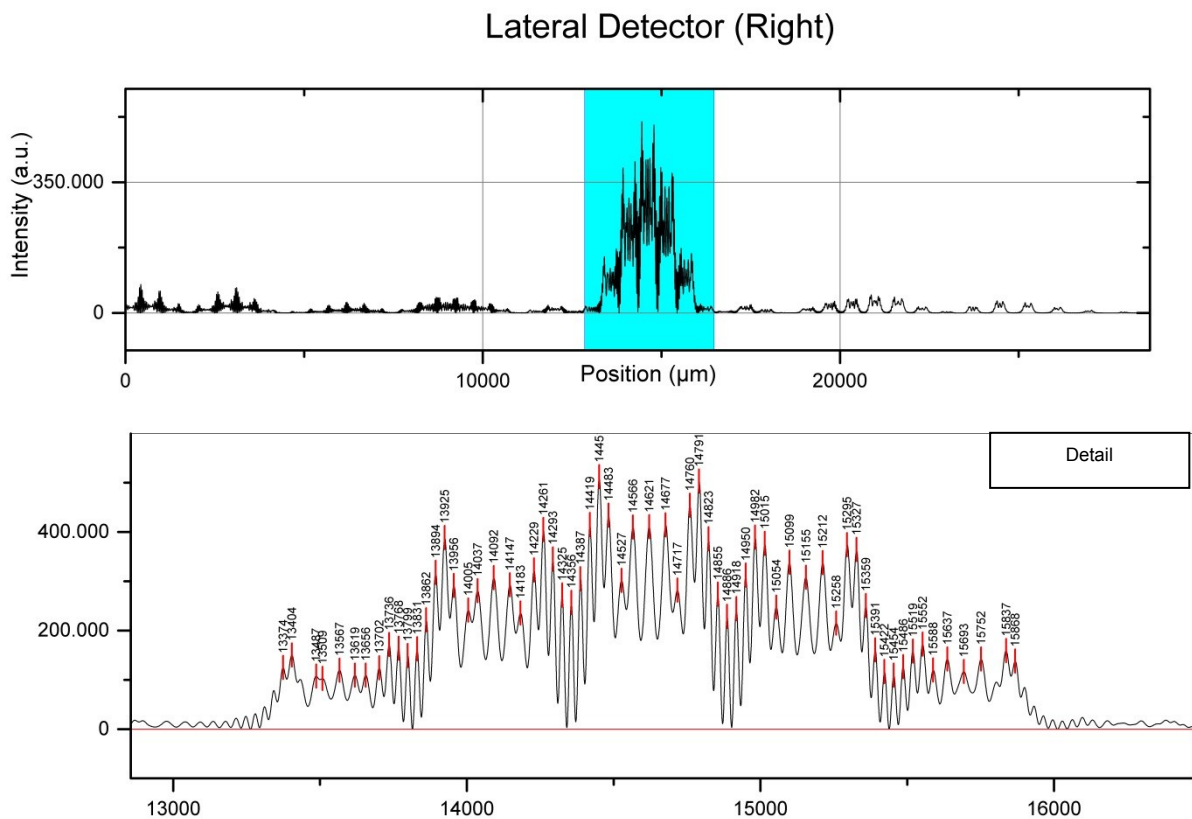


Figure 50 - Intensity plot calculation of lateral detector (right side), Expected variation of the peaks

Distancing from the highest peak, it is observed, as cited on chapter 2, related the Young experience, that the reproduction of the main diffraction behavior in direction to the borders.

## Chapter 7 – Results Evaluation

Expected periodicity in relation to the peak distance is shown on Figure 51 re-scaling calculated intensity on logarithmic scale. The observed periodicity inside the main spot of observation, is related to the calculations of each riblet flank., reproducing on the reflected calculated intensity, a regular split of the micro-sctstructure and presenting a good assessment to evaluate the main parameters of the riblet geometry, as height and angle, specially related to theoretical approach previously cited and illustrated by Figure 24

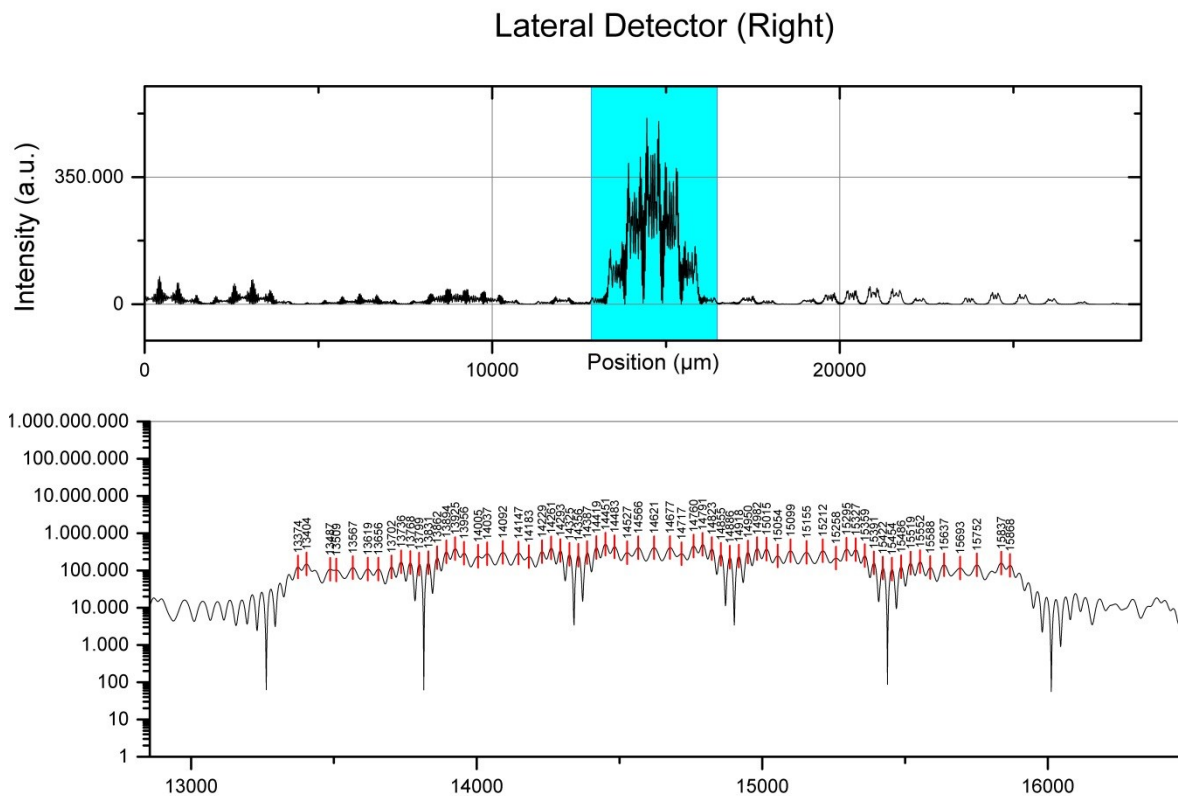


Figure 51 - Intensity plot calculation of lateral detector (right side) - Detail in Logarithmic scale

Using experimental data provide by a laser sensor device developed on Fraunhofer – IFAM, a comparison on acquired data in left detector of the sensor shows the same expected periodicity, normalizing from 0 to 1 and re-scaling to logarithmic scale, a comparison between the calculated intensity and acquired experimental data perform a symmetry and calculated periodicity, with variations attributed to environment interference, external luminosity incidence and difference on resolution of the used detector. (Figure 52)

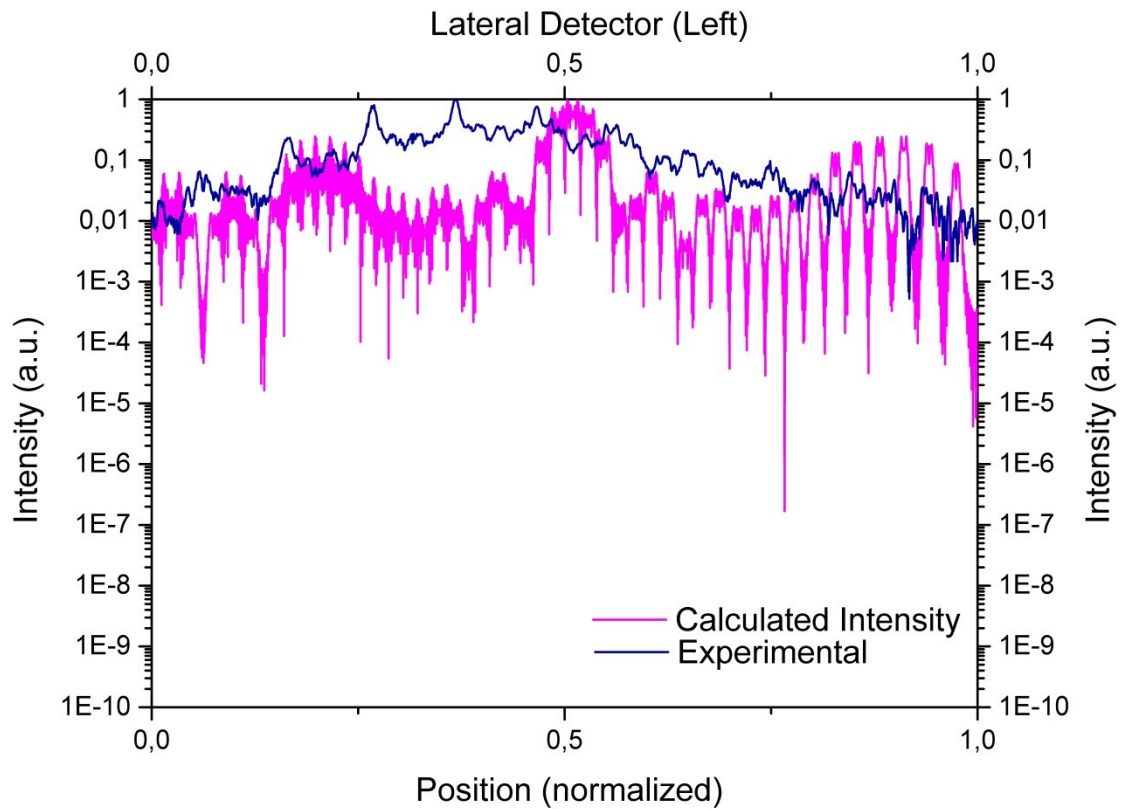


Figure 52 - Intensity plot calculation - Left detector. Comparison between calculated and experimental data in logarithmic scale.

Extrapolating the findings results based on state of the art, a simulation of an degraded structure was performed based on a regular flat degradation, where is considered a cut on the top of the riblets, as shown on Figure 53

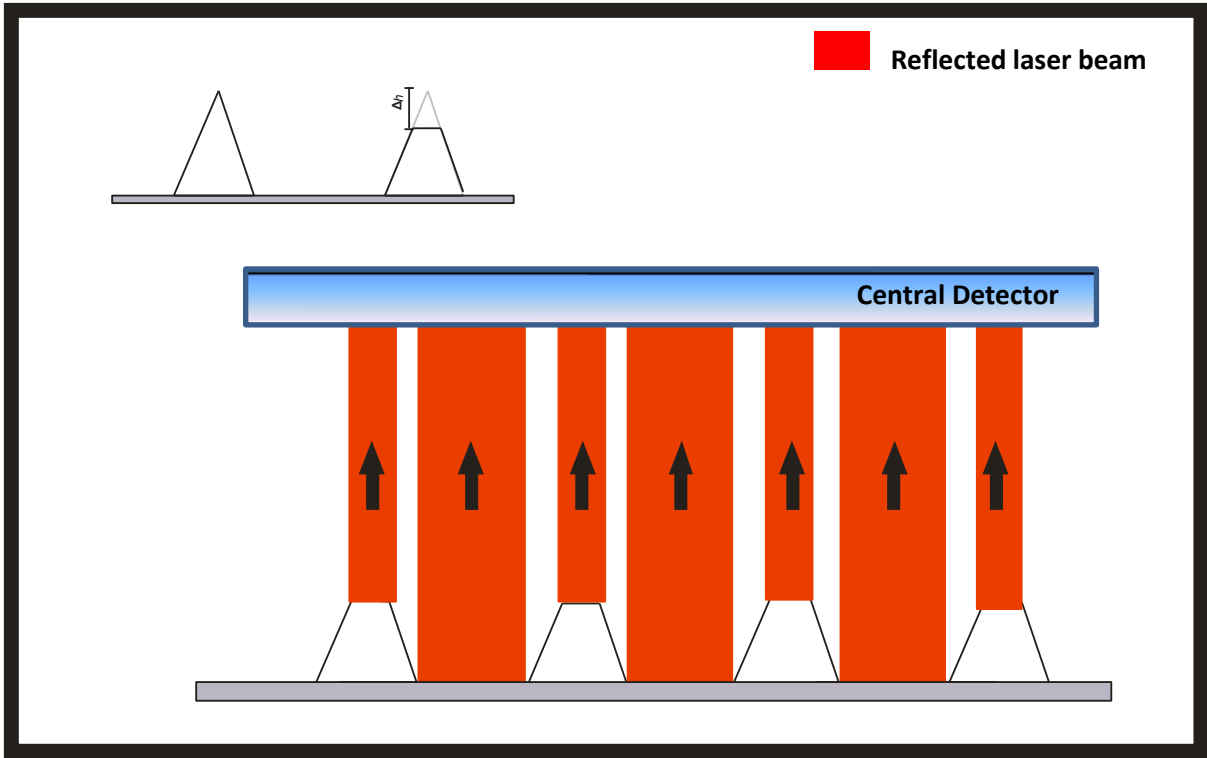


Figure 53 – Degraded riblet structure – laser reflection sketch on central detector

The calculated result via software is demonstrated on Figure 54. In this plot is demonstrated that is possible to identify the expected divergence related to the number of peaks found. In an expected intact surface for this geometry and analyzed spot, number of riblets = 4. The number of peaks is 7, related to the reflection of the base of the riblet structure and the degraded part of the riblets. Further analysis can be performed to keep a relation between the distance between the peaks and the riblets geometry.

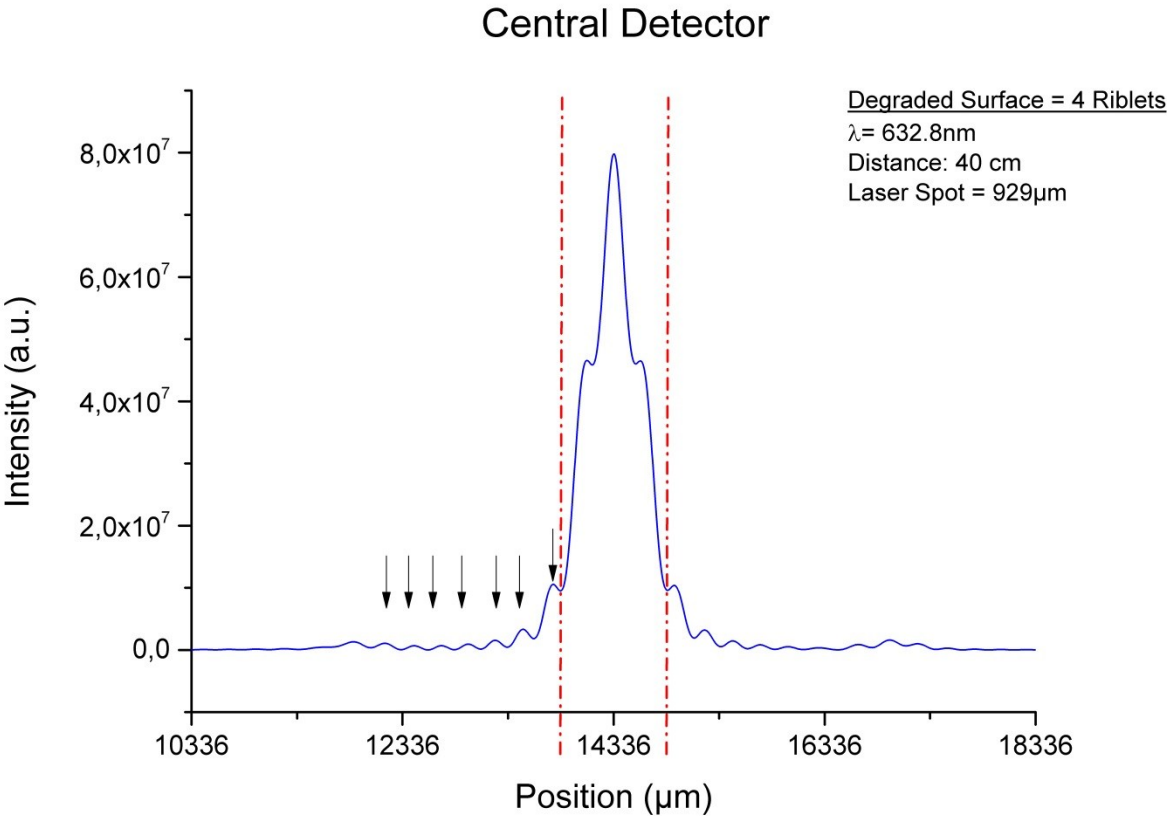


Figure 54 – Degraded riblet structure – Central detector plot evaluation



### Chapter 8 – Conclusions and Outlook

Analyzing presented results, this work intends, to trace guidelines which can be followed in industrial and scientific projects aiming the use of a computational tool along with pre-determined setups of laser sensor devices, to identify status of micro-structured coatings specially used on aerospace industry, and in this particular case, with the geometry based on riblet structure.

Focusing in a technical and objective solution to be applied on quality assurance field in production and maintenance line of industries, theoretical and experimental approaches were crossed and evaluated, opening a way to be explored and implemented with new technologies to rise and the presented results were made to be more than a basic and theoretical compilation of calculations and resultant plots.

Theoretical founding in optics and diffraction theories presented as a solution to perform reliable and fast way in a development of computational tool potentially conceived to be embedded in a portable laser sensor device. Applying this concept in real cases, could save time and resources in a decision process of quality assurance.

To relate presented results with the proposed objectives of this work, the initial specific objective was the graphical reproduction of a micro-structured surface based on pre-determined geometrical parameters. As proposed, using the methodology based on object oriented programming, and pre-determining the basic geometry of the micro-structure, in this particular case, based on riblet structure developed at Fraunhofer – IFAM, a successful graphical renderization was achieved. In two and three dimensions, the visualization is an important step, to understand the reflection of the laser light on the structure, degradation cases which possibly could occurs on the surface and to be a base of the intensity calculations.

A graphical renderization of the laser light incidence on the surface and respective reflection and hitting on the detectors, in this work, the laser sensor device considers the use of three detectors, one central detector, straight  $90^\circ$  in relation to the surface and two lateral

detectors, with an inclination of  $45^\circ$  and  $-45^\circ$  in relation to the surface. This step was accomplished and reproduces the entire laser sensor device setup.

In order to validate the theoretical findings, the calculations were implemented on a computational tool to reproduce the expected intensity acquired by the detectors and, based on this, to be a support to evaluate and describe the analysis criteria to be followed and improved on further prototypes and studies. The calculations, especially with the embasement of a powerful database management system, were implemented and validated, reproducing expected results.

The diffraction theory applied to perform the calculations, showed reliability and, applying the proposed integration on the calculations, good performance in terms of calculation time and precision were reached, also taking into account the integration of Object Oriented Programming (OOP) with a powerful Database Management System (DbMS).

The analysis of the calculated results allowed the discussion to identify on experimental results obtained by a prototype of a laser sensor device, the main criterias that can be explained as follows.

By evaluating the results obtained on the central detector of the laser sensor device, it is possible with this obtained results, with any configuration, specially taking in account a sensible parameter for the study, the distance from surface to the detector, identify:

- Number of riblets on the structure
- Distance between riblets

If the setup of the laser sensor device has the distance from the surface to the detector inside of the Fresnel pattern of diffraction, it is possible identify:

- Number of riblets on the structure
- Distance between riblets
- Width of the base of the riblet

If there's some degradation, in the resultant plot of this situation it is possible to identify in which riblet there's the defect and based on the degraded size; deduce the height of the degraded riblet.

Evaluating the data obtained by the lateral detectors, and following the same procedure of investigation and assumption of analysis, the resultant plot can return to analysis:

- The number of the riblets on the structure
- The height of each riblet on the spot and each flank.
- The type of degradation, if imply in rounded degradation.

The number of riblets is obtained by the same analysis in both cases, on the central detector and on the lateral detectors. The analysis of the plotes generated via any experimental setup can bring this information, setting the peaks on the plot, taking into account the laser spot and the pre-determined angle.

For each side of the riblet, the analysis will be performed by an specific detector. The height will be identified; in this case, it is important to set the distance from the surface to the detector, inside the Fresnel pattern of diffraction to get more precise data.

Comparison between an intact riblet structure and a degraded structure, considering a flat degradation allows the proposed methodology to identify the diference between the expected values if the structure is intact ad the real measured values after the degradation process. Comparing the height of each riblet structure, the higher height is related to the intact riblet and the smaller one is related to a degraded riblet.

The spread of the intensity on the lateral detectors, determines the type of degradation. The same pattern acquired experimentally in relation to calculated patern, but with smaller riblet height determines a flat degradation, with the riblet flanks on straight shape, in other way, if the acquired pattern returns back spreading values, without expected periodicity, determines a round degradation, reflecting the laser light on irregular pattern and not following a pre-determined micro-structured geometry.

Simulating a riblet degradation, in this particular case analyzing a regular flat degradation, the calculations demonstrated which is possible identify, based in an expected geometry of the riblet structure, if the structure is degraded or not. Taking the number of peaks calculated via computational tool, this simulation leads the analisys to evaluate and confirm the theory behind the proposed methodology.

Summarizing the findings on this work, Table 8 shows the main criteria to be analysed on status identification of micro-structured coatings:

<b>Evaluation</b>	<b>Criteria</b>
<b>Central Detector</b>	Number of the Riblets
	Height of the Riblet
	Distance between Riblets
	Width of the Riblet Base
<b>Lateral Detectors</b>	Number of the Riblets
	Height of the Riblet
	Degradation Type

**Table 8** Table of analysis criteria evaluated on each detector position

The following general conclusions can be drawn from the obtained results. Micro-structure coatings, especially designed in order to be applied on aerospace industries, and, in this particular case, to be used on drag reduction, it is a powerful technology that improves up to 8% of gains. This technological gain is subject to direct action of external factors, which can cause degradation on the original coating geometry, decreasing the effectiveness of the coating.

Efforts to assure the high quality on the supra-cited micro-structured coatings are expensive and can be destructive, In order to guarantee an optimal performance of the coating, this study approached a non-destructive method to be used to identify the real status of the coating and, it became a list of analysis criteria that could reproduce and identify the level of degradation (or no degradation) on the coating, specifically studied on this work based on the riblet structure coating.

Therefore, presented work describe a scientific progress on the interdisciplinarity applied to join engineering, physics and computer science; emerging substantiated knowledge on mentioned fields to solve with possible substantial gains on the process related to aviation industry. Also in comparison with other techniques, the proposed methodology could be

considered an innovation in terms of applicability; the same theoretical principles can be found in techniques as crystallography, for example; the use to support quality assurance of surfaces in production line or in maintenance line in the industry, proposing an innovative non destructive test is acquired with the integration of the supra-cited fields, linking the entire system to be an innovation in terms of applicability and performance. The use of computer science techniques to upgrade the theoretical knowledge in physics to be successfully applied on engineering, bring substantial inputs in this area to be the embasement to further applications and researches.

In this context, future studies should focus on the investigation of the threshold definition for the degradation levels, definition and identification of degradation patterns, combination of diverse degradation types. The use of data mining techniques tends to be a powerful tool to improve performance on comparison tasks on a knowledge database against the evaluated coating on field, specially developed on a final product to be embedded and applied on industry process.

Other applications can be implemented using the proposed methodology, adjusting the scale, or changing in the surface geometry, could be implemented to analyse another types of coatings and diverse surfaces, for instance, plant leaves.

Improvements on the proposed methodology, also can be successfully applied taking in account that must be considered reflectance factor and the application target, implementing acceptable error levels on the calculations as limits to be evaluated.

### Chapter 9 - References

- [1] 'Shark skin (detail)', <https://goo.gl/znCmJA>
- [2] García-Mayoral, R., Jiménez, J.: 'Drag reduction by riblets', *Philosophical transactions. Series A, Mathematical, physical, and engineering sciences*, 2011, **369**, (1940), pp. 1412–1427
- [3] Stenzel, V., Wilke, Y., Hage, W.: 'Drag-reducing paints for the reduction of fuel consumption in aviation and shipping', *Progress in Organic Coatings*, 2011, **70**, (4), pp. 224–229
- [4] Commission of the European Communities: 'Package of Implementation measures for the EU's objectives on climate change and renewable energy for 2020' (27.2.2008)
- [5] Fahr, A., Wallace, W.: 'Aeronautical applications of non-destructive testing' (DEStech Publications Inc, Lancaster, Pennsylvania, 2014)
- [6] ASTM: 'Specification for Agencies Performing Nondestructive Testing'
- [7] Liu, C.-Y., Fu, W.-E., Lin, T.-Y., Chang, C.-S., Chen, J.-S.: 'Nanoscale surface roughness characterization by full field polarized light-scattering', *Optics and Lasers in Engineering*, 2011, **49**, (1), pp. 145–151
- [8] Imlau, M., Bruening, H., Voit, K., Tschentscher, J., Dieckmann V.: 'Riblet Sensor - Light Scattering on Micro Structured Surface Coatings: Final Report', 2016
- [9] Tschentscher, J., Hochheim Sven, Brüning Hauke, Brune Kai, Imlau, M.: 'Optical Riblet Sensor: Beam Parameter Requirements for the Probing Laser Source', 2015
- [10] Choi, K.-S.: 'Near-wall structure of a turbulent boundary layer with riblets', *J. Fluid Mech.*, 1989, **208**, pp. 417–458
- [11] WALSH, M., WEINSTEIN, L.: 'Drag and heat transfer on surfaces with small longitudinal fins', *AIAA Paper*, 1978
- [12] WALSH, M.: 'Turbulent boundary layer drag reduction using riblets', *AIAA Paper*, 1982
- [13] WALSH, M., LINDEMANN, A.: 'Optimization and application of riblets for turbulent drag reduction', *AIAA Paper*, 1984
- [14] Choi, K.-S., Pearcey, H.H., Savill, A.M.: 'Test of drag reducing riblets on a one-third scale racing yacht', *Proc. Int. Conf. on Turbulent Drag Reduction by Passive Means*, 1987
- [15] McLean, J.D., George-Falvy, D.N., Sullivan, P.P.: 'Flight-test of turbulent skin friction reduction by riblets', *Proc. Int. Conf. on Turbulent Drag Reduction by Passive Means*, 1987
- [16] Squire, L.C., Savill, A.M.: 'Some experiences of riblets at transonic speeds', *Proc. Int. Conf. on Turbulent Drag Reduction by Passive Means*, 1987
- [17] Johansen, J.B., Smith, C.R.: 'The effect of cylindrical surface modification on turbulent boundary layers', *Rep. FM-3. Dept. of Mechanical Engineering and Mechanics, Lehigh University, Pennsylvania*, 1983
- [18] Hoosmand, D., Youngs, R., Wallace, J.M.: 'An experimental study of changes in the structure of a turbulent boundary layer due to surface geometry changes', *AIAA Paper*, 1983
- [19] GALLAGHER, J., THOMAS, A.: 'Turbulent boundary layer characteristics over streamwise grooves', *AIAA Paper*, 1984
- [20] BACHER, E., SMITH, C.: 'A combined visualization-anemometry study of the turbulent drag reducing mechanisms of triangular micro-groove surface modifications', *AIAA Paper*, 1985
- [21] Bechert, D.W., Hoppe, G., REIF, W.: 'On the Drag Reduction of the Shark Skin', *AIAA Paper*, 1985
- [22] Bechert, D.W., Bartenwerfer, M., Hoppe, G., REIF, W.: 'Drag reduction mechanisms derived from shark skin', *15th Congress, International Council of the Aeronautical Sciences, London*, 1986
- [23] Choi, K.-S.: 'Near-wall turbulence structure on a riblet wall', *BMT Rep. BMT Ltd, Feltham, Middlesex, UK*, 1985
- [24] Choi, K.-S.: 'Drag reduction by manipulation of near-wall turbulence structure', *Proc. European Meeting on Turbulent Drag Reduction, Lausanne*, 1986
- [25] Choi, K.-S.: 'The wall pressure fluctuations of modified turbulent boundary layer with riblets', *In Turbulence Management and Relaminarisation (ed. H. W. Liepman & R. Narasinha)*. Springer, 1987

- [26] Choi, K.-S.: 'On physical mechanisms of turbulent drag reduction using riblets', *In Transport Phenomena in Turbulent Flows* (ed. M. Hirata & N. Kasagi). Hemisphere, 1987
- [27] Dinkelacker, A., Nitschke-Kowsky, P., REIF, W.: 'On the possibility of drag reduction with the help of longitudinal ridges in the walls', *In Turbulence Management and Relaminarisation* (ed. H. W. Liepman & R. Narasinha). Springer, 1987
- [28] Coustols, E., Cousteix, J.: 'Reduction of turbulent skin friction : turbulence moderators', *Rech. Aerosp.*, 1986, p. 63
- [29] Nieuwstadt, F.T.M., van Dam, W., Leidjens, H., Pulles, C.: 'Some turbulence measurements above a grooved wall', *Proc. European Drag Reduction Conf. Lausanne*, 1986
- [30] REIDY, L.W.: 'Flat plate drag reduction in a water tunnel using riblets', *Naval Ocean Systems Center TR1169*, 1987
- [31] REIDY, L., ANDERSON, G.: 'Drag reduction for external and internal boundary layers using riblets and polymers', *AIAA Paper*, 1988
- [32] Djenidi, L., Liandrat, J., Anselmet, F., Fulachier, L.: 'About the mechanism involved in a turbulent boundary layer over riblets', *Proc. Second European Turbulence Conf., Berlin*, 1988
- [33] Anderson, E.J., MacGillivray, P.S., Demont, M.E.: 'Scallop Shells Exhibit Optimization of Riblet Dimensions for Drag Reduction', *Biol. Bull.*, 1997, pp. 341–344
- [34] WALSH, M.J.: 'Effect of detailed surface geometry on riblet drag reduction performance', *Journal of Aircraft*, 1990, **27**, (6), pp. 572–573
- [35] Anderson, D.G.: 'Coatings', *Anal. Chem.*, 1997, **69**, (12), pp. 15–28
- [36] Bechert, D.W., Bruse, M., Hage, W.: 'Experiments with three-dimensional riblets as an idealized model of shark skin', *Experiments in Fluids*, 2000, **28**, (5), pp. 403–412
- [37] Lee, S.-J., Lee, S.-H.: 'Flow field analysis of a turbulent boundary layer over a riblet surface', *Experiments in Fluids*, 2001, **30**, (2), pp. 153–166
- [38] WALSH, M.J.: 'Riblets as a Viscous Drag Reduction Technique', *AIAA Journal*, 1983, **21**, (4), pp. 485–486
- [39] Viswanath, P.: 'Aircraft viscous drag reduction using riblets', *Progress in Aerospace Sciences*, 2002, **38**, (6-7), pp. 571–600
- [40] FROHNAPFEL, B., Jovanovic, J., DELGADO, A.: 'Experimental investigations of turbulent drag reduction by surface-embedded grooves', *J. Fluid Mech.*, 2007, **590**
- [41] Jovanovic, J., Hillerbrand, R.: 'ON PECULIAR PROPERTY OF THE VELOCITY FLUCTUATIONS IN WALL-BOUNDED FLOWS', *J. Thermal Science*, 2005, pp. 3–12
- [42] "degradation" Word Central: Merriam-Webster's Student's Electronic Dictionary', <http://www.merriam-webster.com/dictionary/degradation>, accessed September, 2016
- [43] Yang, X., Vang, C., Tallman, D., Bierwagen, G., Croll, S., Rohlik, S.: 'Weathering degradation of a polyurethane coating', *Polymer Degradation and Stability*, 2001, **74**, (2), pp. 341–351
- [44] Yang, X.F., Li, J., Croll, S.G., Tallman, D.E., Bierwagen, G.P.: 'Degradation of low gloss polyurethane aircraft coatings under UV and prohesion alternating exposures', *Polymer Degradation and Stability*, 2003, **80**, (1), pp. 51–58
- [45] Raj, B., Jayakumar, T., Thavasimuthu, M.: 'Practical Non-destructive Testing', 2002 (Woodhead Publishing, 2002, 2nd edn.)
- [46] Paula Leite, P. G. de: 'Curso de Ensaio nao destrutivos (Non destructive Tests Course)', 1973 (Sao Paulo, 1973, 4th edn.)
- [47] Halmshaw, R.: 'Non-destructive Testing Techiques', 1991 (1991, 2nd edn.), p. 43
- [48] Andreucci, R.: 'Radiologia Industrial (Industrial Radiology)', 2010 (ABENDE, Sao Paulo, 2010), p 6-22
- [49] Stegeman, D.: 'Zerstörungsfreie Prüfverfahren: Radiografie und Radioskopie', 1995, (v. 36) (1995), p. 36
- [50] 'Quality Control and NDT, Nondestructive Testing'
- [51] Cherfaoui, M.: 'Innovative Techniques in Non-Destructive Testing and industrial Applications on Pressure Equipment', 2012 (2012), p. 267
- [52] Halmshaw, R.: 'Introduction to the Non-destructive testing of Welded joints', 1996 (Ed. Butterwoth-Heinemann Ltd., 1996, 2nd edn.), p.5

## Chapter 9 - References

---

- [53] Shull, P.J.: 'Nondestructive Evaluation Theory, Techniques and Applications', 2002 (Altoona, Pennsylvania, 2002), p. 63
- [54] Araujo, G.M.: 'Seguranca na Armazenagem, Manuseio e Transporte de Produtos Perigosos' (Rio de Janeiro, 2005, 2nd edn.)
- [55] 'Technical Specification - Smart High Sensitivity CCD Line Camera', [https://www.thorlabs.com/newgrouppage9.cfm?objectgroup\\_id=5290](https://www.thorlabs.com/newgrouppage9.cfm?objectgroup_id=5290), accessed April, 2017
- [56] Hecht, E.: 'Optics', 1998 (Pub. Addison Wesley Longman, Inc., New York, 1998, 3rd edn.)
- [57] Lipson, S.G.: 'Optical Physics', 1995 (Pub. Cambridge University Press, Cambridge, 1995, 3rd edn.)
- [58] Guenther, R.D.: 'Modern Optics', 1990 (Pub. John Wiley & Sons, Ltd., New York, 1990)
- [59] Smith, F. G. Thomson, J. H.: 'Optics', 1988 (Pub. John Wiley & Sons, Ltd., New York, 1988)
- [60] Giancoli, D.C.: 'Physics for Scientists and Engineers with Modern Physics', 1988 (Pub. Prentice-Hall, Inc., New Jersey, 1988, 2nd edn.)
- [61] Meyer-Arendt, J.R.: 'Introduction to Classical and Modern Optics', 1995 (Pub. Prentice-Hall, Inc., New Jersey, 1995, 4th edn.)
- [62] Wilson, R.: 'Fourier Series and optical Transform Techniques in Contemporary Optics: An Introduction', 1995 (Pub. John Wiley & Sons, Ltd., New York, 1995)
- [63] Halliday, D., Resnick, R., Walker, J.: 'Fundamentals of Physics - extended', 1997 (Pub. John Wiley & Sons, Ltd., New York, 1997)
- [64] Pedrotti, F.L., Pedrotti, L.S.: 'Introduction to Optics', 1993 (Pub. Prentice-Hall, Inc., New Jersey, 1993, 2nd edn.)
- [65] Jenkins, F.A., White, H.E.: 'Fundamentals of Optics', 1976 (Mcgraw-Hill Book Company, Inc., Singapore, 1976, 4th edn.)
- [66] Beynon, J.H.: 'Introductory University Optics', 1996 (Prentice Hall Europe, Hertfordshire, 1996)
- [67] Rossi, B.: 'Optics', 1965 (Pub. Addison Wesley Publishing Company, Inc., Massachusetts, 1965, 3rd edn.)
- [68] Fowles, G.: 'Introduction to modern optics. 2.ed' (Holt, Rinehart and Winston, 1975, New York, N.Y., 1975)
- [69] Born, M., Wolf, E.: 'Principles of optics: Electromagnetic theory of propagation, interference and diffraction of light' (Cambridge University Press, Cambridge, New York, 2006, 7th edn.)
- [70] Reis, D.M., Santos, E.M., Andrade-Neto, A.V.: 'Diffraction patterns from n non-symmetric slits and arbitrary widths', *Rev. Bras. Ensino Fís.*, 2015, **37**, (2), 2312-1-2312-9
- [71] Vriesman, D., Pacheco, M.Z.: 'Development of an object oriented programming based software for quality assurance of structured coatings for aerospace applications', 2014 (Darmstadt - Germany, 2014)
- [72] Colak, I., Sagiroglu, S., Yesilbudak, M.: 'Data mining and wind power prediction: A literature review', *Renewable Energy*, 2012, **46**, pp. 241–247
- [73] E.V:Ramana and P.Ravinder Reddy: 'Dta Mining Based knowledge discovery for quality prediction and control of extrusion blow molding process', *International Journal of Advances in Engineering & Technology*, 2013
- [74] Lee, I., Qu, Y., Lee, K.: 'Mining qualitative patterns in spatial cluster analysis', *Expert Systems with Applications*, 2012, **39**, (2), pp. 1753–1762
- [75] Oracle: 'Java' (Oracle, 2017)
- [76] Oracle: 'JAVASE' (Oracle, 2017)
- [77] Netbeans: 'Netbeans' (Netbeans, 2017)
- [78] Microsoft: 'SQL-Server Express' (Microsoft, 2008)
- [79] Chamorro, L.P., Arndt, R., Sotiropoulos, F.: 'Drag reduction of large wind turbine blades through riblets: Evaluation of riblet geometry and application strategies', *Renewable Energy*, 2013, **50**, pp. 1095–1105
- [80] Bechert, D.W., Bruse, M., Hage, W., Van Der Hoeven, J. G. T., Hoppe, G.: 'Experiments on drag-reducing surfaces and their optimization with an adjustable geometry', 1997
- [81] Joseph W. Goodman: 'Introduction to Fourier Optics' (The McGraw-Hill Companies, INC, 1996)



## Chapter 9 - References

---

- [82] Lorrain, P., Corson, D.: 'Electromagnetic fields and waves. 2.ed' (Freeman, San Francisco, Calif., 1970)
- [83] Missoffe, A., Chassagne, L., Topçu, S., Ruaux, P., Cagneau, B., Alayli, Y.: 'New simple optical sensor: From nanometer resolution to centimeter displacement range', *Sensors and Actuators A: Physical*, 2012, **176**, pp. 46–52
- [84] Saravi, S.S., Cheng, K.: 'A review of drag reduction by riblets and micro-textures in the turbulent boundary layers', *European Scientific Journal*, 2013, **9**, (33), pp. 62–81
- [85] Tang, Z., Maclennan, J., Kim, P.: 'Building Data Mining Solutions With OLE DB for DM and XML for Analysis', in Maimon, O., Rokach, L. (Eds.): 'Data Mining and Knowledge Discovery Handbook' (Springer-Verlag, New York, 2005), pp. 1331–1345
- [86] Tornow, C., Schlag, M., Lima, L.C.M., *et al.*: 'Quality assurance concepts for adhesive bonding of composite aircraft structures – characterisation of adherent surfaces by extended NDT', *Journal of Adhesion Science and Technology*, 2015, **29**, (21), pp. 2281–2294
- [87] David J Whitehouse: 'Handbook of Surface and Nanometrology', 2003
- [88] Kordy, H.: 'Process abilities of the riblet-coating process with dual-cure lacquers', *CIRP Journal of Manufacturing Science and Technology*, **11**, pp. 1–9